Physik-Department E12 der Technischen Universität München

Study of the e^+e^- pair acceptance in the dilepton spectrometer HADES

Laura Fabbietti

Vollständiger Abdruck der von der Fakultät für Physik der
Technischen Universität München zur Erlangung des akademischen Grades eines

Doktors der Naturwissenschaften (Dr. rer. nat.)

genehmigten Dissertation.

Vorsitzender: Univ.-Prof. Dr. Andrzej J. Buras

Prüfer der Dissertation:

1. Univ.-Prof. Dr. Reiner Krücken
2. Univ.-Prof. Dr. Stephan Paul

Die Dissertation wurde am 14. 11. 2003 bei der Technischen Universität München eingereicht und durch die Fakultät für Physik am 27 11 2003 angenommen.

Summary

This thesis contains a detailed study of the di-electron pair acceptance of the HADES spectrometer. First of all, the response of the RICH detector has been analyzed via a dedicated efficiency measurement, that has allowed us to understand the response of the detector to a single photon and to evaluate the overall detector efficiency. The figure of merit N_0 of the detector has been calculated for each of the six RICH sectors separately and values between 70 and 85 have been found. The analysis of this measurement has allowed us to develop a very detailed detector parameterization, that enabled to calculate the single electron efficiency of the RICH detector on the base of simulations. An average single electron efficiency of 85% has been evaluated for e^+e^- pairs produced in the target. For γ-conversion products the efficiency is reduced to 20% .

A set of full scale simulation of the whole spectrometer for the heavy ion reaction C + C at 1 and 2 $AGeV$ has been performed, to compare the signature of the e^+e^- pairs between simulation and experiment. The comparison has shown a good agreement between the two data sets as far as the RICH detector is concerned. The overall e^+e^- pair acceptance and efficiency of the whole HADES spectrometer has been also calculated using simulations for unlike/like-sign pairs. The geometrical acceptance of the unlike-sign pairs has been estimated around 35%, similar values have been obtained for the negative like-sign pairs. A lower geometrical acceptance (on average reduced by 8%) has been found for the positive like-sign pairs. The recognition efficiency for the unlike-sign pairs in the geometrical acceptance has be found to be around 45% in the high invariant mass region ($M > 300MeV/c^2$) and 15% in the low region ($M < 150MeV/c^2$). This leads to an absolute efficiency of 18% and 5% respectively for the unlike-sign e^+e^- pairs.
The simulated and the experimental e^+e^- invariant mass spectra have been corrected for the efficiency. The comparison of the corrected distributions has shown a good qualitative agreement but not a quantitative one.

Zusammenfassung

In Rahmen dieser Doktorarbeit wurde die Akzeptanz des HADES Spektrometers für Dielektronen untersucht. Zuerst wurde die Antwort des RICH Detektors mittels einer dedizierten Effizienzmessung analysiert. Dadurch war es möglich die Antwort des Detektors auf Einzelphotonen zu verstehen und die gesamte Detektoreffizienz zu bestimmen. Für jeden der sechs RICH Sektoren einzeln wurde die 'Figure of Merit' berechnet und Werte zwischen 70 und 85 ermittelt. Die Analyse dieser Messung führte zur Entwicklung einer sehr detaillierten Parameterisierung des Detektors, mittels welcher die Einzelelektroneneffizienz des RICH Detektors auf der Basis von Simulationen berechnet wurde. Es konnte eine Effizienz von 85% für einzelne Elektronen, die aus dem Target stammen, ermittelt werden. Für die γ-Konversionsprodukte reduzierte sich die Effizienz auf 20%.

Eine Menge von massstäblichen Simulationen des gesamten Spektrometers für die Reaktion C + C bei 1 und 2 AGeV wurde durchgeführt, um die Signatur der e^+e^- Paare im Experiment und in der Simulation zu vergleichen. Dieser Vergleich ergab eine gute Übereinstimmung zwischen den beiden Datensätzen, was den RICH Detektor angeht. Ebenfalls wurde die gesamte e^+e^- Paarakzeptanz und Effizienz des HADES Spektrometers mittels Simulationen für Paare mit ungleichen/gleichen Vorzeichen bestimmt. Die geometrische Akzeptanz der Paare mit ungleichem Vorzeichen wurde auf 35% geschätzt; ähnliche Werte wurden für Paare mit negativem gleichem Vorzeichen erhalten. Eine kleinere geometrische Akzeptanz (im Mittel reduziert um 8%) wurde für die Paare mit positiven Vorzeichen ermittelt. Die Erkennungseffizienz für Paare mit ungleichen Vorzeichen in der geometrischen Aktzeptanz wurde für den Bereich mit grosser invarianter Masse ($M > 300 MeV/c^2$) zu ungefähr 45% bestimmt und zu 15% im Bereich mit kleiner invarianter Masse ($M < 150 MeV/c^2$). Dies führt zu einer absoluten Effizienz von 18 % und 5 % für Paare mit ungleichem Vorzeichen.

Die simulierten und gemessenen e^+e^- Spektren der invarianten Masse wurden mit der jeweiligen Effizienz korrigiert. Der Vergleich der korrigierten Verteilungen zeigte eine gute qualitative, jedoch keine quantitative Übereinstimmung.

Contents

Chapter 1

Introduction

The investigation of the properties of nuclear matter over a wide range of temperatures and densities is one of the major topics of contemporary nuclear physics. The main motivation for this is to investigate the equation of state (EOS) of nuclear matter and to test the predictions of the fundamental theory of strong interactions, quantum chromodynamics (QCD). The EOS of strongly interacting matter is of importance for astrophysical problems like neutron stars and supernovae, as well as Big Bang nucleosynthesis and related topics [Cas 99].
As nuclear matter is heated and compressed, hadrons occupy more and more of the available space. They can start to overlap and the confined quarks and gluons begin to percolate between the hadrons and to be "liberated". This idea has been confirmed by QCD lattice calculations at finite temperature. The latter predicts a phase transition in which the confined hadrons turn into a *quark gluon plasma* (QGP), where quarks and gluons become deconfined. This transition is expected at very high densities and temperature: $\rho \geq 5\rho_0$[1] or T $\geq$ 170 MeV.
At the same time the up (u) and down (d) quarks loose their masses, that is of a few hundred MeV, leading to a restoration of the *chiral symmetry* [Ern 98], an approximate symmetry of QCD valid for the light quarks. Once massless, left- and right-handed quarks decouple leading to a degeneracy in hadronic states of opposite parity.
Figure 1.1 shows the expected phase diagram of hadronic matter [Sta 98]. The cross-hatched region indicates the transition from confined to deconfined strongly interacting matter. The confined phase consists of an interacting gas of hadrons, while the deconfined phase is comprised of a non ideal gas of quarks and gluons. Also shown are the so-called chemical and thermal freeze-out. The chemical freeze-out refers to the stage of the reaction where the inelastic collisions cease and the fireball acquires its final particle composition. The thermal freeze-out refers to the stage where even the elastic collisions cease and the momentum distributions of the hadron do not change any longer. The chemical freeze-out is calculated under the assumption of thermodynamical equilibrium [Bra 96], via an hadrochemical analysis of the particle species. Figure 1.1 also shows the results of experiments performed at different beam energies.[2] As it can be seen in

[1] $\rho_0 = 0.17$ fm^{-3} is the saturation density of symmetric nuclear matter.

[2] The accelerators SIS (SchwerIonen Synchrotron at GSI, Darmstadt), AGS (Alternating Gradient Synchrotron at Brookhaven National Laboratory, Long Island), SPS (Super Proton Synchrotron at the European Research Laboratory CERN in Geneva), and RHIC (Relativistic Heavy-Ion Collider at Brookhaven National Laboratory, Long Island) deliver heavy-ion beams with energies up to 4(Z/A)GeV, 29(Z/A)GeV, 400(Z/A)GeV and $\sqrt{s} = 200$ AGeV, respectively. Z(A) denotes the charge (mass number) of the projectile nuclei.

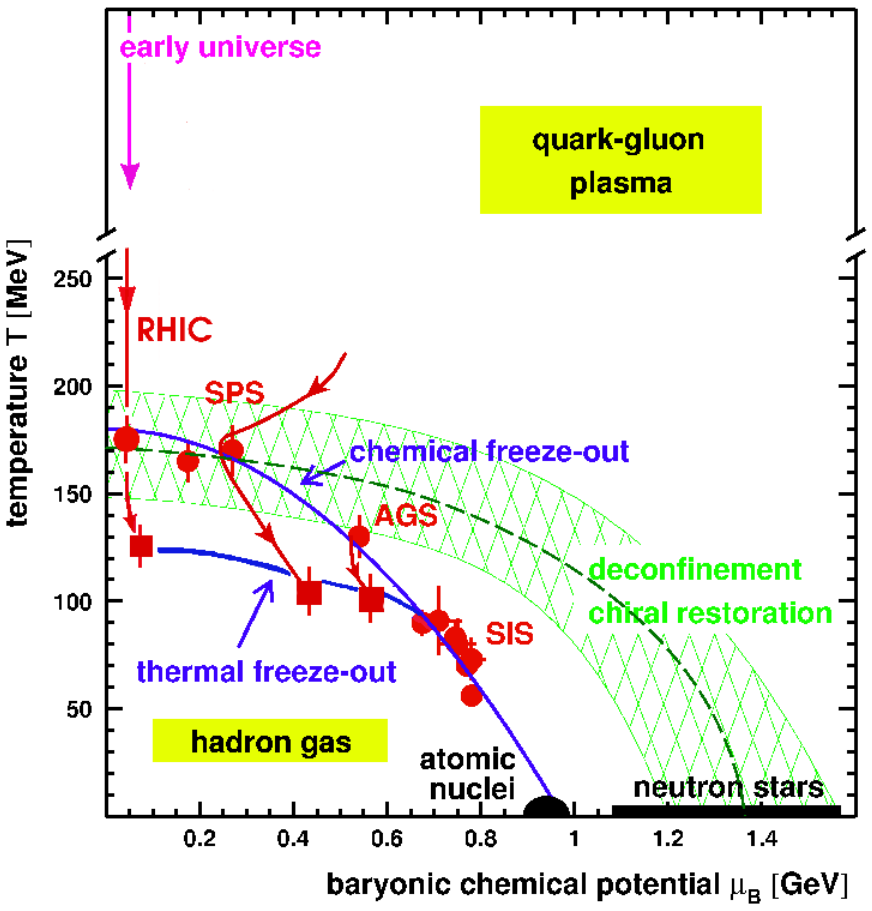

Figure 1.1: Schematic phase-diagram of strongly interacting matter [Sta 98]. Depicted are lines of chemical and thermal (kinetic) freeze-out and corresponding results from various accelerators. The chemical freeze-out parameters are deduced from hadron yields, while the thermal freeze-out parameters result from analysis of transverse momentum spectra. The cross-hatched area indicates the region of the outset of deconfinement and chiral symmetry restoration.

the phase diagram, the chemical and thermal freeze-out curves merge at SIS energies. The corresponding matter state is clearly within the confinement region. In this energy regime, the achieved states of strongly interacting matter consist of nucleons which are excited into baryonic resonance states to a substantial fraction (such as Δ and N^*), along with accompanying meson production, mainly pions.

At these densities (up to $\rho = 3\rho_0$) one expects a trend toward chiral restoration, that implies a decreasing of the scalar quark condensate $< q\bar{q} >$ [Wei 96] with increasing temperatures and density. As a result one should expect that some properties of light hadrons, such as masses, spectral functions and couplings, change considerably in the nuclear environment, where the chiral condensate is expected to be reduced.

Since the quark condensate is sensitive to changes of the density, one expects valuable insights into its properties at SIS energies (on the contrary, at relativistic beam energies hot and baryon-poor matter is produced and deconfinement effects are envisaged to be

probed).

1.1 Di-lepton spectroscopy

To be able to study the quark-hadron transition induced in heavy-ion reactions one has to isolate observable signals. Because of their negligible final-state interaction with the hadronic environment, di-leptons (correlated lepton pairs e^+e^- and $\mu^+\mu^-$) as well as photons are considered ideal probes for the high-density/temperature regions formed in the early stages of the collisions [Shu 78]. The invariant pair mass M_{ll} variable allows a superior signal to background and classifies the di-leptons as better probes compared to the photons.
Of particular interest are the e^+e^- decays of the vector mesons ρ, ω and ϕ. As shown in table 1.1 the lifetimes of these particles are comparable with the typical fireball lifetime ($10 - 15\ fm/c$) and therefore all the ρ mesons and part of $\omega - \phi$ mesons produced in the collision decay inside the interaction region.

meson	mass (MeV/c^2)	width (MeV/c^2)	lifetime τ (fm/c)	e^+e^- branching ratios
ρ	768	152	1.3	4.4×10^{-5}
ω	782	8.43	23.4	7.2×10^{-5}
ϕ	1019	4.43	44.4	3.1×10^{-4}

Table 1.1: Characteristic quantities of light vector mesons.

Brown and Rho [Bro 91] proposed the idea that most hadron masses should be reduced in nuclear matter. In such a way the hope was born to verify explicitly the mass change of the ρ meson in strongly interacting matter. It was supposed that the ρ meson mass is directly related to the quark condensate. Therefore, by quantifying a change of the ρ meson via the di-electron decay channel, one is able to measure directly the change of the chiral condensate. However, in practice there are a few things making electromagnetic probes rather difficult:

1. There are several competing background processes generating di-electrons: Bremsstrahlung and Dalitz decays of Δ, ω, η, π^0. These decays produce e^+e^- pairs mainly in the low-mass region. Dalitz decays of higher baryon resonances can become sizable.

2. Since di-electrons are monitoring the full time evolution of strongly interacting matter, the finally observed spectra consist of a convolution of all stages with the local emission strength. This makes the deconvolution difficult.

3. Experimentally, electromagnetic signals are rare probes due to their small branching ratios (see table 1.1).

For these reasons the first generation of heavy-ion collision experiments observing di-leptons encountered several limitations which must be overcome by improved experimental devices. Hereafter, the first generation experiments will be mentioned.

1.1.1 Experiments at CERN-SPS

The CERES [Aga 96] and HELIOS [Mas 95] collaborations measured di-lepton spectra at CERN-SPS energies (30 $AGeV < E_{beam} < 200$ $AGeV$) and found a significant enhancement of the low energy di-lepton yield below the ρ and ω peaks [Aga 96] in heavy ions systems (Pb + Au) compared to light systems (S + W) and proton induced reactions (p + Be).
Figure 1.2 shows the latest results [Dam 01] of the analysis of the Pb+Au collisions at 40 AGeV where an enhancement of the number of di-electrons in the mass region below the vacuum ρ peak by a factor of 5.1 $\pm$ 1.3 (stat.) $\pm$ 1.0 (syst.) is visible. This enhancement can be theoretically explained within a hadronic picture by the assumption of a dropping ρ mass [Cas 95] or by the inclusion of in-medium spectral functions for the vector mesons [Urb 98],[Bra 98]. In both cases the enhanced low energetic di lepton yield is not simply caused by a shift of the ρ and ω peaks in the nuclear medium but it may also originate from an enhanced contribution of the $\pi^+\pi^-$ annihilation channel.

1.1.2 DLS puzzle

A similar situation occurs at a completely different energy scale, namely around 1 AGeV incident energies, where the low mass region of the di-electron invariant mass spectra are underestimated by present transport calculations compared to *pp* and *pd*

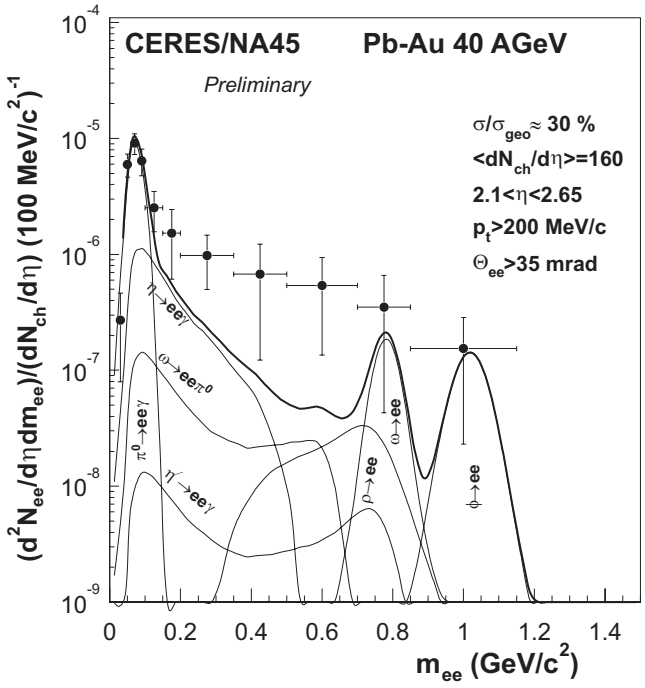

Figure 1.2: Inclusive invariant e^+e^- mass spectrum in 40 AGeV Pb + Au collisions normalized to the observed charged-particle density observed by CERES [Dam 01]. The full line represents the e^+e^- yield from hadron decays scaled from p-induced collisions.

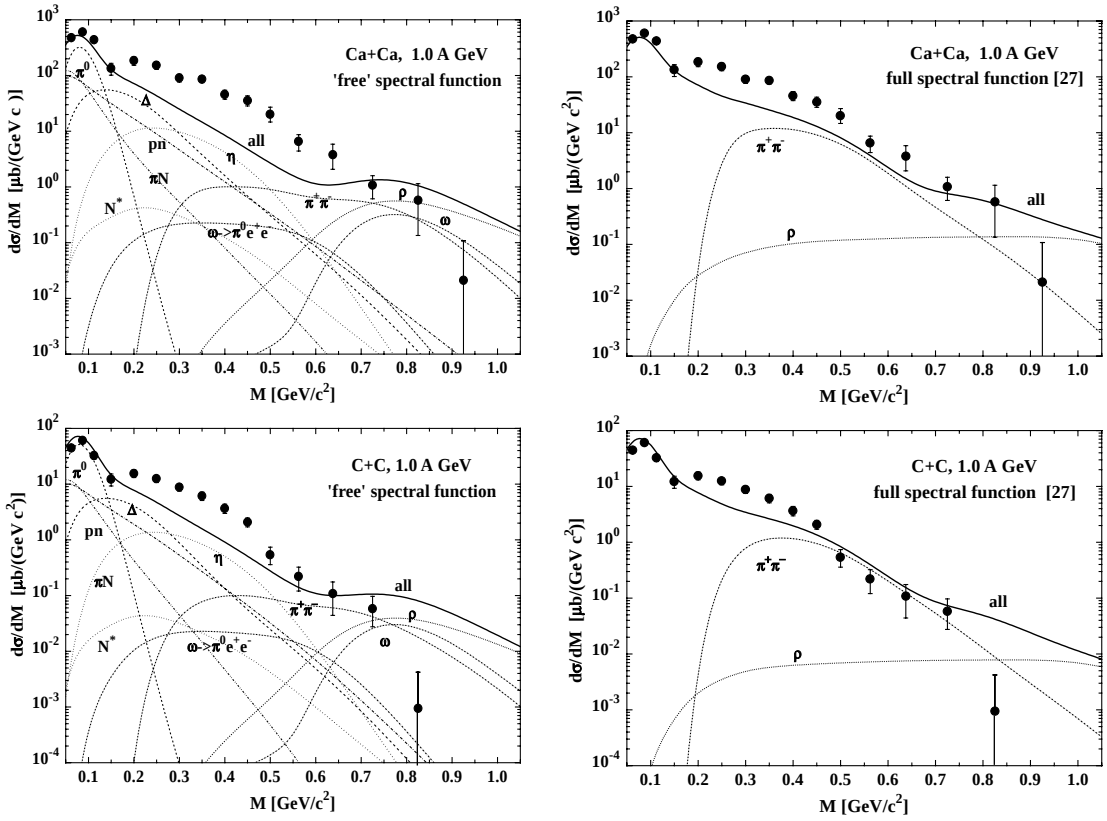

Figure 1.3: Differential cross section (full circles) for di-electron production measured by the DLS collaboration [Mat 95] in comparison to BUU transport calculations (full line) [Bra 98]. The left panel refers to calculations that estimate the contribution of each source using the "free"spectral function for the decay in vacuum. For the right panel the yield for ρ and $\pi^+\pi^-$ annihilation have been calculated using in-medium spectral functions.

reactions.
The DLS[3] collaboration at the BEVALAC [Por 95] measured in the late '80s and in the early '90s the di-electron invariant mass spectra for p + p and p + d collisions with beam kinetic energies from 1.04 to 4.88 GeV, Ca + Ca at 1 and 2 AGeV and also systems such as C + C, d + Ca and He + Ca. For the Ca + Ca system the data lead to differential di-lepton production cross sections, which are up to 7 times larger than predicted by conventional models (see figure 1.3). The discrepancy between experiment and theoretical predictions, based on a cocktail of free hadron sources of e^+e^- pairs,

[3] DiLepton Spectrometer

was denoted as *lepton yield enhancement*. This behavior is particularly visible in the medium invariant mass range 200 $MeV/c^2 < M_{inv.} < 600\ MeV/c^2$ (see figure 1.3), below the ρ/ω region. The discrepancy could be reduced to a factor three by more refined theoretical calculations [Bra 98] in which the in-medium spectral function of the ρ meson was included (see figure 1.3, right panel).
Another attempt to describe the experimental data has been performed using the ultra relativistic quantum molecular dynamic (UrQMD) transport calculations, which explicitly implement a dropping of the ρ meson mass according to the Brown-Rho scaling [Ern 98]. This model fails to describe the data too.
The consideration of additional e^+e^- sources from sub-threshold ρ production via the N(1520) resonance increased the contribution at masses below the ρ meson [Bra 99] but did not enhance sufficiently the total yield in the medium mass range.
The difficult interpretation of these data has to cope with two additional constraints. First one cannot attribute the yield enhancement below $M_{inv.} \leq 500\ MeV/c^2$ to the η-Dalitz decay contribution, since this assumption would contradict the η production cross sections measured for C + C and Ca + Ca [Hol 97]. Secondly, the measured di-lepton spectra from elementary pp collisions [Wil 98] are reasonably well reproduced by the transport model approaches [Bra 00].
Therefore, the di-lepton enhancement seen already for light ion collisions might be already a hint of medium modifications.
The HADES collaboration aims to study the continuum region of the di-lepton invariant mass spectrum for the C + C system with reasonable statistics and better signal to background ratio than the DLS experiment.

1.2 Second generation di-lepton spectrometers

The **H**igh **A**cceptance **D**i-**E**lectron **S**pectrometer (HADES) at GSI, Darmstadt, provides the possibility for electron-positron pair spectroscopy at incident energies up to 2 AGeV. These energies together with a proper choice of the collision system allow access to a wide region in the nuclear matter phase diagram ranging from ground state matter density ρ_0 up to $3\rho_0$ and temperatures up to 100 MeV. The long range physics program of HADES includes the systematic studies of e^+e^- pair production in hadron and heavy-ion induced collision systems and to look for precursor effects of chiral symmetry restoration. The SIS delivers as projectiles pions with a momentum range from 0.6 to 2.8 GeV/c, protons and heavy ions at beam energies up to 4.7 GeV and 2 AGeV respectively. During its heavy ion collisions program, HADES will identify ρ, ω and ϕ decays and search for shifts of the corresponding spectral lines. In parallel the continuum below the ρ/ω peak will be addressed to resolve the DLS puzzle.
Besides the heavy-ion collisions, a focus will also be on elementary hadronic reactions, such as $\pi + N$, to study the predicted $\rho - \omega$ interferences, which require very sensitive experiments.

Another important motivation concerns the measurement of electromagnetic form factors of mesons and baryons, such as the ω transition form factor. Knowledge of such properties is very important for theoretical models of hadrons, since the form factors

carry complete information on the electromagnetic structure of the particles.
The di-electron invariant mass spectra are reconstructed from a signal that is very weak in comparison with other heavy ion reaction products. If one looks at the production cross-section of the different mesons and their branching ratios (see table 3.2 and table 3.3), one expects for the reaction C+C at 2 AGeV a yield of $3 \cdot 10^{-3}$ e^+/e^- pairs produced in π^0-Dalitz decays and $1.8 \cdot 10^{-7}$ pairs from direct ω decays per collision. These numbers can be compared to the average multiplicities of 1.3 charged pions and 14 protons per event for the same reaction.
In order to be able to compare the experimentally reconstructed di-electron invariant mass distributions with theoretical models, mainly three conditions should be fulfilled:

- the mass resolution should be sufficient to enable the recognition of structures with narrow width like the expected mass of the ω,
- the intensity of the invariant mass signal must be quantitatively understood over the whole mass range,
- the combinatorial background must be correctly evaluated and subtracted from the total signal, to extract the net signal.

The first of these requirements will be mainly determined by the momentum resolution of the spectrometer, since the geometrical acceptance of the HADES spectrometer is quite large and flat and therefore no artificial structures should appear in the invariant mass spectrum.
The intensity of the reconstructed di-electron invariant mass signal depends crucially on the single electron and di-electron pair efficiency of the sub-detector components. In particular it depends on the single electron efficiency of the **R**ing **I**mage **CH**erenkov detector, which is used for the electron/positron recognition.
The evaluation of the combinatorial background and the rejection of tracks, that mainly contribute to the background, depends on one side on the number of misidentified ring images in the RICH detector and on the other hand on the combination of a good two-hit resolution in the RICH and the two-tracks discrimination in the particle tracking detector (**M**ulti-wire **D**rift **C**hambers). Indeed, all e^+e^- pairs with very small opening angles ($\alpha < 2^\circ$) will be identified as a single ring in the RICH detector and can possibly be resolved in the tracking chambers. Such close pairs are produced predominantly in γ-Conversion and π^0-Dalitz processes, with comparably higher cross-sections (see chapter 3) and constitute the main background source.

The aim of the present work is to provide answers for the second and third point of the list. For this reason a dedicated experiment has been carried out and the experimental results have been quantitatively compared with simulations. First the photon detection efficiency of the RICH detector was determined and a parameterization for the simulation of the detector was developed. These results have lead to the determination of the electron detection efficiency of the RICH detector together with the inner tracking system. Finally the di-electron pair acceptance of the whole HADES spectrometer has been studied on the base of simulated and experimental data.
Before these items will be described in the following chapters, the HADES spectrome-

ter will be presented and the expected invariant mass spectra for the simulation of the reaction C + C at 2 AGeV discussed.

Chapter 2

The HADES spectrometer

2.1 Overview

The HADES experiment (High Acceptance Di-Electron Spectrometer) has been set up at the GSI (Gesellschaft für Schwerionenforschung) laboratory for the study of e^+e^- pair production in nuclear reactions. It makes use of the heavy ion synchrotron accelerator (SIS) that delivers beams ranging from proton to uranium, with energies up to 2 $AGeV$ and intensities up to 10^{11} particles/s. The experimental goal is the identification and momentum determination of e^+e^- pairs coming from the decay of mesons produced in π, p and heavy ion induced reactions. In order to fulfill these tasks efficiently the following features have to be realized:

- *Solid angle acceptance:* For the maximization of the detected number of di-leptons the solid angle coverage should achieve a value close to 2π.
- *Track resolution:* A position resolution $\delta x \leq 100\mu m$ have to be reached in the tracking detectors in order to obtain a momentum resolution $\frac{\delta p}{p} \approx 1\%$.
  The most abundant sources of di-lepton pairs are conversion processes and π^0 Dalitz decays. The combination of the reconstructed leptons into pairs form a combinatorial background that endangers the recognition of the real signal. In order to suppress this combinatorial background, a high double track discrimination is needed together with the use of high radiation length material to diminish the multiple scattering and secondary reactions.
- *Stability at high rates:* The vector mesons of interest, ρ and ω, have a production yield in the order of 10^{-3} particle per collision in the heavy ion reactions at the 1-2 $AGeV$ energy range. Moreover they decay into di-leptons with branching ratios of the order of 10^{-5}. In order to detect such pairs with good statistics, a high reaction rate is needed, that the detectors should be able to handle.

These requirements are satisfied by a spectrometer that covers about 50% of the total phase space with a good acceptance in the mid rapidity region [Sch 96] for the products from nuclear reactions (see figure 2.1). All sub-detectors are composed of six sectors each covering 60 degrees in azimuthal angle and between 18 and 85 degrees in polar angle. The geometry is rotationally symmetric around the beam pipe. The inner-most detector of HADES is the **R**ing **I**mage **CH**erenkov detector (RICH), where the electron positron recognition is done. Particles produced in the target, placed inside the RICH, travel through a gas radiator and cross a very thin spherical mirror. After that they

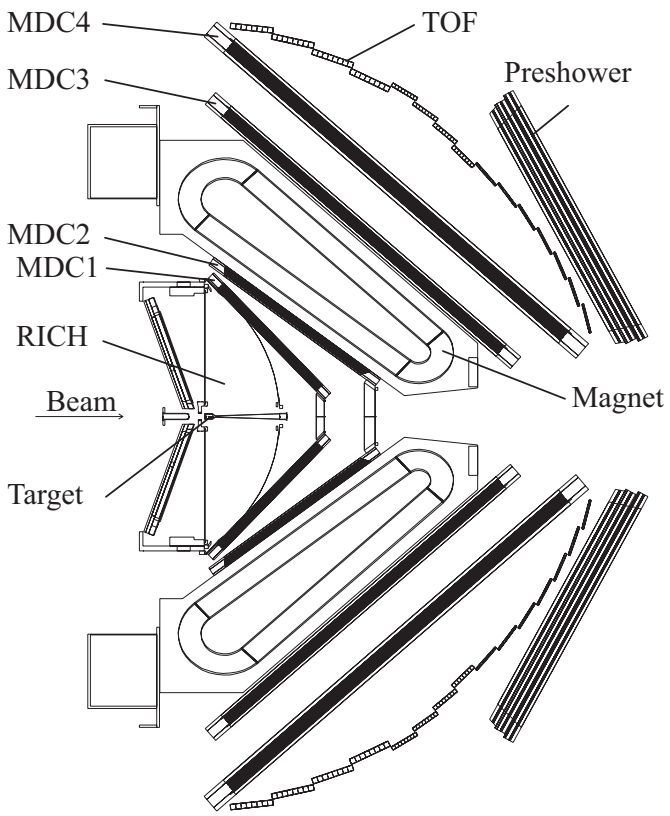

Figure 2.1: Schematic cross-section of the HADES spectrometer.

reach the first two planes of the **M**ulti-wire **D**rift **C**hambers (MDC). The spectrometer is equipped with six superconducting coils that produce a toroidal magnetic field of radially (increasing polar angle) declining strength. The magnet is placed downstream from the first two MDC planes. Two more MDC planes are located after the magnetic field, such that the position of the particle can also be measured after the deflection in the field. The momentum is then calculated reconstructing the particle trajectory with the help of the hits in the four MDC modules. A **T**ime **O**f **F**light wall (TOF) is located at the end of the spectrometer. It measures the particle's velocity and enables the determination of the particle identity. The start signal for the time of flight measurement is given by a diamond start detector [Ber 00], placed 30 cm upstream from the target. In the polar angle range between 18 and 45 degrees behind the TOF is placed a Pre-Shower detector that provides additional information about the particles identity in a phase space region where the particle density is higher and the TOF can not distinguish very well pions from electrons. In the following the TOF and Pre-Shower detectors together will be addressed as META (**M**ultiplicity and **E**lectron **T**rigger **A**rray) detector. In the following, all the detector components will be described with particular emphasis for the electron/positron identification.

2.2 The Ring Image Cherenkov detector

Cherenkov detectors are able to identify and select particles on the basis of their velocity. If a particle crosses a dielectric medium a time-dependent electric field will be generated around the particle trajectory. This leads to a variable polarization in the particle's neighborhood. If the speed of the particle is faster than the phase velocity c' = c/n of light in the medium, the produced wavefronts will overlap in a constructive mode with an opening angle Θ_C around the particle trajectory given by [Che 37]:

$$\cos\theta_c = \frac{1}{n\beta}, \qquad \beta = \sqrt{1 - \frac{1}{\gamma^2}}, \tag{2.1}$$

where θ_c denotes the opening angle of the light cone, n the refraction index of the material in which the Cherenkov photons are produced and β the particle velocity. A measurement of θ_c allows to determine the particle velocity.
For each material there is a minimum velocity $\beta_{threshold}$ (and a corresponding $\gamma_{threshold}$) that the particle must exceed to produce Cherenkov photons.
Simulation studies [Sch 95] predict a typical value $\gamma_{threshold} \approx 12$ so that for electrons and positrons $\gamma \geq \gamma_{threshold}$ and for hadrons and muons $\gamma \leq \gamma_{threshold}$. Since at the energies available with the SIS facility hadrons reach a γ_{max} of about 10, the estimated $\gamma_{threshold}$ imply that the detector is *hadron blind* and hence can more easily trigger on e^+/e^- induced signals only. The requirements of the HADES RICH detector include:

- The detector must be 'hadron-blind'.
- The photon-detector should be placed upstream from the target to minimize the material in the electron trajectories and the background due to charged particles crossing the photon-detector.
- A sufficient amount of photons for each lepton must be detected to enable the reconstruction of the e^+/e^- signature.
- The readout of the detector must be stable at high rates, since the measurements are carried out at high interaction rates (10^6 $collisions/s$) to cope with the small branching ratios (see table 1.1).

The Cherenkov detector that has been built for the HADES spectrometer is shown schematically in figure 2.2. In the center of the detector we find the target, placed in a thin carbon beam pipe. The e^+/e^- produced in the target cross the beam pipe and travel trough the radiator gas, in which only particles with $\gamma \geq \gamma_{threshold}$ will produce Cherenkov light that will be reflected from a spherical mirror. The reflected photons travel trough a CaF_2 window to a two dimensional photon-detector where the Cherenkov cone will be mapped as a ring. The photon-detector is composed of six independent modules. The space resolution of the photon-detector allows to determine the emission angle of the electrons/positrons using the coordinates of the ring center.

One of the detector's tasks is the on-line identification of e^+/e^- during data taking, in order to have a e^+/e^- selection trigger.
In the following subsections the most important properties of the RICH components will be recalled. The HADES RICH is described in details in [Kas 99], [Kas 00].

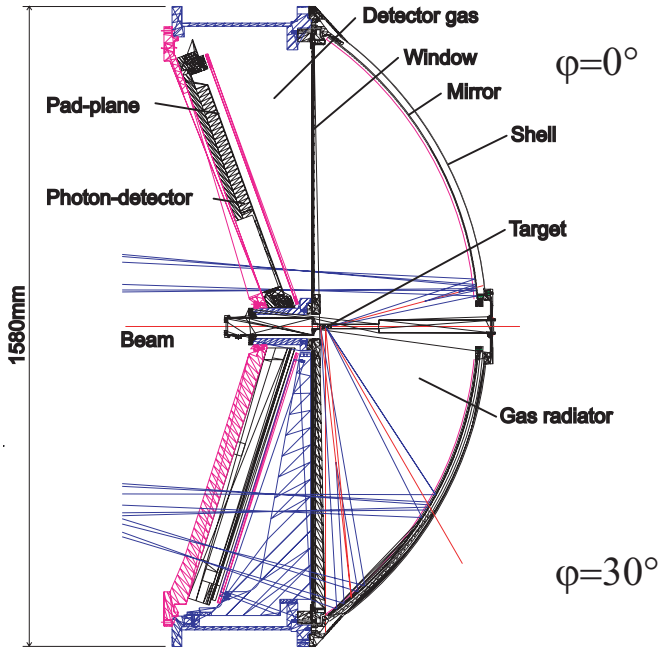

Figure 2.2: Schematic cross-section of the RICH detector. The upper part of the figure shows the detector section taken at azimuthal angle $\phi = 0°$, the lower part at $\phi = 30°$.

2.2.1 The Gas Radiator

The two criteria adopted to choose the gas for the radiator were a $\gamma_{threshold}$ such that only e^+/e^- emit Cherenkov light when they cross the gas and a high transparency in the VUV wavelength range. The chosen gas is C_4F_{10} because it fulfills both requirements reasonably with a $\gamma_{threshold} \approx 18$, the gas transmission is shown in figure 2.6. The photon absorption can increase due to contamination of water and hydrogen in the gas. Therefore the detector gas must be cleaned continuously and it is exchanged every hour. The number of emitted photons for each particle depends on the path length the particle is traveling trough the gas radiator. Figure 2.3 shows the number of photons that reach the CaF_2 window, that separates the radiator gas from the detector gas, as a function of the photon wavelength λ.

In order to minimize multiple scattering the radiation length of the detector gas should be as low as possible. The main contribution to the multiple scattering is due to the radiator gas but there is a contribution due to the **C**arbon **F**ibre **L**aminate (CFL) beam pipe and the CFL tank shell. The corresponding contributions are summarized in table 2.1. The hereby obtained error on the polar angle leads to a resolution in the calculation of the invariant mass of $\Delta M_{inv.}/M_{inv.} \approx 0.5$ % for $p > 400\ MeV$.

2.2.2 The VUV-mirror

The opening angle of the Cherenkov cone of e^+/e^- is about $\Theta_C = 3.18°$, the reflection of these photons leads to the ring image on the photon-detector. The spherical mirror, with a radius $R_{mirror} = 871$mm, reflects the photons to the photon-detector upstream from the target. Since the target is not placed in the center of the mirror but at a

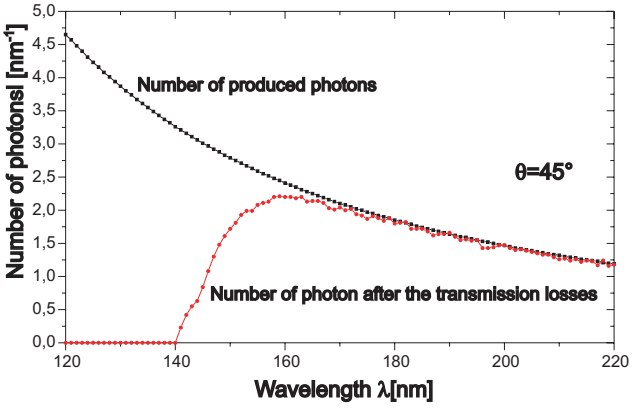

Figure 2.3: Spectral photon distribution in the C_4F_{10} radiator [Kas 00]. The upper curve shows the number of produced photons in the radiator as a function of the photon wavelength, the lower curve the number of photons that reach the CaF window. Both curves have been obtained for a value of the polar angle $\theta = 45°$.

Material	C_4F_{10}	CFL beam pipe	CFL tank shell
Radiation Length X_0 [cm]	3200	30	30
x($\theta = 15$) [cm]	38.5	0.23	0.04
$\Theta_0(\theta = 15)$ [mrad]	2.5	1.9	0.74
x($\theta = 85$) [cm]	67.6	0.06	0.04
$\Theta_0(\theta = 85)$ [mrad]	3.4	0.93	0.74

Table 2.1: Radiation length and multiple scattering contribution for the radiator components. The calculation has been done for electrons with $p \approx 0.5\ GeV/c$ [Kas 00].

distance $d = 0.55 \cdot R_{mirror}$, the radial and focal plane are not overlapping and the pad-plane surface, inclined by 20°, stays in the middle between the two. In this way a compromise between the focusing in the azimuthal and radial direction is achieved [Sch 95].

An additional deformation of the ring images comes from the fact that the photon-detector is not rotationally symmetric. Each of six pagoda-shaped sectors shows a dependency of the ring deformation upon the polar angle. Figure 2.4 shows the photon distribution on the detector pad-plane, simulated by [Kas 00]. One can see that for high polar angles the focusing of the rings become worse and that the deformation increases. This effect can partially be corrected by adjusting the pad dimension to the polar angle such that the solid angle spanned by one pad stays constant. The corrected pad dimension varies from 6.6×4.6 to 6.6×7.1 mm^2 and this leads to an almost constant ring diameter ($\varnothing = 7 - 8$ pads).

The mirror material has to have good optical properties in the VUV range and a low radiation length, in order to minimize multiple scattering and production of secondary photons. The experience made by experiments in astrophysics suggested the usage of a carbon mirror [Iab 96]. The specific material is SIGRADUR G and has a radiation length $X_0 = 28$ cm, that for the 2 mm thick mirror leads to an indetermination in the

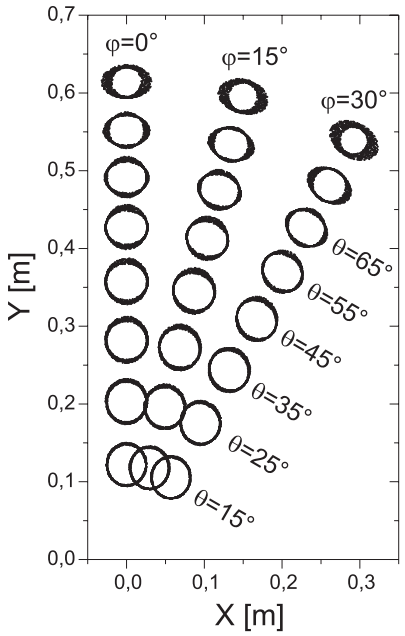

Figure 2.4: Cherenkov ring shapes on the pad-plane as a function of the polar angle before the correction of the pad size [Kas 00]. One can see how the rings become more deformed and less focused with increasing polar angle.

polar angle due to multiple scattering of about $\theta_0 \approx 1.8$ mrad. The chosen material has been coated with a reflective layer of Aluminum and MgF_2 of about $20\mu m$ thickness, the hereby obtained reflectivity is shown in figure 2.6.
Due to its large size, the mirror is be divided in 18 segments that are individually produced and coated.
A description of the production technology and of the obtained results of optical measurements is given in [Fri 03].

2.2.3 The CaF_2 Window

The window is placed between the C_4F_{10} radiator volume and the photon-detector, operating with CH_4 at atmospheric pressure. Two different types of gas have been used for two reasons: first, if C_4F_{10} would be used also in the photon-detector a much lower charge amplification and hence single photo-electron detection efficiency would be achieved. Second the usage of CH_4 in the radiator volume would decrease the photon yield by about 30%.
The window should endure the pressure difference between the two gases ($\Delta p \leq 5$ HPa) and should have a high transparency in the VUV range. The choice of the CaF_2 material is motivated by its very broad transmission range with a minimal cut-off threshold of $\lambda = 130$ nm [Opt 93].
The whole window is composed of 64 hexagonal crystals, each with an outer diameter of 200 mm. The total diameter of the window is 1580 mm.

2.2.4 The Photon-Detector

The photon-detector is composed of six modules, each one being tilted by 20° with respect to a perpendicular position to the beam line and covers an azimuthal angle of 60°. Each module consists of a multi-wire photo-sensitive proportional chamber (MWPC) with a cathodic pad-plane. The pad-plane is coated with a layer of CsI [Fri 99].

Figure 2.5 shows a cross-section of the photon-detector; the cathodic plane and the

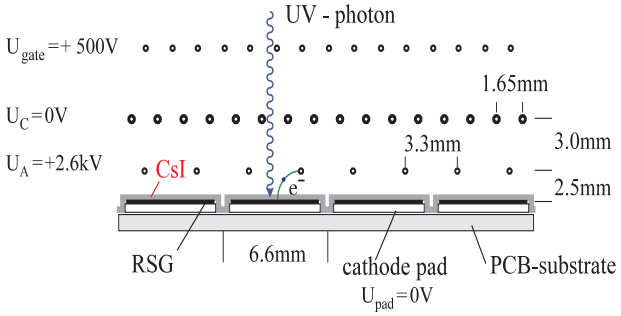

Figure 2.5: Schematic view of the detector pad-plane.

anodic wires are visible. When a photon reaches the pad-plane, there is a certain probability, determined by the quantum efficiency of the CsI layer, that a photo-electron will be ejected. The dependency of the quantum efficiency on the photon

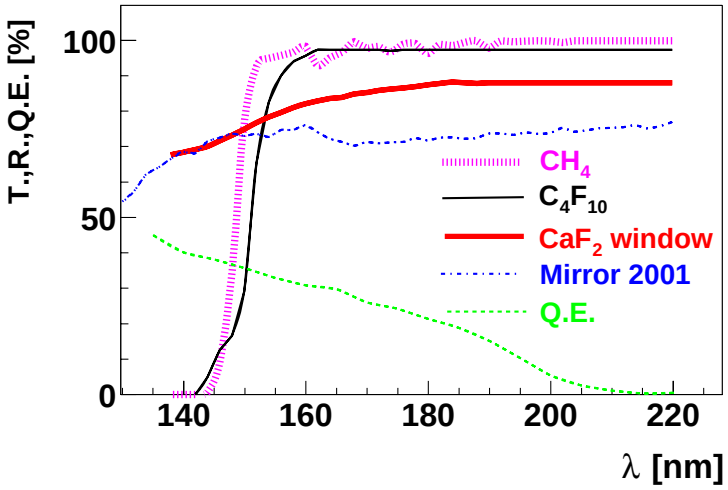

Figure 2.6: Optical parameters of the different detector components. The different curves show: the transmission of the radiator gas (C_4F_{10}) of the CaF_2 window and of the detector gas CH_4, the mirror reflectivity measured in 2001 ($Mirror$ 2001) and the photon cathode quantum efficiency ($Q.E.$). More recent results about the mirror reflectivity are shown in [Fri 03].

wavelength is shown in figure 2.6 [Ger 99]. The emitted photo-electron drifts from the cathodic pad-plane to the anodic wires and generates an avalanche. The produced ions drift back to the cathodic plane and induce a mirror charge on the cathode. Each of the 4712 pads that compose a sector is connected to a preamplifier that registers the pulse height of the charge deposited on it. The amount of charge depends on the total charge produced in the avalanche and on the multiplicity of pads that have been fired. Indeed, a single photon can induce a signal on more than one pad forming a cluster responding on the pad-plane.
Figure 2.6 shows the optical response of all the RICH detector components as a function of the photon wavelength. It can be seen that the single photon efficiency of the whole detector is limited at high wavelengths by the CsI quantum efficiency. Dedicated studies of these optical properties are discussed in chapter 4.

2.3 The Tracking system

2.3.1 Tracking Chambers

The HADES tracking system consists of four multi wire drift chamber planes (MDC I-IV), two before and two behind the magnetic field. Each chamber plane is composed of six trapezoidal modules and has the shape of a frustum. A module covers 60° of the azimuthal angle and module sizes range from 88 cm × 80 cm to 280 cm × 230 cm (height × larger baseline). A chamber module is composed out of six drift cell layers oriented in five different stereo angles (see figure 2.7). These stereo angles (± 40, ± 20, 0 °) have been chosen in order to enhance the precision of position measurement. The cell sizes vary from 5 × 5 mm^2 to 14 × 10 mm^2 from detector I to IV to achieve a constant granularity. The cells are formed by interspersed sense and field wires and cathode wire planes. The total number of drift cells is approximately 27,000. The chamber is filled with counting gas in the ratio: $He : Isobutane = 60 : 40$. When a charged particle passes a drift cell it ionizes the gas. This ionization happens statistically distributed along the track, producing separate clusters of electron clouds drifting to the sense wire acting as the anode. Simulations predict about 35 clusters per cm path length. Hence the ionization closest to the sense wire triggers the signal that is picked up by a fast amplifier connected to the wire. The signal marks the start of the time measurement while the stop signal is given by the START detector. The resulting time must be corrected by the subtraction of the offset and the TDC gain and then be converted into a distance from the sense wire. The last conversion is done using a drift velocity not dependent on the distance of about 4 cm/ms. This leads to an average spatial resolution of about 70 μm. The design value of the MDC detector predicts a momentum resolution of 1.4% for particles with relatively high momentum ($p > 0.5 GeV/c$). This results in a mass resolution of $\frac{\Delta M_{inv}}{M_{inv}} \approx 1\%$. More details about the MDC properties are given in [Bok 02].

2.3.2 The Superconducting Magnet

A good momentum resolution can be achieved only by the use of a high magnetic field. In order to achieve a maximum field intensity of 0.5 T [Sch 95] with the lowest radiation

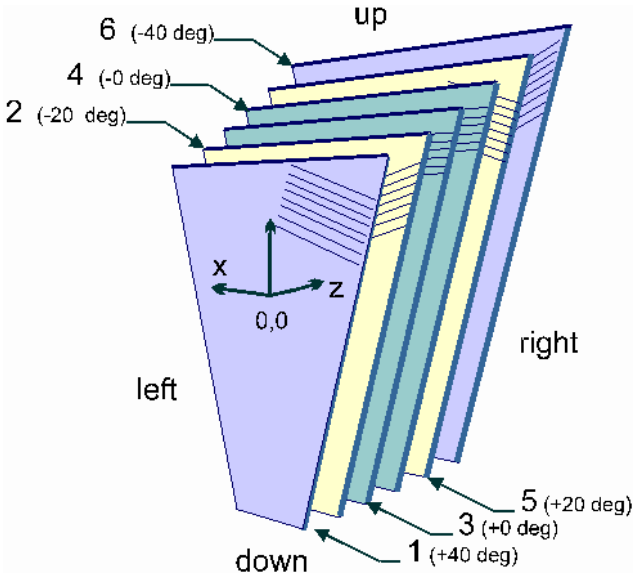

Figure 2.7: Six layers that compose each of the four MDC modules. The orientation of the wires is indicated.

length and the smallest possible size, the usage of a superconducting magnet turns out to be mandatory. The detailed description of the magnet properties can be found in [Bre 99].

2.4 META Detectors

2.4.1 The Time of Flight Wall

(TOF)

The scintillator wall placed behind the tracking system is used for three main purposes:

- A fast determination of the charged particle multiplicity in each event in order to select events by the centrality of the collision.
- The possibility to determine roughly the impact position of each particle in order to allow a fast second level trigger decision.
- The measurement of the time of flight of each detected particle in order to separate electrons and positrons from more massive particles.

The TOF array covers polar angles from 44° to 88° and consists of scintillating rod element structures. The total number of rods in the TOF array is 384 arranged in six sectors of 64 rods. In each sector there are 8 modules of 8 rods enclosed in a special carbon-fiber case (see figure 2.8). The length and the width of the rods increase with larger polar angles such that the cross-section varies from 20 $\times$ 20 mm^2 for the innermost 192 rods to 30 $\times$ 30 mm^2 for the outermost rods. This leads to a finer granularity in the more forward angular region. Each rod is read out by two photomultipliers (PMT) placed at its two ends. Each particle hit provides two signals that

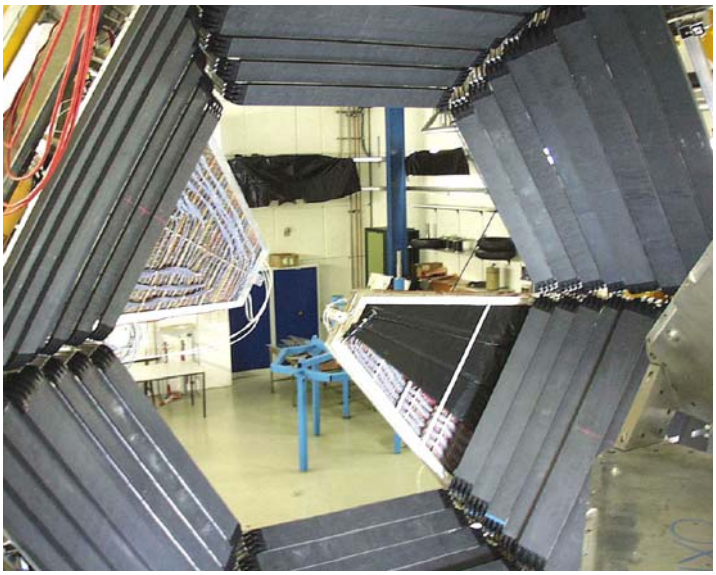

Figure 2.8: Picture of the six sectors of the TOF detector. Two sectors of the Pre-shower detector are visible in the inner region.

allow the determination of the time of flight, the hit position and the deposited energy (ΔE). The achieved time resolution by this detector is between 120-150 ps.
The region between 18° and 44° is covered by the Tofino detector. Like the TOF, Tofino is composed of scintillation paddles, but has a much lower granularity with its four paddles per sector (see figure 2.9). The time of flight measurement is done by means of only one photo-multiplier and the achieved time resolution is about 500 ps. More details about the TOF detector can be found in [Ago 03].

2.4.2 The Pre-Shower Detector

The TOF system provides a particle identification by means of a combination of the time of flight and the momentum measurement. However, at polar angle $\theta < 45°$ the separation between electron and pions and protons is more difficult, due to the higher particle multiplicity and the higher momenta of the hadrons. The estimated yield of tracks that are assigned the wrong particle identity, by the outer and inner TOF detector, is of about 10%.

Therefore at low polar angles, each sector of the META system is composed of one Pre-Shower [Bal 03] module and four Tofino paddles (figure 2.9). The Pre-Shower placed behind the paddles provides a precise hit position measurement.
The Pre-Shower detector is composed of a stack of three trapezoidal wire chambers separated by two lead converter plates. One of the two cathode plane is subdivided into individual pads where the induced charge signal is taken from. The identification of e^+/e^- is based on the recognition of electromagnetic showers that these particles release in the lead converters. Counting and comparing the number of pads before and after the converters by means of integrated charge measurements. This method leads

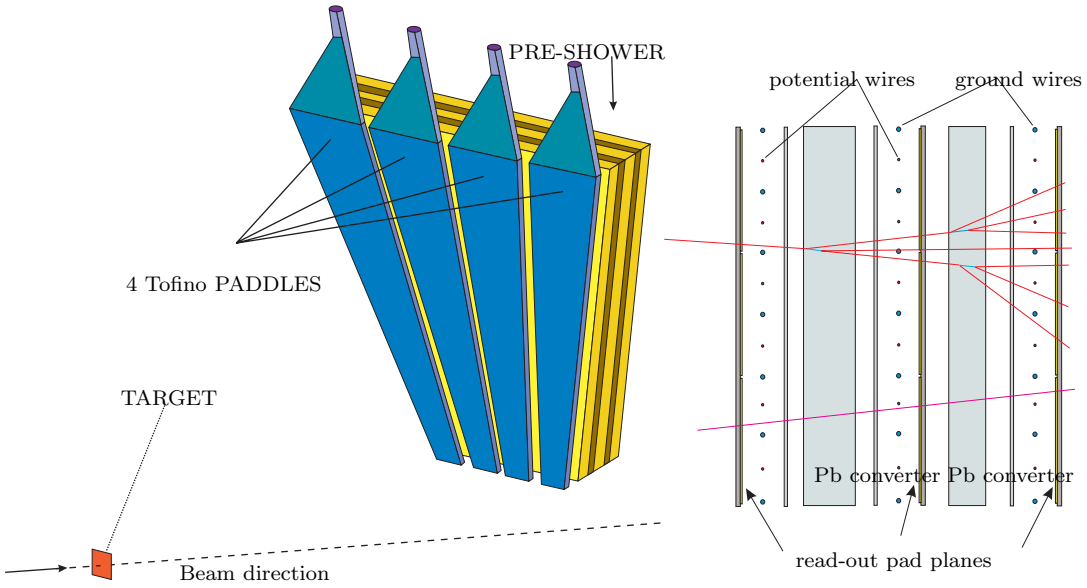

Figure 2.9: Left: Schematic layout of one the Pre–Shower and forward TOF sector. **Right**: Side view of the Pre-Shower detector. Three gas chambers and two lead converters (one sector) are shown. Lepton/hadron discrimination is performed by comparing the charge signal measured in front and behind the lead converters.

to a recognition efficiency of 89% for electrons with high momentum ($p = 850\ MeV$) with a fraction of misidentified particles of 10%. A detailed description of the detector performance can be found in [Bal 03].

2.5 The Selection Trigger

The main task of the HADES trigger system is to discriminate very events containing di-electrons at an interaction rate of $10^6\ s^{-1}$. The aim is the on-line selection of such events. There are three trigger levels that contribute to the event selection.

2.5.1 First Level Trigger

The first level trigger (LVL1) consists of a fast hardware selection of central collisions that makes use of the multiplicity information from the META. When the particle multiplicity exceeds a defined threshold, the event is considered to be peripheral, semi-central or central. Via this discrimination the primary event rate can be reduced by a factor up to 10 ($Au + Au$).

2.5.2 Second Level Trigger

The second-level trigger (LVL2) works in two steps, which is performed by custom designed and programmed electronics, the Image Processing Units (IPUs) and the Matching Unit (MU) [Tra 00]. In the first step the IPUs search for electron signatures.

These are ring images on the RICH pad plane, clusters with the signature of an electromagnetic shower in the Pre-Shower detector, as well as particles with the appropriate time of flight in the TOF and Tofino detector. In the second step the MU correlates the positions of these candidates between the RICH and the META detector to identify leptons, for which the bending in the magnetic field is taken into account. This trigger system currently enables a data reduction by a factor 10 [Toi 03]. If the selection is done on candidate pairs with a minimum opening angle of 20° the reduction factor should go up to 100. A detailed description of the trigger concept and development can be found in [Leh 00], [Pet 00], [Lin 01].

2.5.3 Third Level Trigger

The third level trigger (LVL3) performs a consistency check of the electron candidates determined by the second level trigger by evaluating the hit pattern of the wires from the MDC modules. It gains another reduction factor of 10 that brings the final event rate to the order of 100 Hz. At the moment the experiment is running with the application of the LVL1 and LVL2 triggers only.

Chapter 3

Expected e^+e^- spectra for C+C

The HADES experimental program includes among others the investigation of the system $^{12}C + ^{12}C$.
As discussed in 1.1.2 this system was already studied by the DLS collaboration [Por 95], but the interpretation of the experimental results is still very controversial. The HADES spectrometer, with its high acceptance and high momentum resolution aims to investigate this problem and get to a more concluding result.
The first set of measurements between fall of 2000 and 2001 were carried on with an incomplete tracking system. Only the inner two MDC planes before the magnet were included in the setup and the particle momenta were calculated via the *kickplane method* [San 03], (see section A.5). The limited precision of the position information after the magnet leads to a momentum resolution of about 4%. All the other subdetector systems were complete.
A full-scale simulation of the HADES spectrometer was carried out first in 1995 [Sch 95] as input of the technical proposal for the experiment. Since many technical aspects of the spectrometer have changed and especially the digitization and analysis software have been newly developed, new simulations for the $^{12}C + ^{12}C$ system have been performed for the above experiment in the framework of this thesis. In particular, the signal to background ratio in the e^+e^- invariant mass spectrum was investigated, with emphasis on the reduced set-up. Additionally the amount of beam-time needed to collect sufficient statistics was investigated.

3.1 Input

The expected di-electron production rates for the reaction system $^{12}C + ^{12}C$ at two different energies have been investigated via simulations. The calculations have been done for two energies: $E_{lab} = 1\ AGeV$, which is below threshold for $\eta,\ \rho,\ \omega$ production in free nucleon-nucleon collisions, and the maximum SIS energy $E_{lab} = 2\ AGeV$ to allow for sufficient production of $\eta,\ \rho,\ \omega$ and eventually also ϕ mesons.
As input for the simulation a Boltzmann distributed isotropic source for each type of particles has been produced. Each particle distribution has been calculated using the Pluto package [Plu 00], that, given the average particle multiplicities per event and the source temperature (dependent on the beam energy), generates the isotropic source.
Therefore, the mean multiplicities per event of the different particles types and the estimated temperature for the system at the two beam energies are needed. The average multiplicities per event for neutrons and protons have been taken from UrQMD

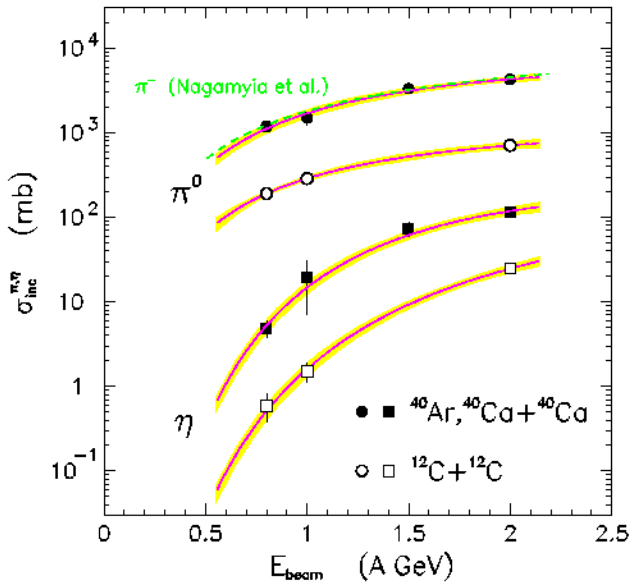

Figure 3.1: The inclusive π^0 and η cross sections in the $A_{proj} + A_{targ} = 12 + 12$ and $40 + 40$ systems are shown as function of the bombarding energy [Hol 97]. The solid lines represents polynomial fits to the data (see text for details).

calculations [Ern 98] (see section A.4).
The average multiplicities for π^0 and η were measured by the TAPS collaboration [Hol 97] at GSI. The TAPS experimental program includes the measurement of neutral mesons produced in heavy ion reactions. The measurements covered a wide range of reaction systems (from C + C to Au + Au) with beam energies varying from 0.8 to 2 $AGeV$ [Ave 97].
In figure 3.1 the inclusive cross-sections of the neutral mesons π^0 and η are shown as a function of the beam energy for two different systems. Together with the data polynomial fits are shown. The TAPS experiment measured the inclusive cross section for neutral meson in the rapidity[1] interval $0.42 < Y < 0.74$. The full solid angle cross-sections have been extrapolated using a fireball [Cug 81] model for the particle emission. In table 3.1 the extrapolated inclusive π^0 and η multiplicities for the system

E [GeV]	$< M >^{4\pi}_{\pi_0}$ $[10^{-4}]$	$< M >^{4\pi}_{\eta}$ $[10^{-4}]$	T [MeV]	$P^{\pi^0}_{part}$ $[10^{-4}]$	P^{η}_{part} $[10^{-4}]$
1.0	3350±2.5	17±5	54±3	560±0.4	3.2±0.8
2.0	8260±8.4	294±46	83±2	1380±1.4	49±8

Table 3.1: Inclusive measured meson multiplicities per event and the production probability per participant for the system ^{12}C + ^{12}C at 1 and 2 $AGeV$.

^{12}C + ^{12}C at 1 and 2 $AGeV$ are shown. Together with the measured neutral mesons multiplicities per event and the production probability per participant, the source tem-

[1]The rapidity of a particle is defined in terms of its energy-momentum components p_0 and p_Z by $Y = \frac{1}{2}\ln\left(\frac{p_0+p_Z}{p_0-p_Z}\right)$

peratures (T) for both beam energies are listed.
These temperature values were extracted from the transverse mass (m_t) distribution of the neutral mesons, as shown in [Ave 97]. The variable m_t exhibits the transverse momentum distribution and is defined as:

$$m_t^2 = m^2 + p_t^2. \tag{3.1}$$

where m is the particle rest mass and ${p_t}^2$ the transverse component of the particle momentum. The experimental m_t distributions of π^0 and η were fitted with the expression $\frac{d\sigma}{dm_t} = m_t^2 \cdot \exp\left(-\frac{m_t}{T}\right)$, which corresponds to a thermal-equilibrated and isotropic source. The parameter T extracted from the fit of the π_0 and η m_t distributions is found to be the same, the value is shown in table 3.1. This approximately universal behavior with respect to m_t is called m_t *scaling* [Bour 76],[Ber 94].
A schematic representation of the m_t scaling is shown in figure 3.2, where the $\frac{1}{m_t^2}$ corrected differential cross-sections for the mesons π^0, η and ω are schematically depicted. The lower threshold of each distribution represents the rest mass of the corresponding meson. The figure shows that the distributions have the same slope for π^0 and η and it is assumed that the same is valid for the ω meson. The integral of the distribution starting from the meson rest mass gives the production cross-section for each meson. Hence, from the experimentally known π_0 and η cross-sections those for ω, ρ and ϕ have been estimated. The common temperature parameter is used to generate the Boltzmann distribution of each particle species. The Δ production cross-section is

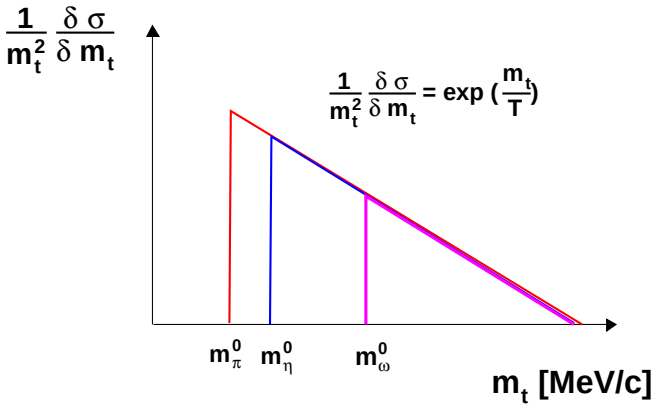

Figure 3.2: Schematic representation of the m_t scaling. The m_t distribution of π^0, η and ω is schematically depicted.

related to the π^0 cross-section and has been estimated a factor $\frac{3}{2}$ larger [Bas 95]. The

[2]The transverse momentum p_t of a particle is the momentum component perpendicular to the beam axis. $p_t = \sqrt{(p_x^2 + p_y^2)}$

pn-bremsstrahlung production was determined by fitting the UrQMD simulated spectrum. For our calculations, two centrality selections have been considered: a detected charged particle multiplicity M ≥ 2 corresponding to 97% of all C+C interactions (inclusive measurement) and M ≥ 6 for semi-central events corresponding to $\simeq 40\%$ of the total reaction cross section.
The particle multiplicities for the inclusive and semi-central collisions have been estimated via a scaling law [Ave 97]:

$$\sigma^{\pi^0}_{inclusive} = \sigma_{reaction} < A_{part} >_{inclusive} P^{\pi^0}_{part}, \tag{3.2}$$

$$\sigma^{\pi^0}_{semi-central} = \sigma_{reaction} < A_{part} >_{semi-central} P^{\pi^0}_{part} \tag{3.3}$$

where $\sigma_{reaction}$ is the reaction cross section, $< A_{part} >$ the number of participants and $P^{\pi^0}_{part}$ is the average π^0 production probability per participant.
The total reaction cross section has been calculated assuming that the target and the projectile are spherical.

$$\sigma_{reaction} = \pi \cdot (1.14\ fm)^2 \cdot \left(A_P^{\frac{2}{3}} + A_T^{\frac{2}{3}} \right), \tag{3.4}$$

where A_T and A_P are the mass numbers of the target and projectile nuclei respectively. For the system $^{12}C + ^{12}C$ a reaction cross-section $\sigma_{reaction}$=0.86 b was obtained [Ave 97].
The average number of participants is taken from a geometrical modeling of the overlap volume and averaging over the impact parameter [Cug 81]. For the $^{12}C + ^{12}C$ system $< A_{part} > = 6$ has been obtained for the inclusive reaction and $< A_{part} > = 12$ for the semi-central reaction. The average π^0 and η meson production probabilities $P^{\pi^0}_{part}$ and P^{η}_{part} are listed in table 3.1.

All the other particle multiplicities are scaled with the same factor used for π^0.
In table 3.2 the particle multiplicities per event calculated for the semi-central collisions are listed together with those corresponding to the inclusive reaction. One sees that the meson multiplicities per event are enhanced by a factor 1.6 - 2 between the

	inclusive		semi-central	
	1 *AGeV*	2 *AGeV*	1 *AGeV*	2 *AGeV*
π^0	0.33	0.83	0.68	1.71
η	$1.8{\cdot}10^{-3}$	$2{\cdot}10^{-2}$	$3{\cdot}10^{-3}$	$4.3{\cdot}10^{-2}$
ω	$7.3{\cdot}10^{-5}$	$2.5{\cdot}10^{-3}$	$2.1{\cdot}10^{-4}$	$4.8{\cdot}10^{-3}$
Δ	0.5	1.3	1.02	2.56
p	2.6	2.6	5.5	5.5
n	2.6	2.6	5.5	5.5
d	0.26	0.26	0.55	0.55
pn	$1.0{\cdot}10^{-4}$	$1.8{\cdot}10^{-4}$	$2{\cdot}10^{-4}$	$3.6{\cdot}10^{-4}$

Table 3.2: Emitted particle multiplicities per collision, used as input for the inclusive and semi-central collisions of the system C + C at 1 and 2 *AGeV*.

Source	Mass [Mev/c^2]	Decay Width [Mev/c^2]	[fm/c]	Final State	Probability	e^+e^-	Probability
Dalitz Decay of the pseudo-scalar mesons							
π^0	135	0.78	251	$\gamma\gamma$	98.8%	γe^+e^-	1.2%
η	550	0.001	$>> 30$	$\gamma\gamma$	38.8%	γe^+e^-	0.5%
Two-body-Decay of the vector-mesons							
ρ^0	768	152	1.3	$\pi^+\pi^-$	100%	e^+e^-	$4.6{\cdot}10^{-5}$
ω	782	8.43	23.4	$\pi^+\pi^-\pi^0$	89%	e^+e^-	$7{\cdot}10^{-5}$
ϕ	1019	4.43	44.4	K^+K^-	49%	e^+e^-	$3{\cdot}10^{-4}$
Δ decays							
Δ	1232	115	1.7	Nπ	99%	Ne^+e^-	$4{\cdot}10^{-3}$

Table 3.3: Particle masses and branching ratios of di-electron decay channels.

inclusive and semi-central reactions.

The branching ratios of the particle decays in di-electron pairs are shown in table 3.3. In order to propagate the particle tracks in the HADES spectrometer the GEANT [Gea] package adapted for the geometry of the spectrometer (HGeant) has been used. Since this program processes only the di-electron pairs decay of π^0 and η mesons, the other particles are let to decay into e^+e^- channels already in the Pluto framework, where the Boltzmann distribution is computed. The decay products together with the π^0 and η particles are used as input for the HGeant simulation.

3.2 Analysis of simulation data

3.2.1 General procedure

The HGeant package propagates all reaction products and in particular the e^+/e^- tracks through the spectrometer, providing the information of the position where the different tracks crossed the sub-detectors.
The set-up used for these simulations is composed of:

- a fully equipped RICH detector,
- 2 MDC plane before the magnet (MDC 1/2) and one MDC plane after the magnet (MDC 3),
- fully equipped TOF and Tofino detectors,
- fully equipped Pre-Shower detector.

The hit information provided by HGeant is general different from the signal registered for the experimental data. For this reason the hit position information must be converted into detector signals in the simulations. This process goes under the name of "hit digitization". The digitization of the RICH detector is described in detail in section 4.2.3, the other sub-detector digitizers are described in [Zov 03], [Mar 03], [**?**].

In this analysis, the response of the spectrometer for a perfect tracking system has been investigated. For this, the ideal momentum reconstruction delivered by the HGeant program has been used.
For all the identified particles it is checked if a ring has been found. The Geant track number that identifies the ring must match with the track number of the particle propagated in the other sub-detectors. If these conditions are satisfied a e^+/e^- is recognized. To each e^+/e^- candidate the momentum calculated by the HGeant program is assigned. This momentum is than smeared according to the resolution expected by the employment of both inner MDC planes (MDC 1/2) and one outer plane (MDC 3). With this setup a momentum resolution $\Delta p/p \approx 1.0 + 3.6 \cdot p[\%/GeV/c]$ is expected, i.e. about 4% resolution in the ρ/ω region.
After the single track reconstruction the e^+/e^- tracks can be combined into unlike-sign pairs. The invariant mass of the pair is defined as:

$$m_{pair} = \sqrt{(E_{e^+} + E_{e^-})^2 - (\vec{p}_{e^+} + \vec{p}_{e^-})^2}. \tag{3.5}$$

Where E_{e^+/e^-} is the energy of the e^+/e^- and p_{e^+/e^-} the three-momentum. Since the rest mass of e^+/e^- is small as compared to its momentum, one can approximate E $\approx$ $|p|$ and calculate the invariant mass using only the three-momenta:

$$m_{pair} = \sqrt{2 \cdot p_{e^+} p_{e^-} (1 - cos\Theta_{e^+e^-})}, \tag{3.6}$$

where p_{e^+}, p_{e^-} are the three-momenta of the two particles and $\Theta_{e^+e^-}$ is the pair opening angle.
The total invariant mass spectrum for the unlike-sign pairs is built in the following way: the contribution of each particle species to the total signal is calculated separately ("cocktail contribution") and then the combinatorial background is evaluated and added to the cocktail spectrum.

3.2.2 Background contribution

When the pairs are created in principle all the possible e^+e^- combinations have to be built up. As shown in figure 3.3, a π^0 can decay in γe^+e^- (BR($\pi -> \gamma\ e^+e^-$) = 1.2%) and in the same event a γ can convert in a e^+e^- pair (BR($\gamma -> e^+e^-$) = 3% in the target and gas radiator). In this case, if it is not possible to distinguish between the vertex of the first and second pair, all the pair combinations have to be considered. The reconstructed signal will be composed of the pairs: $e_1^+e_1^-$, $e_2^+e_2^-$, $e_1^+e_2^-$, $e_2^+e_1^-$. The first two pairs correspond to the real signal, the last two contribute to the so-called *combinatorial background*.
The same can be applied to the case $\pi^0 -> \gamma\gamma$ (BR = 98%) and $\gamma -> e^+e^-$ or if the e^+e^- produced by the decay of different particles (e.g Dalitz-decay of π^0 and η) are combined.
For the simulated pair spectra it is possible to evaluate which of the reconstructed pairs belong to the signal and which to the background. Figure 3.4 shows the contribution to the combinatorial background from the different channels. One can see that the main contribution comes from the π^0-Dalitz decay and from the γ conversion processes. The

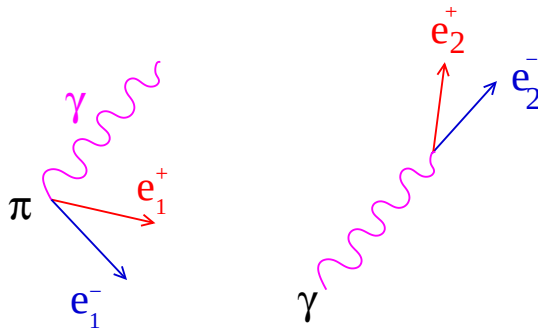

Figure 3.3: π^0-Dalitz and γ-conversion products. The contribution to the combinatorial background is given by the combination of e^+e^- that do not stem from the same particle (e.g. the pair $e_1^+e_2^-$)

media where the di-electron production takes place are indicated in figure 3.4. All π^0-Dalitz decay in the target, while most of the γ-conversion happens in the RICH detector radiator. The contribution from Compton-scattering is much smaller than the contribution of the other two processes.

The background contribution can be reduced if the pairs from conversion and π^0 Dalitz

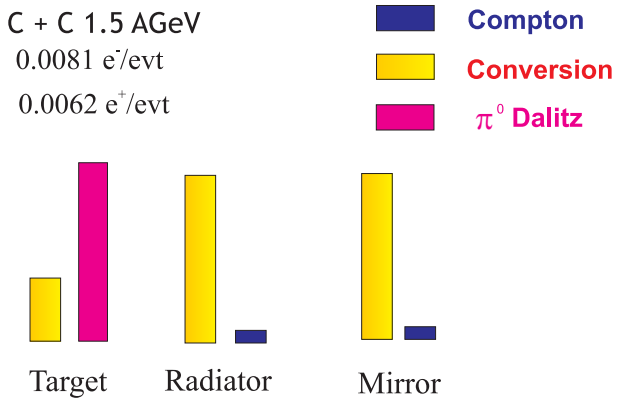

Figure 3.4: The contribution to the combinatorial background from the different mechanisms is shown. The number of e^+e^- tracks per events that compose the background is indicated together with the media where the di-electron pairs are produced.

decays are identified and both pair-partners are removed from the lepton ensemble. The characteristic feature of these pairs is a very small opening angle (for C + C at 2 $AGeV$ $< \alpha >_{\pi^0-Dalitz}= 18°$, $< \alpha >_{Conversion}= 3°$, see [Sch 95]). Their detection requires a good two-track resolution in the RICH and in the inner tracking detectors, in which the trajectories of the oppositely charged tracks are not yet separated by the action of the magnetic field. The resolution of the RICH detector is limited by the pad granularity and corresponds to about 1°. This implies that almost 70% of the conversion pairs will be mapped to a single ring on the photon-detector. In these cases the resolution of the tracking chambers plays the most important role in the identification of the two

candidates.
The opening angle cut has been applied for two different scenarios. In the first case only those tracks for which two rings were found on the RICH detector can build a pair, in the second case the ideal tracking is used to calculate the pair opening angle even if only one ring has been recognized. In figure 3.5 it is shown how possible event

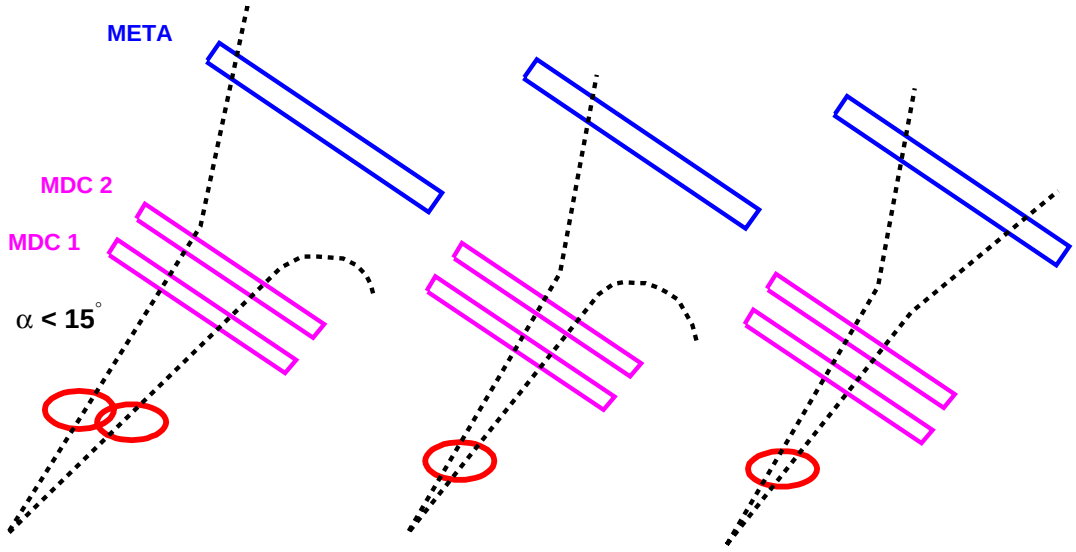

Figure 3.5: Characteristic event patterns induced by e^+e^- background-pairs from π^0-Dalitz and conversion in the RICH and MDC detectors. *left*: two rings are identified for the open pair, one of the candidates is bent out of the acceptance, *center*: only one ring is identified in the RICH detector,*right*: both pair candidates are tracked to the META detector.

patterns induced by a background pair may look like. A crucial point is that, due to the low e^+/e^- momenta in these decays, it is very probable that one of the two pair members will be bent out of the acceptance by the magnetic field. In this case one of the particles will not be tracked trough the whole spectrometer and only one partner will be correctly reconstructed. This will enhance the combinatorial background. Hence the cut on the opening angle must be applied on the track-segments before the magnetic field.
Tracks forming pairs that do not fulfill the opening angle cut are removed from the e^+e^- ensemble. An opening angle cut of 15° has been applied.
Furthermore, accidental assignments of high momentum pion tracks to nearby centers of ring candidates from low momentum electrons ($\pi^\pm/e^\pm$ misidentification) also add to the combinatorial background. Protons and low momentum pions do not contribute, since they can be identified using the time of flight information.

The contribution from $\pi^{\pm}/e^{\pm}$ misidentification is estimated from the distribution of relative angles between pions of momentum p$\geq$ 500 MeV/c and electrons (p$\geq$ 100 MeV/c) detected in the RICH. For E = 2 $AGeV$ beam energy a probability of $2.8 \cdot 10^{-3}$ per primary electron has been found, that a $\pi^{\pm}/e^{\pm}$ pair is observed with an opening angle of $\leq$ 3 degrees. The contribution to the combinatorial background under such conditions seems to be negligible.
A statistical procedure has been used to build the invariant mass spectrum for the combinatorial background. There are two main techniques to compute the background: the like-sign technique and the event mixing technique [Her 01]. Both work successfully in absence of correlated background, that in first approximation can be neglected, since the ideal Geant tracking has been used. The starting point is in both methods the assumption that electron and positron multiplicity distributions are Poisson functions. The like-sign technique method is based on the fact that the same-event combinatorial like-sign background is identical to the unlike-sign combinatorial background. This is exactly true only under the assumption that the acceptance and the efficiency for electrons and positrons is the same. It can be shown [Her 01] that the mean unlike-sign combinatorial background is given by twice the geometrical mean of the like-sign pairs:

$$N_{+-}^{Comb.} = 2 \cdot \sqrt{N_{++} N_{--}} \tag{3.7}$$

In the mixed-event technique the background is built combining tracks from different events into unlike-sign pairs. This second method has been used mainly because it reduces the computation time.
Given two events A and B all the e^+ candidates in A with the e^- candidates in B have been combined with one another and vice-versa. The events in which only one candidate was found have been also included. The opening angle for the track selection is applied to each formed e^+e^- pair as well. In this case, if the opening angle of one pair is below 15° the pair is rejected but the two tracks are further combined to the other candidates. For each formed pair the invariant mass can be calculated and the unlike-sign mixed-event distribution can be built.
The mixed-event combinatorial background is obtained normalizing the unlike-sign mixed-event distribution in the following way:

$$< n_{+-}^{mixed} >= \frac{N_{exp}}{N_{mixed}} < n_{+-}^{mixed} >^{AB} \tag{3.8}$$

where N_{exp} is the total number of analyzed events, including those in which no e^+e^- was found, N_{mixed} the number of event-pairs that have been mixed. Finally the combinatorial background yield $< n_{+-}^{mixed} >$ has been evaluated using the unlike-sign mixed-event yield $< n_{+-}^{mixed} >^{AB}$.

3.3 Results

A total of $5 \cdot 10^5$ events has been processed for the system C + C at 1 and 2 $AGeV$. The calculations have been performed for the two centrality conditions mentioned above (see section 3.1). The semi-central events ($M_{Char.P.} \geq 6$) reduces the collision rate by

roughly a factor 2.5 as compared to the minimum bias condition.
Since the calculations were performed for the first run of the HADES spectrometer, a moderate primary beam intensity $I \approx 2 - 5 \cdot 10^6/s$ has been assumed, that together with a 1% interaction target leads to a first level trigger rate of $1 \cdot 10^4/s$. An additional reduction factor of 10 by the Second Level Trigger has been required, since this device was at that time still under testing. The resulting event building and taping rate is then $1 \cdot 10^3 events/s$.
A charged particle detection efficiency of 98% has been assumed for the MDC and TOF/Tofino detector, as measured in the commissioning runs. The single lepton efficiency of the RICH detector was estimated from simulation to 50% ($\theta = 20°$) and 90% ($\theta = 80°$) for $p > 50\ MeV/c$. For the Pre-Shower detector the measured charge particle detection efficiency is 98% and the single electron efficiency ranges from 40% (p = 0.2 GeV/c) to 90% (p = 1.0 GeV/c). The total track reconstruction efficiency for e^+e^- pairs inside the acceptance was estimated to be about 70%.
These correction factors have been to scale the reconstructed invariant mass spectrum in order to obtain a realistic di-lepton yield per day.
The obtained invariant mass spectra obtained for the semi-central collisions are shown in figure 3.6 and figure 3.7. The two pictures show the contribution to the signal coming from the different particles and the combinatorial background obtained with the mixed-event technique.
Two methods have been used to calculate the combinatorial background. The lower dashed curve in figure 3.6 shows the results obtained for the best scenario, in which all leptons triggered by a ring in the RICH detector can perfectly be resolved. The upper dashed curve was obtained for the worst case, for which only those pairs corresponding to two identified rings in the RICH detector can be resolved. It can be seen that there is a huge difference in the combinatorial background yield between the two cases.
The total invariant mass spectrum shown in figure 3.6 and figure 3.7 (continuous black line) was obtained summing up the cocktail contributions with the lower combinatorial background curve. The data points are obtained sampling with a Poisson distributions the values on the black line. The error bars account for the statistical error only.

It has been estimated that within 5 days (43200 s/day at 50% duty cycle) of beam $2.16 \cdot 10^9$ events can be recorded. This should lead for E = 1 $AGeV$ to a total number of 25100-50300 reconstructed e^+e^- pairs of and about 350-700 in the 200-600 MeV/c^2 mass region for the two centralities, respectively. At 2 $AGeV$ incident energy the total yield is a factor 3.6 higher and about 2100-4200 e^+e^- pairs in the 200-600 MeV/c^2 mass region are expected.
Table 3.4 shows the contribution of the different channels to the total invariant mass spectrum for inclusive reactions. In the same table the integral of the combinatorial background distribution is shown for the two scenarios.
One can see that the lowest background curve leads to a signal to background ratio of about 2 for E = 1 GeV and of about 5 for E = 2 GeV at $M_{e^+e^-}$=300 MeV/c^2. For the higher background the ratio changes to 0.3 and 0.7 for the two beam energies, respectively.
One important result of these simulations is that the signal to background ratio depends mainly on two parameters: the double-track resolution and the single lepton efficiency of the RICH detector. For this reason it is necessary to evaluate the efficiency of the

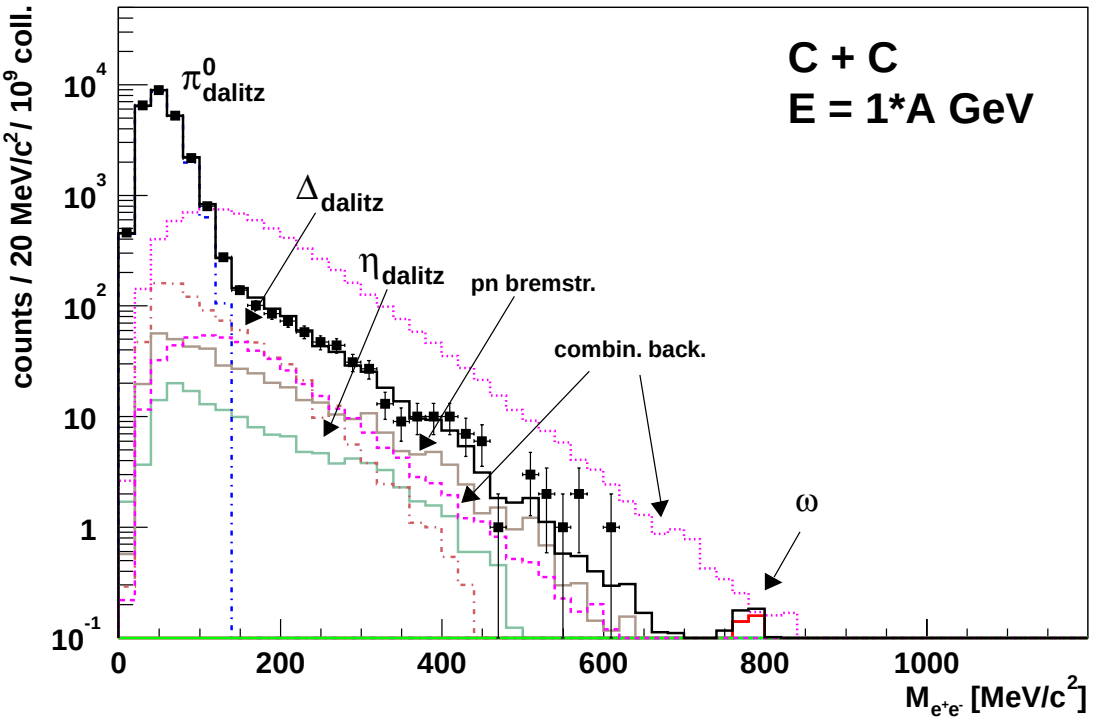

Figure 3.6: Simulated invariant mass spectrum of e^+e^- pairs for C + C at $E_{Kin} = 1AGeV$. The total yield (squares and solid histogram) of ≈ 5000 pairs is expected for $2 \cdot 10^9$ semi-central collisions (40% of the total cross-section). In the ρ/ω region about 4 counts are expected. The error bars reflect pure statistical errors. The combinatorial background is calculated for two scenarios of close pair rejection. The upper curve corresponds to the double ring recognition in the RICH only, the lower curve to the ideal track resolution (see text for details).

RICH detector quantitatively, in order to calculate more carefully the contribution of the combinatorial background to the total signal.
In the following chapters of this work the detailed analysis of the RICH detector response will be described and results concerning the efficiency shown.

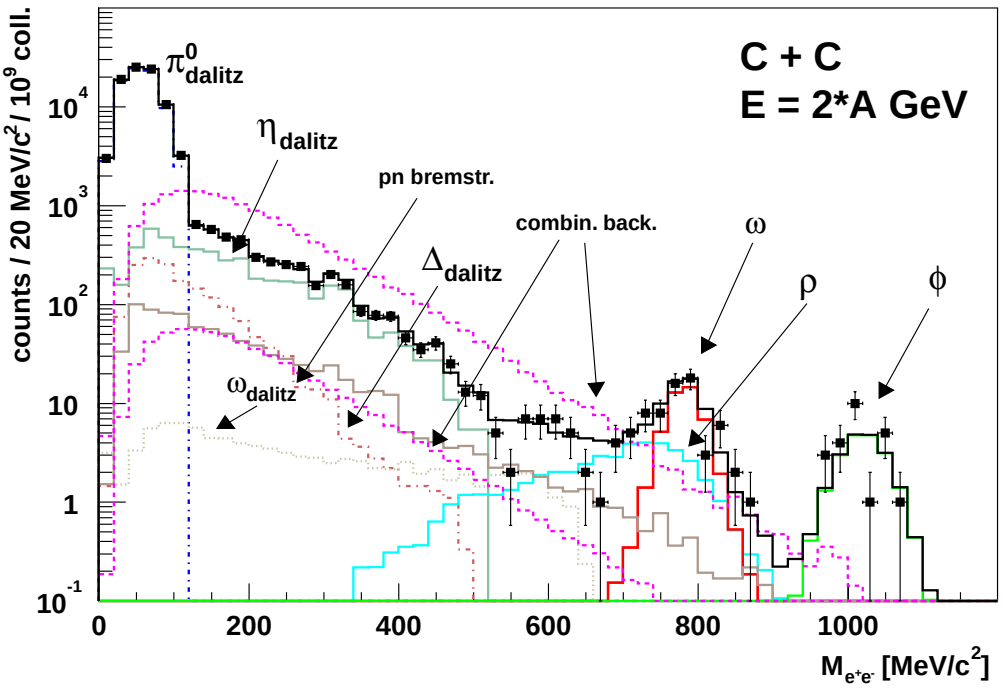

Figure 3.7: Simulated invariant mass spectrum of e^+e^- pairs for C + C at $E_{Kin} = 2\ AGeV$. The total yield (squares and solid histogram) of $\approx$ 180000 pairs is expected for $2 \cdot 10^9$ semi-central collisions (40% of the total cross-section). In the ρ/ω region about 180 counts are expected. Errors and combinatorial background are treated like in figure 3.6

.

Table 3.4: Contribution of the different channels to the total di-lepton yield in C+C collisions. Given are the average total multiplicities $< M_{e^+e^-} >$ of reconstructed di-lepton decays per collision for a minimum bias measurement ($M \geq 2$). The number of pairs detected in one day within the full azimuthal acceptance is calculated with a beam intensity of $\simeq 2 \cdot 10^6/s$. The range of combinatorial background corresponds to the two limits given in figure 3.6 and figure 3.7.

	E=1 AGeV	T=55 MeV	E=2 AGeV	T=89 MeV
Channel	$< M_{e^+e^-} >$ [per coll.]	Yield [per day]	$< M_{e^+e^-} >$ [per coll.]	Yield [per day]
$pn_{\,brems}$	$2 \cdot 10^{-7}$	$8.4 \cdot 10^{1}$	$4.0 \cdot 10^{-7}$	$1.7 \cdot 10^{2}$
π^0_{dalitz}	$1.1 \cdot 10^{-5}$	$4.6 \cdot 10^{3}$	$3.7 \cdot 10^{-5}$	$1.6 \cdot 10^{4}$
$\eta_{\,dalitz}$	$6.7 \cdot 10^{-8}$	$2.9 \cdot 10^{1}$	$2.2 \cdot 10^{-6}$	$9.7 \cdot 10^{2}$
$\Delta_{\,dalitz}$	$4.2 \cdot 10^{-7}$	$1.8 \cdot 10^{2}$	$7.6 \cdot 10^{-7}$	$3.3 \cdot 10^{2}$
$\omega_{\,dalitz}$	$4.6 \cdot 10^{-10}$	0.2	$4.4 \cdot 10^{-8}$	$1.9 \cdot 10^{1}$
ρ	$4.5 \cdot 10^{-10}$	0.2	$2.1 \cdot 10^{-8}$	9
ω	$2.3 \cdot 10^{-10}$	0.1	$2.0 \cdot 10^{-8}$	8
ϕ	$< 4 \cdot 10^{-11}$	0	$1 \cdot 10^{-8}$	4
comb. backgr.		90-2200		230-5700

Table 3.5: Expected yield of detected e^+e^- pairs in the full HADES acceptance for 5 days of beam-time. The numbers are given for minimum bias (M $\geq$ 2) and semi-central (M $\geq 6, 40\%$ of reaction cross section) trigger conditions and a first level trigger rate of $10^4\,s^{-1}$. Combinatorial background is not included (for an estimate see Fig. 3.6 and Fig. 3.7).

Ch. Part. Mult.	Inv. mass range $[MeV\,/\,c^2]$	E=1 $AGeV$ Yield	E=2 $AGeV$ Yield
2	0 - 1200	$25 \cdot 10^3$	$89 \cdot 10^3$
2	200 - 600	$3.5 \cdot 10^2$	$2.1 \cdot 10^3$
2	600 - 900	2	93
6	0 - 1200	$50 \cdot 10^3$	$178 \cdot 10^3$
6	200 - 600	$7.0 \cdot 10^2$	$4.2 \cdot 10^3$
6	600 - 900	4	186

Chapter 4

RICH performance and single photon efficiency

4.1 On-line Efficiency Measurement (OEM)

4.1.1 Motivations

The performance of the RICH detector depends on several parameters of which the most crucial one is the number of photons detected per lepton that travels through the gas radiator. In a material where emission of Cherenkov photons takes place, the number of emitted photons per energy and path length interval is :

$$\frac{d^2N_\gamma}{dE_\gamma dl} = \frac{Z^2\alpha}{\hbar c}\left(1 - \frac{1}{n_0^2\beta^2}\right) = \frac{Z^2\alpha \sin^2\theta_c}{\hbar c}, \tag{4.1}$$

where E_γ is the photon energy, l the path length of the particle in the material where the Cherenkov emission occurs, Z the effective charge of the incoming particle, α the fine structure constant, $n(E)$ the refraction index of the material, β the particle velocity and θ_c the emission angle of the Cherenkov photons. Assuming that the particle travels on average a known path length l_{rad} and integrating over the energy, the total number of emitted photons per particle can be calculated.

$$N_\gamma = \frac{Z^2\alpha l_{rad}}{\hbar c}\int_{E_{min}}^{E_{Max}} \sin^2\theta_c \cdot dE_\gamma. \tag{4.2}$$

The number of detected photons decreases due to losses in the optical media that compose the detector. The product of the optical properties of all the detector components determines the detector efficiency. The detector performance is characterized by a factor called figure of merit (N_0) that accounts for the total efficiency and is calculated in the following way [Ger 98]:

$$N_0[cm^{-1}] = 370\int_{E_{Min}}^{E_{Max}} \epsilon(E_\gamma)\cdot dE_\gamma. \tag{4.3}$$

where $\epsilon(E_\gamma)$ is the product of the optical parameters of the detector components that depend on the photon energy. In the case of the HADES RICH detector $\epsilon(E_\gamma)$ includes:

- the transmission of the gas radiator (C_4F_{10}),
- the mirror reflectivity,
- the transmission of the window (CaF),

- the transmission of the detector gas (CH_4),
- the quantum efficiency of the CsI layer on the photon-detector,
- the single electron detection efficiency of the MWPC,
- the geometrical losses due for example to MWPC wires and the edges of hexagonal crystals of the window.

Figure 2.6 shows the optical properties of the different detector components as a function of the photon wavelength. These values have been obtained from measurements on small samples in the laboratory. Using the equation (4.3) , a N_0=112 has been calculated.
The total number of detected photons per lepton is given by:

$$N_{\gamma det} \approx N_0 Z^2 l_{rad} \overline{sin^2\theta_c} \tag{4.4}$$

where l_{rad} is the lepton path length in the C_4F_{10} radiator, the place where the Cherenkov emission takes place. Assuming an average path length of about 40 cm, $Z^2 = 1$ for e^+/e^-, a Cherenkov angle of about 3.18° and a value of N_0=112, equation (4.4) predicts 14 photons detected for each lepton. The value N_0 equal to 112 corresponds to the design value of the detector, it was calculated using the optical parameters measured on small samples in the laboratory. These parameters could show non-homogeneous behavior for larger areas and due to aging processes. For these reasons it is necessary to measure as many optical parameters and eventually N_0 for the full-size device.
In order to investigate all these properties, an intense isotropically distributed electron source of energy between 10 and 1000 MeV/c^2 would be a reasonable probe. The number of detected photons per ring could then provide informations about N_0. Such a source could be realized via elastic scattering, but this is not possible with the SIS facilities that do not provide high energetic electron beams.
Besides that, it is known from previous simulations [Had 94] that the small radius of the rings (about 4 pads on the pad-plane) leads to an overlap of the different photons, such that it is difficult to extract the signal corresponding to a single photon. The calculation in equation (4.4) is valid only for e^+/e^- produced in the target, that travel across the whole gas radiator, while in a normal heavy ion reaction there are many leptons produced by conversion processes in the gas radiator itself, for which the path length is much shorter. A priori it is not possible to distinguish between the signals induced by the leptons coming from the target and those coming from the radiator. Therefore it is not possible to calculate N_0 precisely.
A second possibility is to use a source of VUV photons irradiating the whole detector. The number of detected photons according to the optical parameters measured in the laboratory can be calculated and N_0 can be extracted by the comparison with the experimentally detected photons. Crucial for this experiment is the possibility to get on the detector separated photon hits that can be counted individually. If this is feasible the single photon response of the detector can be extracted as well.
Each photo-electron induces a signal on more than one pad on the photon-detector and hence form a pad cluster. The characterization of the cluster topology is very important to understand the ring properties. If the single photon response can be measured,

it is possible to parameterize the detector response to the e^+/e^- signal and learn about the ring properties.
One may ask, why it is so important to know how a lepton ring looks like?
The answer lies in the fact that the RICH detector is used as on-line trigger for e^+/e^- in order to reduce the amount of data. The on-line ring recognition must be very fast and precise and the algorithm used must be tuned on the ring pattern produced by real leptons. Therefore it is important to know precisely how the ring patterns look like.
In order to study the single photon response of the RICH a dedicated measurement has been carried out [Sch 00] at GSI; the collected data have enabled the extraction of the response of the detector to single photons and the single photon efficiency.
In the following chapter the experiment and the data analysis will be described.

4.1.2 Experimental setup

The VUV photon source was obtained by focusing a low intensity (10^3 particles/s) carbon ($^{12}C^{6+}$) beam of E = 600 $AMeV$ ($\beta = 0.794$) onto a set of polished radiator disks located close to the standard target of the HADES spectrometer (see figure 4.1 and figure 4.2). Since the solid radiators are placed around the beam pipe it was necessary to displace the focused beam to hit them. The carbon ions were counted individually by two in-beam diamond detector placed 40 cm upstream from the RICH detector.
The two radiators chosen were MgF_2 and SiO_2, for which the photon transmission as a function of the wavelength is shown in figure 4.3 [Sch 00]. The MgF_2 shows a good photon transmission for wavelengths between 130 and the visible region. As already shown in figure 2.6, this range corresponds to the whole acceptance for all optical

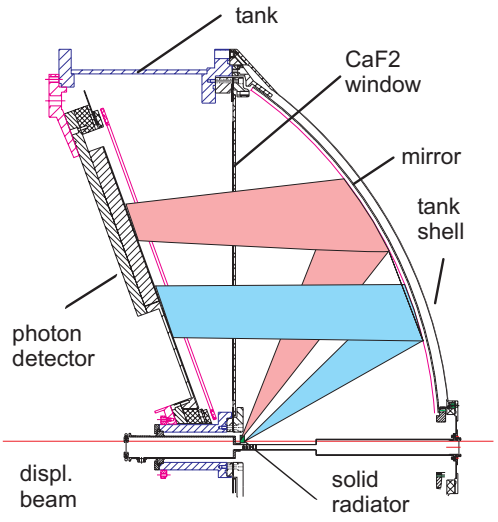

Figure 4.1: Cross section (upper half only) of the HADES RICH. Ions from the displaced beam emit Cherenkov radiation in solid radiators close to the target.

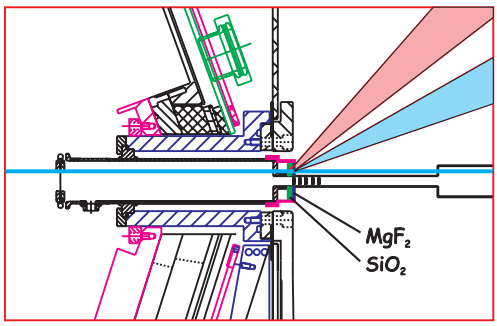

Figure 4.2: Detail of the set-up with the two solid radiatoris around the beam pipe.

components of the RICH detector. This property will allow the determination of the detector response over the whole interesting wavelength range. The transmission of the SiO_2 crystal is limited in the range above 165 nm, but the higher dispersion with respect to the MgF_2 leads to a larger occupied area on the pad-plane for photons produced in the SiO_2. The thickness of the 2 radiators was chosen such that the photon multiplicity per event (about 80 photons per sector) is high enough to get a good signal to background ratio, considering an electronic noise contribution of about 1%, and a low pad occupancy at the same time, to minimize the double photon hits contribution. For a thickness of 5 mm for SiO_2 and 2 mm for MgF_2, an occupancy of one photon each 5×5 pads is expected. In this way it is possible to separate individual photon hits.
Given the refractive indexes of the two materials, the Cherenkov angle of the emitted photons has been calculated using:

$$\cos \Theta_c = \frac{1}{n(\lambda)\beta}, \tag{4.5}$$

where β is the velocity of the incoming carbon ion from the accelerator with $\frac{\Delta\beta}{\beta} < 10^{-4}$. Knowing the angle θ_c the number of emitted photons from the interaction of each ion in the two solid radiators has been calculated using equation (4.2) . Assuming a wavelength of 200 nm the two refractive indexes of MgF_2 and SiO_2 are 1.422 and 1.551 respectively. Substituting $n(\lambda)$ [Opt 93], [Pal85] in equation (4.2) , it has been estimated that for each interaction about 1200 and 3000 photons will be emitted from the MgF_2 and SiO_2 radiators, respectively in the region 150 $nm < \lambda < 210$ nm.
Due to the dispersion, the refractive indexes of the two media depend upon the photon-wavelength. This effect leads to a dependency of the Cherenkov angle on the photon-wavelength and hence to a broadening of the two light cones. Figure 4.1 shows the cross section of the two cones. For the given radiator thickness the resulting occupancy of photon hits on the detector pad-plane has allowed to identify pad clusters from single photons and to determine the photon energy (respectively the wavelength) from the polar angle.
As shown in figure 2.6, the overall efficiency for the larger wave length is limited by

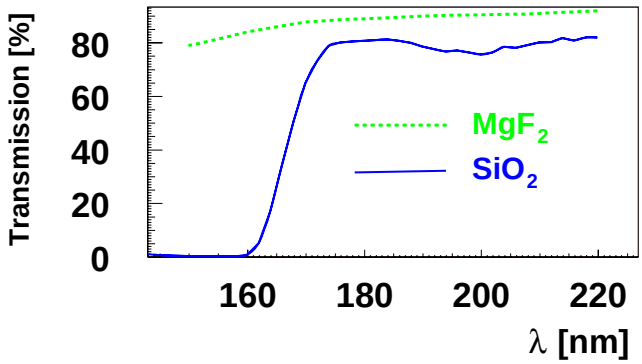

Figure 4.3: Transmission of the two solid radiators.

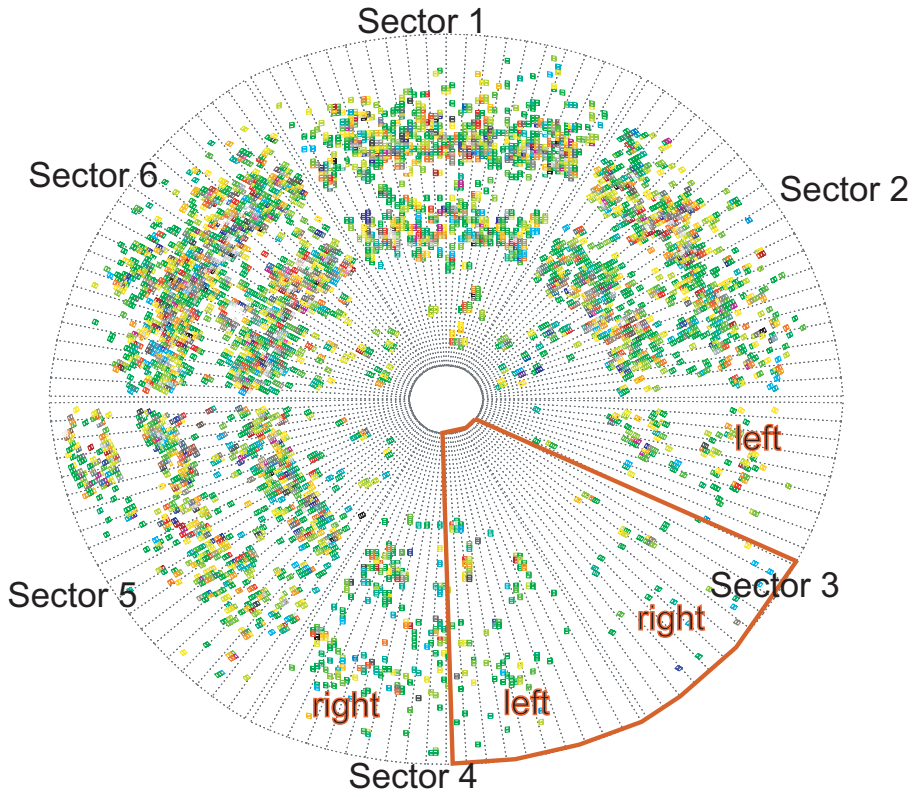

Figure 4.4: 50 accumulated events of the OEM measurement. The photon yield due to the two radiator crystals is visible, the outer ring corresponds to the SiO_2 crystal, the inner ring to the MgF_2.

the quantum efficiency. Since the quantum efficiency behavior is crucial for the higher wavelength, it is very important to investigate this region with high resolution.
The experiment was performed in November 2002 with a beam intensity of about 1000 ions/spill (1 spill $\sim$ 8 sec). The focusing of the beam was achieved using the coincidence of the signal of the start detector, placed 30 cm upstream from the target, and the halo detector, placed 30 cm downstream from the target.

Figure 4.4 shows the pads occupancy for 50 accumulated events. The two rings are due to the photons produced in the two radiators, the outer one corresponds to SiO_2 the inner one to MgF_2.
Figure 4.5 shows the pad occupancy in one of the six sectors for a single events. In the following section the event selection applied to the experimental data is explained.

4.1.3 Event Selection and Cleaning Procedure

The coincidence of start and halo detectors has been used to focus the beam position changing the impact point to cover all the sectors. Due to the beam pipe, given an impact point on the solid radiators, there is at least one sector that is in the shadow, hence only partially hit by photons. Since the beam position is not completely stable,

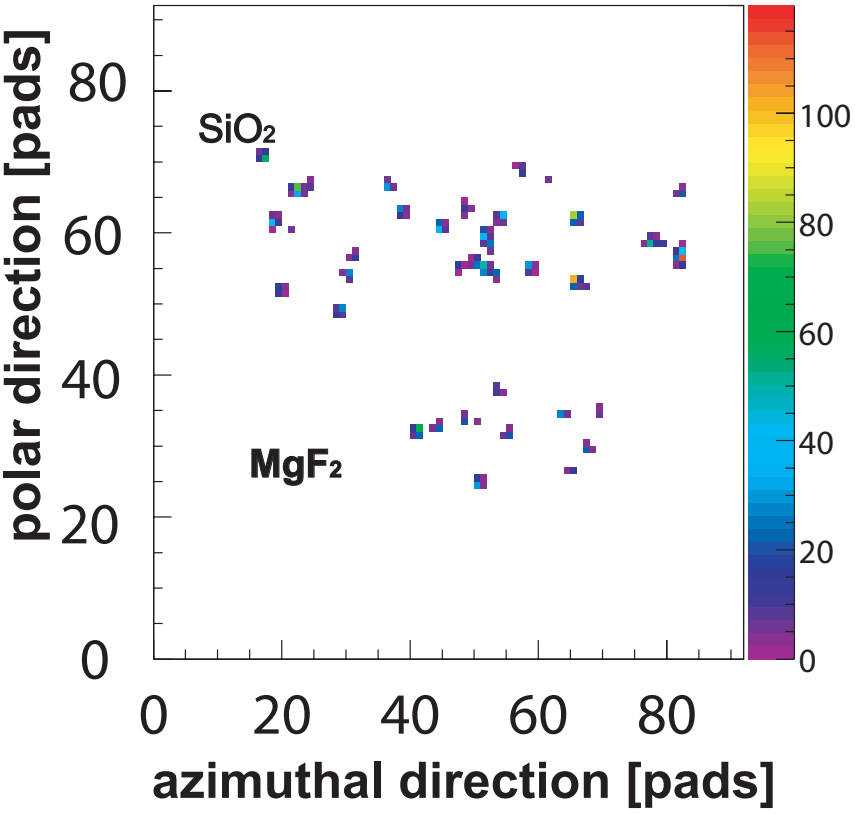

Figure 4.5: Cherenkov ring segments measured in one sector for a single ^{12}C ion impinging on a MgF_2 (inner segment) and a SiO_2 (outer segment). The color code reflects the pad pulse height.

it is necessary to select offline events where the shadow position and extension were constant. This is done by means of cuts on the pad multiplicity for those sectors partially covered by the shadow, that can be seen in figure 4.4. The two shadowed sectors have not been used for the photon efficiency analysis, therefore for each setting only data for four sectors could be analyzed. For the particular setting shown in figure 4.4, a correlation analysis on the multiplicity of fired pads (M) in the different sectors has been done and the following cuts have been obtained:

- $M(Sector\ 3) \geq 20$
- $M(Sector\ 4) \geq 30$
- $M(Sector\ 3, Left) \geq 3 \cdot M(Sector\ 3, Right)$
- $M(Sector\ 4, Right) \geq 3 \cdot M(Sector\ 4, Left)$

A logical AND of these cuts has been applied, whereas the last two inequalities restrict the multiplicity cuts on the external edges of the shadow region, to avoid triggering on events characterized by noise or pile-up.
Figure 4.6 shows the average multiplicity pad distribution on each sector for the experimental data after the event selection has been applied. The active sectors (Nr. 1, 2, 5 and 6) show very similar multiplicity distributions, they range on average between 40 and 120 fired pads per event.
Additional data have been taken with the beam displaced in two different position such to irradiate with photons even sector number 3 and 4. The multiplicity cuts have been applied always on the sectors on the edge of the beam pipe shadow. An additional selection is needed to get rid of the events where the incoming ^{12}C beam has interacted with the start detector or with other materials upstream from the target. These events can be identified since the reaction products that reach the photon-detector induce on the pad-plane clusters that are quite different from those induced by photon hits. An example of such clusters is shown in figure 4.7 and one can see that it is possible to select them by looking at the maximum pulse height, that in case of the fragments reaches values up to 700 ADC channels (to be compared with the maximal photon pulse height of about 200 ADC channels shown in figure 4.5). The events that contain such clusters will be rejected.
The events that pass these selections have been used to study first the single photon response and secondly the single photon efficiency of the RICH detector.

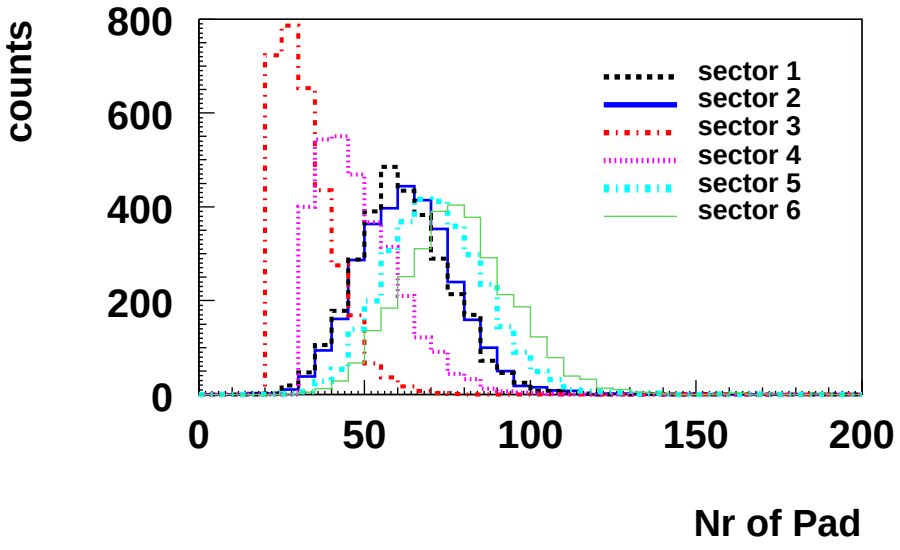

Figure 4.6: Average pad multiplicity distribution for experimental data for the six sectors.

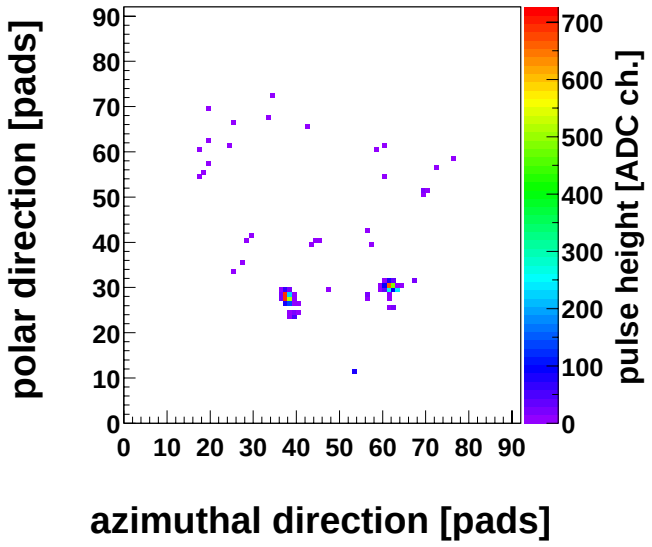

Figure 4.7: Characteristic signature of a direct hit on the detector pad-plane.

The following paragraphs describes the analysis steps that have been followed. The detector response for a single photon has been extracted from the single event experimental data. This response has been parametrized and implemented in the simulation of the RICH detector response. Then a full-scale simulations of the Online Efficiency Measurement experiment has been carried out and results have been obtained that can be directly compared with the experimental data. The parallel analysis of accumulated events for simulated and experimental data allows a detailed analysis of different contributions to estimate to the detector efficiency.

4.2 Single Photon Response of the MWPC

The first step of the analysis consists in extracting o the single photon pulse height distribution from the experimental data. As it can be seen in figure 4.5, the different photon hits lead to the formation of pad clusters on the pad-plane. For low pad cluster densities, it is possible to sum up the pulse height registered by each pad of the cluster and come up with the single photon pulse height. The distribution of the photon pulse height delivers significant informations about the detector performance.

4.2.1 Pulse Height analysis.

In a typical wire chamber operating in proportional modus, the shape of the pulse height distribution of a single photon is expected to obey the Fury law [Piu 03]:

$$P(A) = \frac{1}{A_0} \cdot \exp\left(-\frac{A}{A_0}\right), \tag{4.6}$$

where A and A_0 are the current and the average pulse height. Given A_{thr} the detection threshold of the front end (FE) electronics, one can calculate the single-electron detection efficiency in the following way:

$$\epsilon_{det} = \exp\left(-\frac{A_{thr}}{A_0}\right). \tag{4.7}$$

The measured hits on the detector do not stem only single photons. Indeed, in addition to the signal produced by the avalanche created by the primary photo-electron, secondary electrons can be ejected by feedback-photons, formed by various excitations of the detector gas. For a CH_4 detector gas, photons are emitted predominantly according to three lines at 156, 166 and 193 nm with relative abundances of 30, 57, 13 % [Mor 74].
It is known from previous studies [Arn 88], that the amount of the feedback-photons is proportional to the pulse height A of the primary avalanche according to:

$$N_{feedback-photon} = 7.7 \times 10^{-6} \times A. \tag{4.8}$$

Since the feedback-photons are produced in the avalanche of the primary electrons, it is very likely that they induce a signal on the same pads to which the signal of the primary electron couples. This makes it difficult to separate their contribution from that of a primary photo-electron.
It is anyway possible to select photon hits that have a lower probability of containing feedback contribution to extract the characteristics of the primaries. The clusters visible in figure 4.5 can be classified in three classes:

- class 1 : clusters of one, two or three pads where the pad with maximal charge is in the "middle"of the cluster;
- class 2 : clusters of three pads where the pad with maximal charge is not in the center;
- class 3: clusters of more than three pads.

The assumption that is made is that, since the feedback production is proportional to the pulse height of the primary photon (4.9) and since larger pulse heights generate larger clusters, small clusters have a lower probability to contain the contribution of a feedback-photon.
Figure 4.8 shows the pulse height distribution of the photon hits belonging to the three classes. It can be observed that the slope of the pulse height distribution increases for class **3** in comparison with class **1** indicating the contribution of secondary effects.
Studies carried out by the Alice collaborators [TDR 99] show that only a small fraction

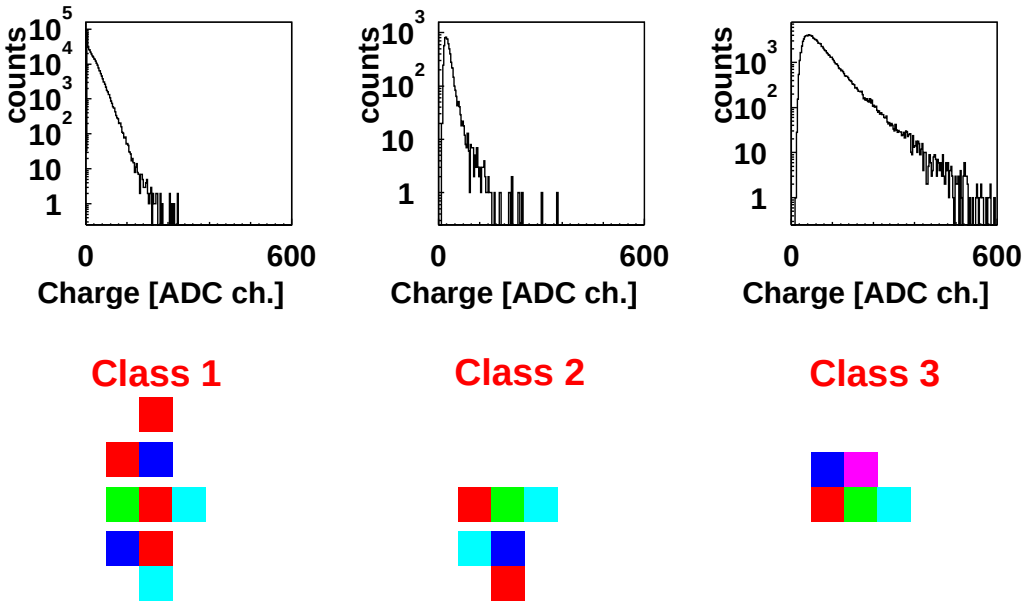

Figure 4.8: Definition of the cluster classes.

of class **1** clusters is generated by more than one photo-electron. The contamination of the class **1** clusters has been investigated via a Monte Carlo program and it has been found that 9% of class **1** clusters contain contribution of a feedback-photon and 8.4% are generated by two overlapping primary photons. The low contamination entitles us to extract the pulse height characteristics of the primary photons using only class **1** clusters.

4.2.2 Single Photon Pulse Height.

If the class **1** clusters do not contain any significant contamination by the feed-back photons, the pulse height distribution of the photon candidate, reconstructed summing up the pulse height of each pad belonging to the cluster, should follow equation (4.6) . The inverse slope of the pulse height A_0 distribution for a single photon (see (4.6)) is a measure of the detector gain. Data have been collected for nine different values of the MWPC anode voltage setting between the cathodic pad-plane and the anodic wires. Hence it is possible to analyze the dependency of the gain upon the anode voltage.
Figure 4.9 shows the pulse height distribution for photon hits of class **1** for four different values of the anode voltage. Together with the experimental distribution two fits are shown, the full-line represents an exponential fit and the dashed line a fit done using a Polya Function [Alk 70].

The used Polya function is:

$$P(A) = \frac{1+\theta}{A_0 \cdot \Gamma(1+\theta)} \cdot \left(\frac{A}{A_0}(1+\theta)^{\theta}\right) \cdot \exp - \left(\frac{A}{A_0}(1+\theta)\right) \tag{4.9}$$

whereas A is the pulse height and the parameter θ accounts for the deviation from the pure exponential curve (see (4.6)).
The departure of the pulse height distribution from the pure exponential curve for increasing anode voltages indicates that selecting the class **1** clusters a bias on the total pulse height of the clusters has been introduced. Indeed the signal induced on the pad-plane from a single photon distributes eventually on more than one pad and this coupling mechanism can lead to clusters with more than 3 pads even if they are generated from a single primary photon. This effect sets at an anode voltage of 2400 Volt. For lower voltages the pulse height distribution can be fitted with a pure exponential function. As shown in figure 4.9, starting from 2450 Volt the exponential function reproduces only the low pulse height range (up to 50 ADC channels); therefore, the Polya function has been used as a generalization of the exponential function to fit the whole range and the results of this fit have been compared with the slope of the exponential fit applied between 10 and 50 ADC channels.
The results of the two fits applied to the pulse height distributions of the class **1** clusters for different anode voltages are collected in table 4.1. The so obtained values of A_0 are in reasonable agreement between each other. The increase of the parameter θ with the rising anode voltage shows that the bias on the pulse height introduced by the definition of class **1** plays a more significant role at higher anode voltage.
The same analysis can be applied to the pulse height distribution obtained for all clusters. Higher values of A_0 are expected for all the clusters due to the contribution of feedback and secondary photons.
Via a Monte Carlo calculation, it has been estimated that 12% of all clusters contain the contribution of at least one feedback-photon and 16% are generated from two overlapping primary photons. If the photon pulse height is sufficiently high it is possible that more than 1 feedback-photon is produced. This will lead to very big clusters with up to 15 pads.
Additionally, a finite element calculation has been carried on [Zei 03], assuming a realistic field geometry and tabulated gas properties. This has been used to compute the expected values of A_0 as a function of the anode voltage for the HADES RICH specifications (see A.1 for details).
The results are summarized in figure 4.10, where the values of A_0 obtained from the analysis of the class **1** clusters, all clusters and from the calculation are shown as a

HV [Volt]	2150	2250	2350	2400	2450	2475	2500	2525
A_0^{Exp} [ADC ch.]	3.06	6.2	12	18	23	26	29.5	33
A_0^{Polya} [ADC ch.]	2.97	6.6	13.7	17	24	26	29	32
Θ^{Polya}	0.03	0.12	0.32	0.65	0.77	0.82	0.85	0.95

Table 4.1: Results of the fit of the experimental pulse height distribution of class 1 clusters, obtained using a pure exponential and a Polya function.

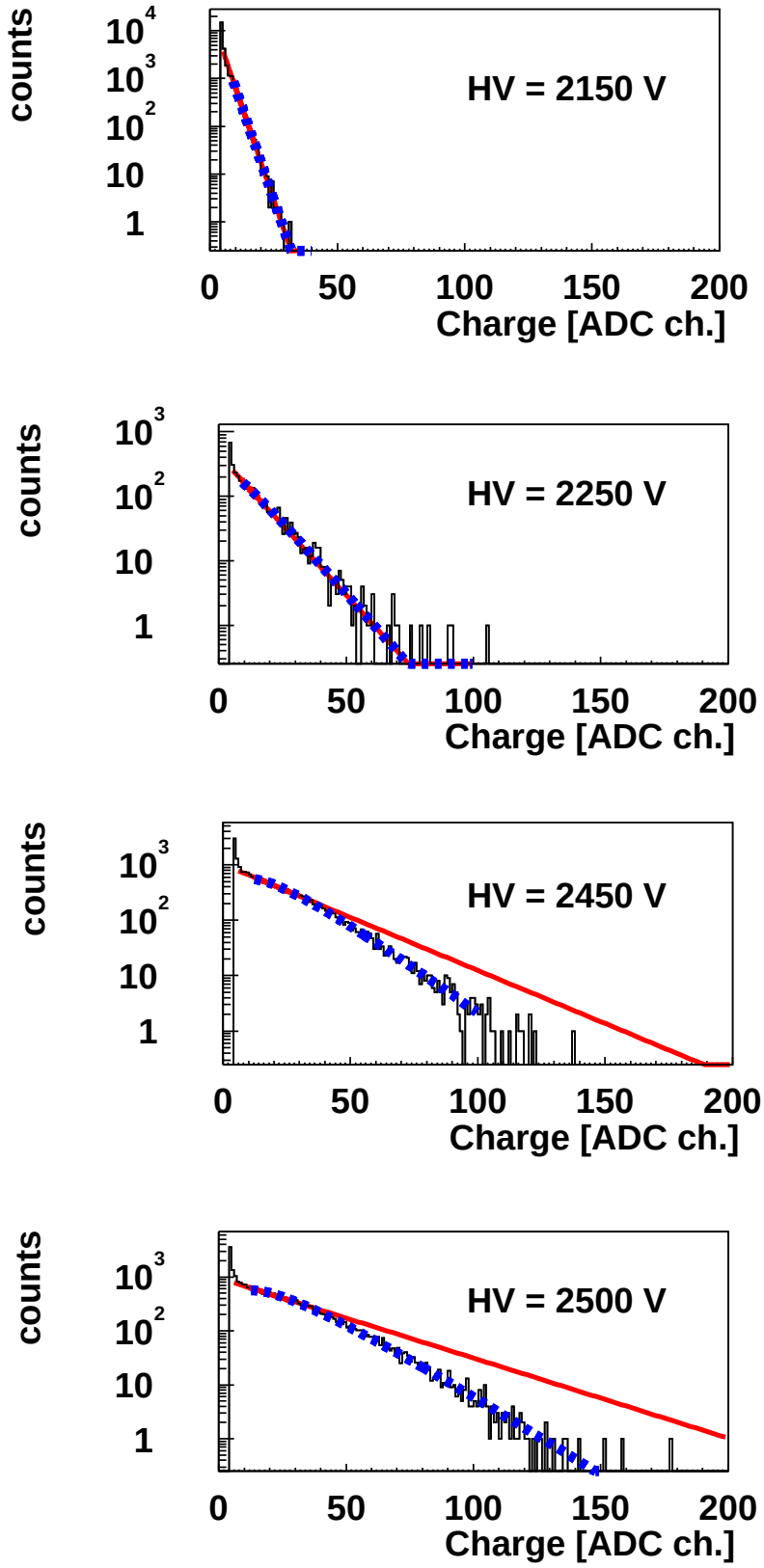

Figure 4.9: Pulse height distribution for the clusters of class **1** for sector number six.

function of the anode voltage respectively. The curve obtained from the calculation is very close to an exponential function and it is fixed on data points obtained from the class **1** analysis for the lowest anode voltage, since the absolute values in the calculations overestimate the measured ones about 50%. This data point should correspond exactly to the single photon result, since at these low voltages the feedback production has not set on yet.
To explain this discrepancy of 50% one has to take into account that the total photon pulse height collected by the electronic corresponds to 75% of the initial charge deposited on the anodic wires [Ger 96]. That means that the expected gain of the MWPC is 25% higher than the values extrapolated from the data. There is still a 25% difference between the absolute values of the calculated gain compared to the values extracted from the data, an possible explanation is given in A.1.
The values obtained from the class **1** clusters underestimate the calculation and the difference gets bigger with increasing anode voltage. This has been again interpreted as an effect due to cut-off introduces by the definition of the class **1** clusters. The difference between the calculation and the results from the analysis of all clusters should be due to the feedback contribution only. The double hit probability is not correlated with the pulse height of the primary photon.
The parameter A_0 at a given anode voltage is evaluated by extrapolating the full squared data points in figure 4.10 up to the theoretical curve. This way, an average photon pulse height A_0 of about 28 ADC channels has been obtained at the operating voltage of 2450 Volt. Given the relation 1 ADC channel = 1730 e^-, A_0 corresponds to 4.8×10^4 e^-. This value is not constant for all six sectors but varies from 4.5×10^4 e^- to 5.1×10^4 e^- and represents the precise geometrical constraints that have been

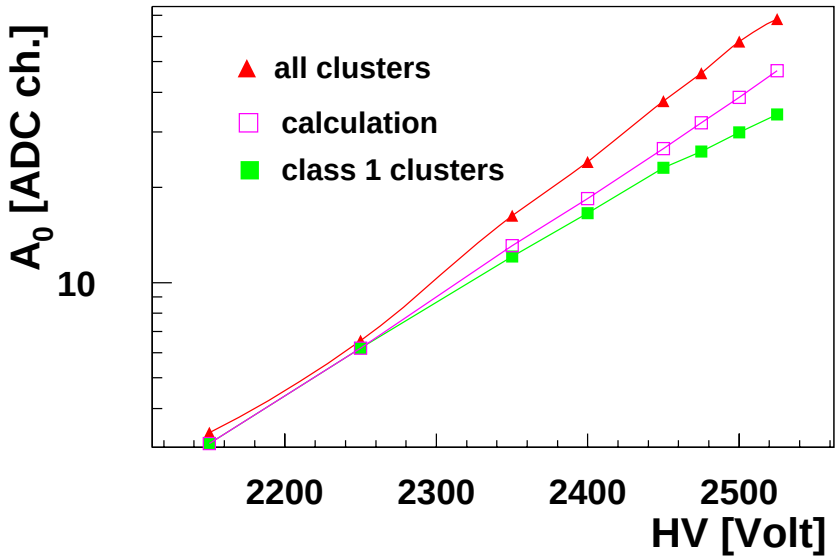

Figure 4.10: Average pulse height of single photons as a function of the anode voltage.

achieved [Kas 00].
Using equation (4.7) and assuming an average threshold of 2 ADC channels for the FE, an average a photon electron detection efficiency of about 93% has been calculated. This analysis has allowed to determine the pulse height distribution of a single photon for a given anode voltage. The open point is still how this pulse height is distributed on the pad-plane forming the different clusters. The mechanism of this coupling is addressed in the next paragraph, where the parameterization of the detector response to a single photon is completed.

4.2.3 Parameterization of the detector response.

In figure 4.5 the clusters of fired pads on the RICH pad-plane in one event are shown. The single photon hits are visible and one can see that the number of pads that compose each cluster varies in most of the cases from 1 to 9 pads.
After the pulse height distribution of a single photon has been investigated, the mechanism that leads to the formation of pad clusters via the action of a single photon has been studied too.
First it has been determined how the photon signal is distributed on the pad-plane, hence how the cluster distribution has come out.
Figure 4.11 shows a schematic view of the 3×3 pad pattern on which the photon charge can be distributed. The two vertical lines represent the anodic wires stretched in front of each pad and the cross the impact position of the photon. Most of the pulse height is induced on the central pad (here pad nr. 4) but some fraction of this charge is coupled to the neighboring pads, as represented in figure 4.11 by the arrows.
The pulse height induced on the neighbors has been expressed as a fraction of the charge induced on the central pad and a parameterization has been found, able to reproduce the experimental values. This parameterization is a function of the total pulse height of the photon, the hit wire and the impact position x of the photon hit along the wire. In order to evaluate the correct coupling parameters for the different neighbors, first only class **1** clusters have been analyzed, since the coupling of a single photon is the aim of the analysis. Figure 4.12 shows the experimental pulse height distribution on the central pad (**4**) and the charge ratio on the right (**5**) and upper (**7**) neighbors. The distribution looks the same for the left and the lower neighbors respectively. The charge ratio for the corner pads shown in Figure 4.12 is zero because the class **1** does not include clusters with 4 pads. This case has been analyzed separately and results are shown later on.
The charge ratio on the upper and lower neighbors (pads **1** and **7** in figure 4.11) depends on the position x of the photon impact along the wire. The experimental distribution $\frac{Q_7}{Q_4}$ (see figure 4.12) has been normalized to **1** and the probability density function for a certain charge to be deposited on pad **7** has been obtained. This probability distribution has been called $P(\frac{Q_7}{Q_4})$ (see figure 4.13). The extraction probability of the photo-electron has been assumed to be independent on the x-coordinate along the wire 4.13.
Assuming a monotone behavior the position x is related to the charge distribution

probability $P(q)$ with $q = \frac{Q_7}{Q_4}$, through the expression:

$$\int_0^{x_1} P(x)dx = \int_0^{q_1} P(q)dq, \tag{4.10}$$

$$x_1 = \int_0^{q_1} P(q)dq = F(q_1) - F(0) \tag{4.11}$$

If a suitable function $F(q_1)$ can be found, the deposited charge as a function of the impact position x can be calculated.

$$q_1 = F^{-1}(x_1) + const. \tag{4.12}$$

Figure 4.14 shows the $\frac{Q_7}{Q_4}$ distribution normalized to 1. This probability density function can be partially fitted with the function shown in the figure 4.14. Integrating and inverting this function using (4.11) the solution has been obtained

$$\frac{Q_7}{Q_4} = F^{-1}(x) + const, \frac{Q_1}{Q_4} = F^{-1}(1-x) + const. \tag{4.13}$$

Figure 4.15 shows the correlation between the charge ratios $\frac{Q_1}{Q_4}$ and $\frac{Q_7}{Q_4}$. Both variables show an offset (G) that can not be explained via threshold effects, since the effect extends all over the pulse height range. This gap has been interpreted as a negative capacitive coupling between neighboring pads.
In order to take this into account a boundary condition has been introduced: $q_1(K) = 0$ to determine the constant in the equation (4.12) . Given the offset G:

$$q_1(0) = -G, \tag{4.14}$$

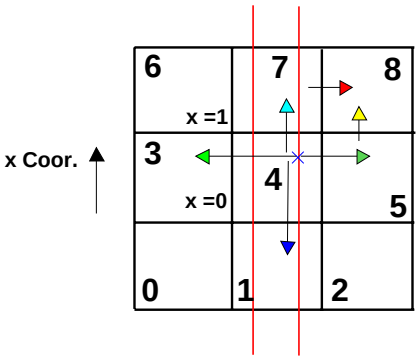

Figure 4.11: Schematic view of the coupling pattern of one photon on a 3×3 pad pattern.

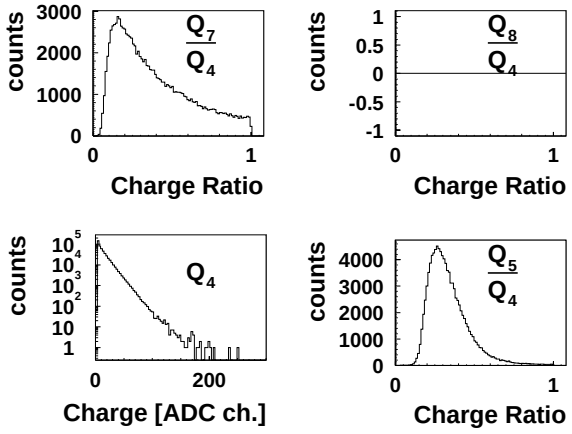

Figure 4.12: Experimental charge distribution for class **1** clusters. $\frac{Q_7}{Q_4}$ and $\frac{Q_5}{Q_4}$ are the ratios of the charge induced on the upper and right pads respectively divided by the charge induced on the central pad.

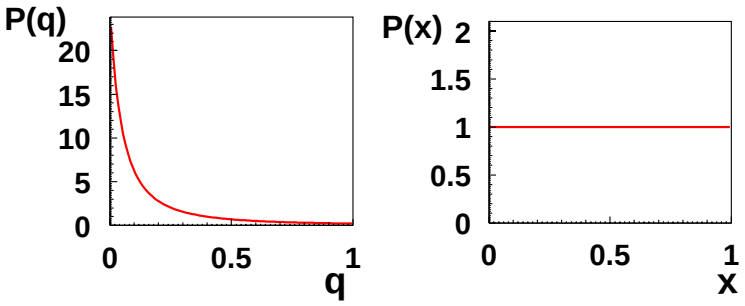

Figure 4.13: Probability density functions for the pulse height ratio q and the impact position x

and applying this condition together with the boundary condition:

$$q_1(1) = 1, \tag{4.15}$$

the solution is obtained:

$$q_1(x) = \frac{Q_7}{Q_4}(x) = \frac{K + \frac{a}{b}}{1 - (K + \frac{a}{b})a^2 \cdot I \cdot x} - \frac{a}{b}, \tag{4.16}$$

where:

- K = -0.03 is the negative capacitive constant,
- $I = \int_K^1 P(q)dq$,

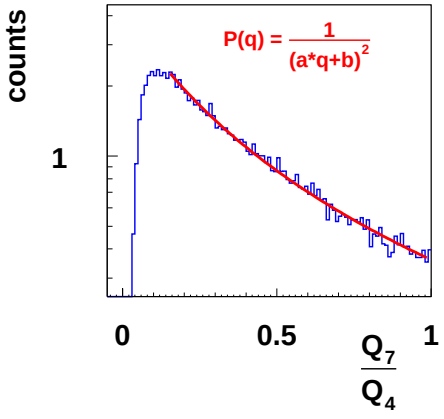

Figure 4.14: Fit of the experimental distribution of the charge ratio $\frac{Q_7}{Q_4}$.

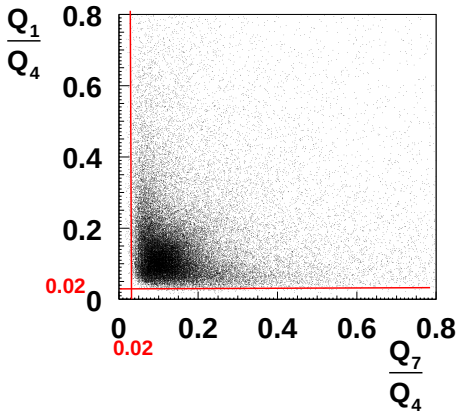

Figure 4.15: $\frac{Q_7}{Q_4}$ versus $\frac{Q_1}{Q_4}$, the figure shows a gap, that has been interpreted as a negative capacitive coupling between the neighboring pads.

- x the impact position,
- a and b the parameters for the fit of the probability density function (see figure 4.14),
- $\frac{Q_1}{Q_4}(x) = \frac{Q_7}{Q_4}(1-x)$.

The solution (4.16) is displayed in figure 4.16. The variable x is expressed in pad units. The negative values that the charge ratio can assume represent the capacitive coupling; this contribution can not be seen from the electronics, sensible only to positive charges. As described above this has been deduced through the boundary condition.
In order to parameterize the pulse height induced on the side pads (**3** and **5** in figure 4.11) it has to be taken into account that the charge from the photo-electron avalanche will be collected only on one of the two wires stretched in front of each pad. If the impact position indicated in figure 4.11 with the cross is considered, some charge will be coupled on the right pad (**5**) and no charge will be coupled on the left pad (**3**). Hence the experimental distribution has been fitted with a Landau function (see figure 4.12 right bottom) and the average ratio and sigma have been determined. It was found: $\frac{Q_5}{Q_4} \simeq 0.19$ and $\sigma = 0.02$. The same parameterization is valid for the left pad. The distance between the right wire and the edge of the left pad is about 0.75 *pad unit* and as the blue dashed line visualizes in figure 4.16 this position corresponds exactly to a coupling of 0.19. This confirms the results obtained by the position dependent parameterization.
The investigation of the coupling on the corner pads (**0**, **2**, **6** and **8** in figure 4.11)

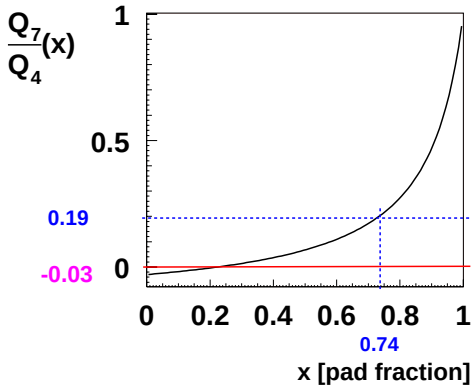

Figure 4.16: Analytical function that describes the dependency of the charge ratio $\frac{Q_7}{Q_4}$ upon the impact position x.

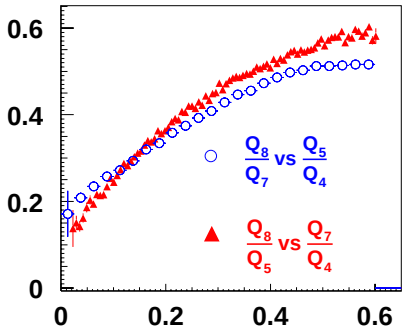

Figure 4.17: $\frac{Q_8}{Q_7}$ versus $\frac{Q_5}{Q_4}$ and $\frac{Q_8}{Q_5}$ versus $\frac{Q_7}{Q_4}$. The profile distribution show that the dependence between the coupling to the corner and the product of the coupling to the side with the coupling on the upper and lower pads can be approximated with a straight line.

requires the usage of larger clusters too. The hypothesis made is that the coupling

strength from the central pad to the upper one is directly proportional to the coupling from the right pad to the corner pad, the same in the horizontal direction. The following formulas clarifies the assumption:

$$\frac{Q_8}{Q_7} = d \cdot \frac{Q_5}{Q_4}, \quad \frac{Q_8}{Q_5} = e \cdot \frac{Q_7}{Q_4}. \tag{4.17}$$

The combination of both informations leads to:

$$\frac{Q_8}{Q_5} = \frac{d}{e}\frac{Q_5}{Q_4} \cdot \frac{Q_7}{Q_4} \tag{4.18}$$

Figure 4.17 shows that the hypothesis of linearity assumed in (4.17) does not reproduce the reality precisely, this is due to electronics threshold effects showing up at small couplings. Nevertheless a linear fit of both experimental distributions shown in figure 4.17 has been performed and a factor of $\frac{d}{e} = 1.37$ has been obtained. The deviation from linearity visible in figure 4.17 does not influence the quality of the parameterization, that is in very good agreement with the experimental data (see section 4.3).

During the analysis it has been found out that the horizontal position of the strained wires is not constant for all six sectors. This has no influence on the charge induced on the upper and lower pad, since this depends only upon the vertical coordinate, but it changes the charge induced on the side pads shifting the mean value of the Landau distribution. Figure 4.18 shows the difference between the charge induced on the right (**5**) and left (**3**) pad for the six sectors. The mean value of the charge ratio distribution $\frac{Q_3}{Q_4}$ is lower than the mean value of the distribution $\frac{Q_5}{Q_4}$ for four of the six sectors and the yield is higher. This can be explained with a shift to the left of the wires with respect of the ideal position. Since the most probable value of the Landau distribution is related to the impact position of the photon on the pad (see figure 4.16), it is possible to determine exactly the shift of the wires. This shift has a maximum value of 0.6 mm for sector six.

The error in the position has been taken into account for each sector separately and the simulation corrected for it.

4.3 HGeant Simulation

A version of GEANT adapted for the HADES spectrometer (HGeant) has been used to process the simulation of the OEM experiment. The Monte Carlo program contains a realistic description of the RICH detector, including all materials (see figure 4.19). A ^{12}C beam at 600 $AMeV$ was shot on the two cylindric solid radiators placed around the beam pipe, as described in 4.1.2. The position of the ion beam was chosen such to reproduce the shadow observed in the experimental data. The Cherenkov photons emitted from the MgF_2 and SiO_2 radiators have been tracked inside the detector and propagated according to the optical properties of all the detector components. Figure 2.6 shows the optical parameters of all the detector components as a function of the photon wavelength. These curves have been measured in the laboratory on small samples and they are used in HGeant to parameterize the photo-transmission of each

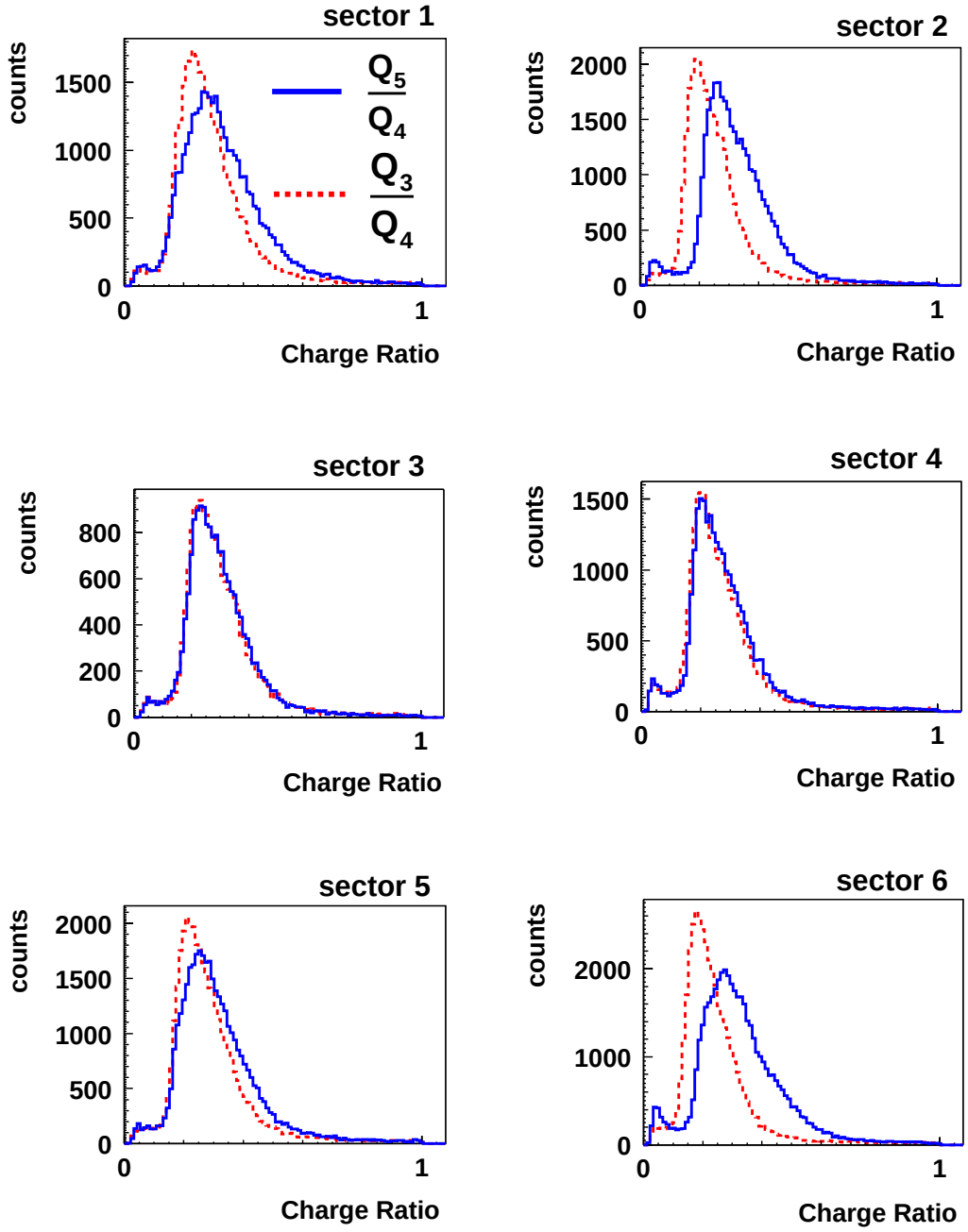

Figure 4.18: The difference between the charge distribution on the left ($\frac{Q_3}{Q_4}$) and on the right neighbor ($\frac{Q_5}{Q_4}$) for the six sectors. The difference is due to a shift of the wires with respect to the ideal position.

component. The HGeant calculation delivers as output the energy of the photon hits that on the photon detector and their position on the pad-plane.
The next analysis step consists of the digitization of the detector response for each the photon hit. This is done using the model described in paragraph 4.2.3.

The parameterization explained so far in 4.2.3, has been implemented in the simulation package of the RICH detector in order to reproduce the experimental single photon response. This program can be applied to the output of a GEANT-based simulation code of the full HADES spectrometer.
Additionally the feedback contribution has been taken into account following [Mor 74] and equation (4.9) .
Another crucial point in the description of the detector response is the understanding of the electronic noise. The electronic noise of the readout chain and front end digitization

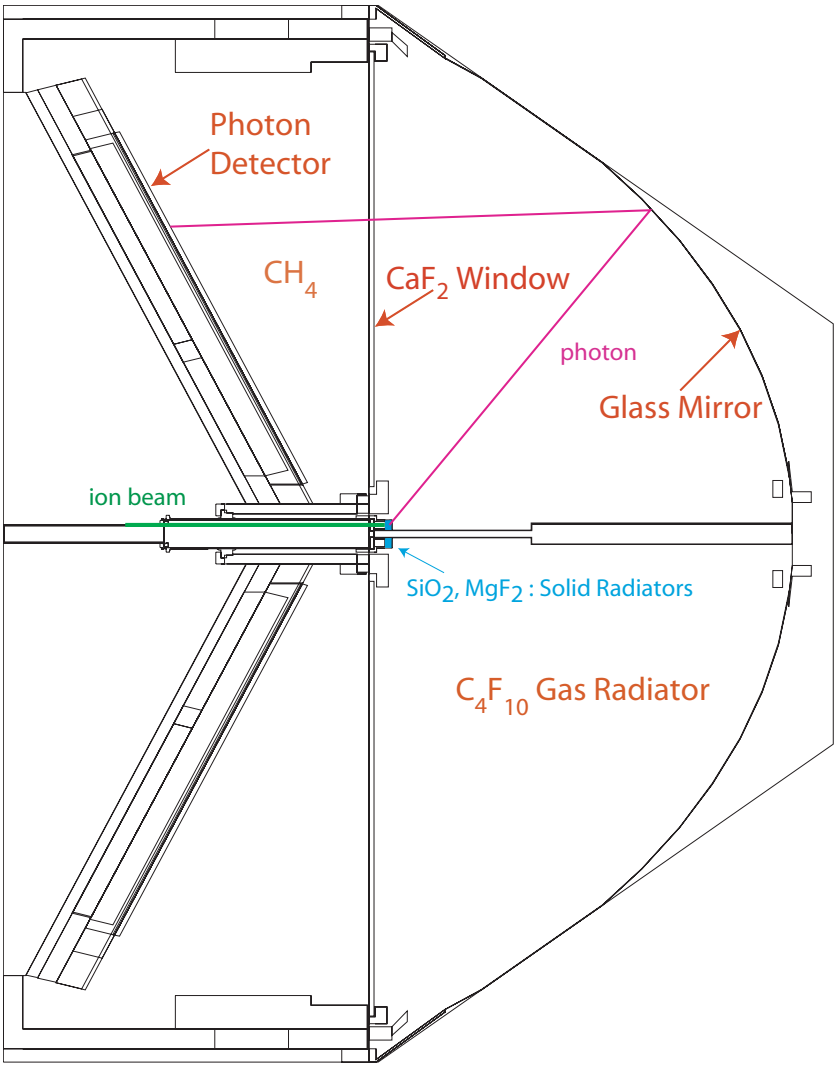

Figure 4.19: RICH detector geometry implemented in GEANT.

[Kas 99] were measured for each of the 28272 pads individually during the data taking with pulsers. It has been assumed that the noise signal on each pad is distributed as a Gauss function, the corresponding mean value and σ of the Gauss distribution are used during the data analysis for the calibration. A cut-off threshold of about $mean + 3\sigma$ has been applied to each pad during the readout time. Later on, during the off-line analysis, the mean value is subtracted from each pad. A similar procedure has been implemented in the simulation. The mean value has been set to 0 for each pad and the values of σ have been read for each pad from the calibration file collected during the pulser runs. The noise has been generated using a Gauss function with mean value 0 and $\sigma = \sigma_{Exp}$, a constant value of 0.5 ADC channel has been added to the noise to reproduce the behavior of the electronics.
To account for changes in the noise situation during data taking with respect to the pulser runs, the possibility of a drift of the mean noise value and of broadening the Gauss distribution has been implemented in the simulation, leaving the cutoff threshold unchanged. The mean value and the width of the Gauss distribution can be tuned for each experiment separately until the simulation reproduces on average the experimental data. Figure 4.20 shows the results achieved for the November 2001 (NOV01) data set. The figure shows a reasonable agreement for the charge distribution due to the electronic noise between experimental and simulated data.
After having generated the electronic noise on each pad in the simulation, the signal coming from the photon hits is propagated and the resulting charge is added to the

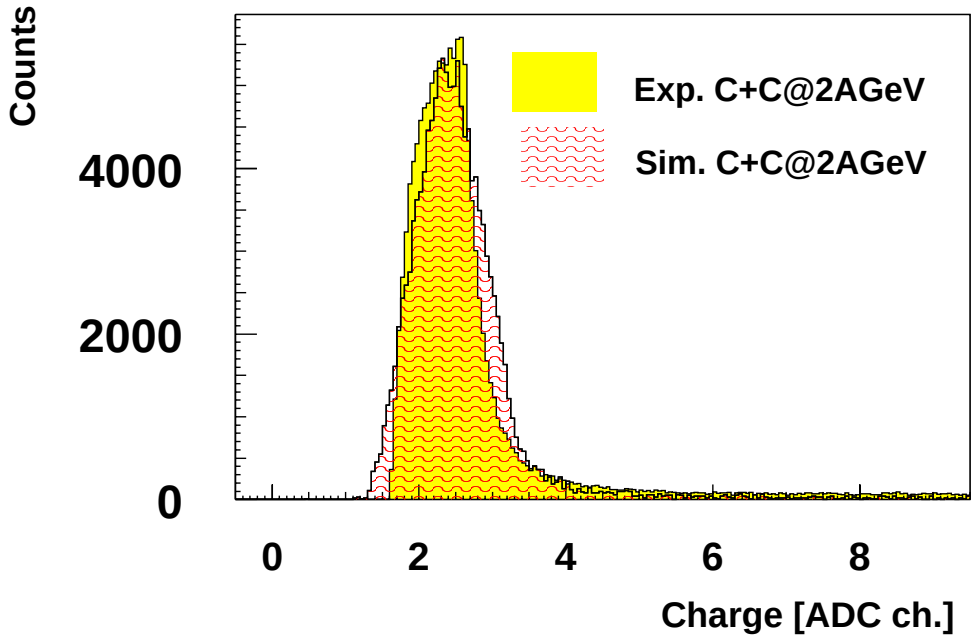

Figure 4.20: Charge distribution due to electronic noise, experimental data from November 2001 data taking and tuned simulations are compared.

hit pads. The same cluster analysis used for the experimental data has been applied to the simulations to allow a direct comparison with the experimental distributions. Figure 4.21 shows the distribution of the pulse height induced in each cluster on the central pad and the ratios $\frac{Q_i}{Q_4}$ only for three of the eight neighbors; experiment and simulation are compared. All the clusters have been used to generate this comparison, hence the result for the corner pads can be checked too. The good agreement of all the distributions shows the validity of the parameterization.
The same comparison has been done using class **1** clusters only and it results in the same good agreement. Overally, the distribution of the single photon pulse height on the pad clusters seems to be reproducible.
Figure 4.22 and figure 4.23 show the comparison between simulation and experiment for the total pulse height and the pad multiplicity distribution for one dedicated sector. The good agreement of the experimental and simulated distribution for the low charge range shows that the electronic noise and the cut-off thresholds have been properly tuned. The agreement for higher charge values shows that the single photon pulse height and the feedback contribution are properly implemented in the simulation. The same comparison can be done separately for class 1 and class 3 clusters and a very good agreement for these distributions has been achieved as well.

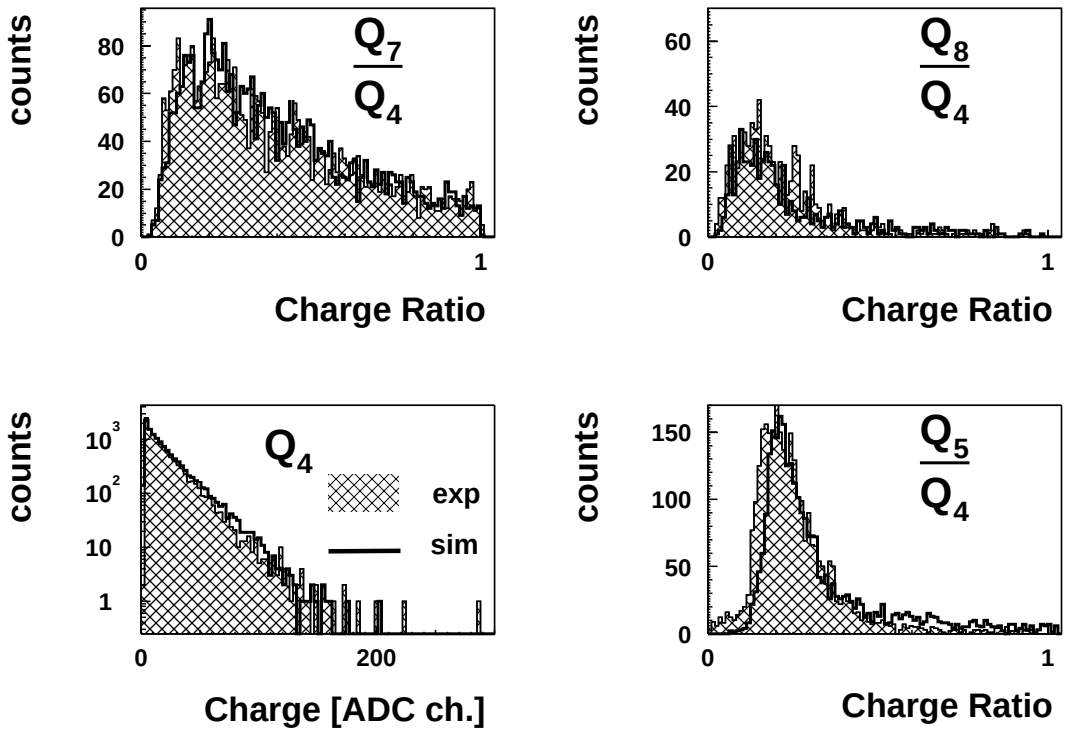

Figure 4.21: Charge distribution on the pad clusters. Charge ratios ($\frac{Q_i}{Q_4}$) with respect to the charge on the central pad (Q_4) are plotted for experimental and simulated data.

The pad distribution reflects the class divisions and the electronic noise contribution (clusters with one pad) and it seems to be properly reproduced by the model.

4.4 Single Photon Efficiency

In order to extract the single photon efficiency of the RICH detector a reference is needed, which is generated by simulations. The accurate description of the single photon signal allows to qualitative rely on the simulation results. Since the Cherenkov photon production is a well known mechanism, the number of produced photons in the experiment can be calculated. The Monte Carlo package HGeant has been used to simulate the OEM experiment and the number of photons have been calculated according to the detector design values.
In the following subsections the analysis of simulated and experimental data will be described in parallel, up to the estimation of the efficiency.

4.4.1 Pad distribution and local maxima selection

The pattern shown in Figure 4.4 for the experimental data has been obtained with the simulation as well. Using the HGeant program it is possible to focus the incoming beam precisely and hence fix the shadow position discussed in 4.1.3. Figure 4.24 shows the pad multiplicity distribution for the six sectors obtained with a beam position that produces a shadow only on sector 3. The simulated multiplicity distributions are not exactly the same between the different sectors. In general, the difference can be due to a varying contribution of the electronic noise and some shadowing due to the displaced light source.
Since the efficiency is assumed to be the same for six sectors, the simulations accounts only for differences in the behavior of the electronic noise for the six sectors, . The difference in the efficiency between the sectors contributes only to the experimental distribution.

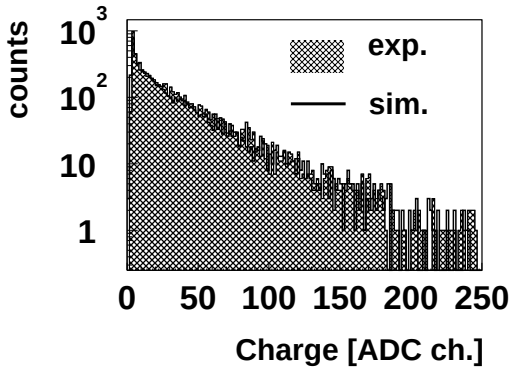

Figure 4.22: Pulse height distribution for all clusters, comparison between experimental and simulated data.

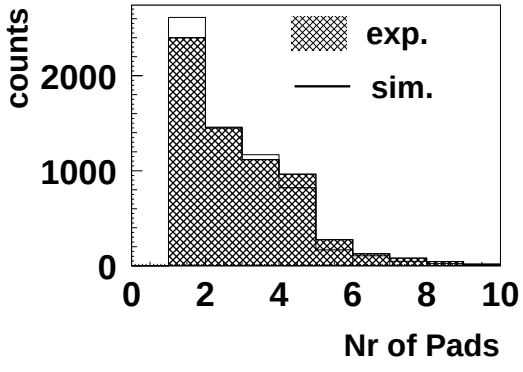

Figure 4.23: Distribution of the number of pads per cluster for all clusters, experimental and simulated data are compared.

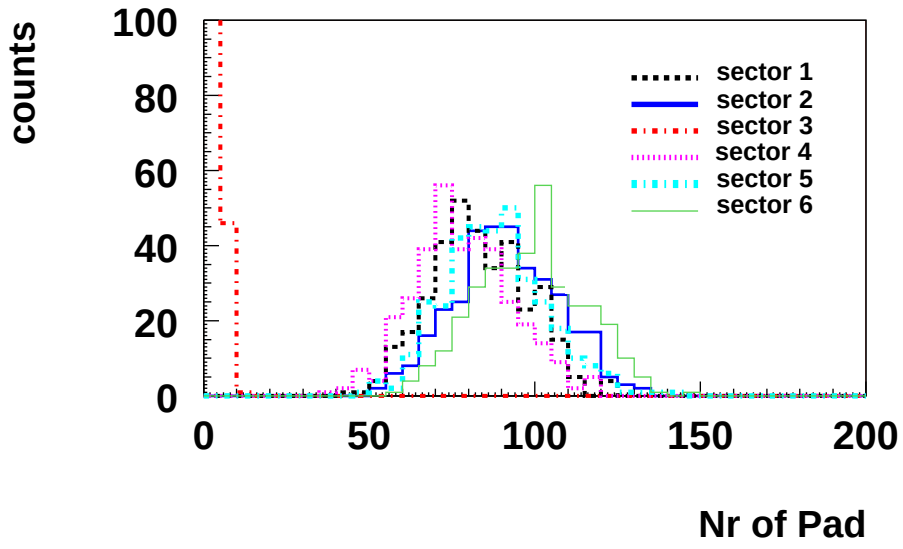

Figure 4.24: Average pad distribution for simulated data for the six sectors.

If Figure 4.24 is compared with Figure 4.6, a higher pad multiplicity for the simulated data can be observed. Assuming that the digitizer reproduces the single photon response of the RICH, this means that in the simulations more photon hits are registered by the detector. This difference has been investigated in details studying the photon hits distribution for the experimental and simulated data.
Simulations have been calculated for two positions of the incoming beam, such to have data at disposal for all the six sectors.

Each cluster of pads can be associated to one or more photons. As it has been already discussed in 4.2.1 small clusters are most probably induced by single photons, the photon position is identified with the position of the pulse height local maximum in the cluster. The local maximum can be selected among four and eight neighbors. If two photon hits overlap in one cluster and are very close to each other, it can happen that the condition of maximal charge is not fulfilled for both produced photo-electron. However, it has been evaluated that only 4% of all the clusters show local maxima that satisfy the condition for four neighbors only and fail for eight. Another possibility is that the two photon hits overlap completely, this effect has already been estimated for small cluster as 8.4%. These double hits for small clusters cannot be recovered in the analysis, they have been considered in the error propagation.
The polar angle distribution of the reconstructed local maxima for simulated and experimental data is plotted, the distributions shown in figure 4.25 is typically obtained for one of the six sectors. The experimental and simulated distributions are normalized to the same number of events. One can see that the integral yield from the simula-

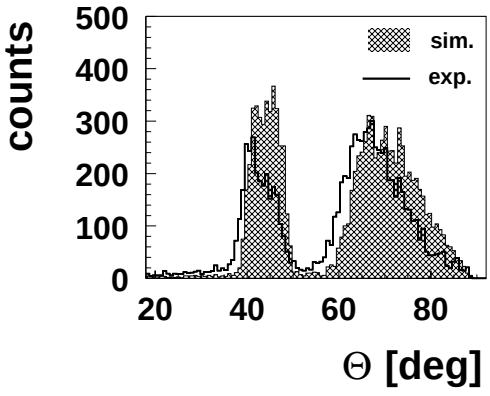

Figure 4.25: Polar angle distribution of the photon hits for 300 accumulated events. Simulated and experimental data are shown for sector 5.

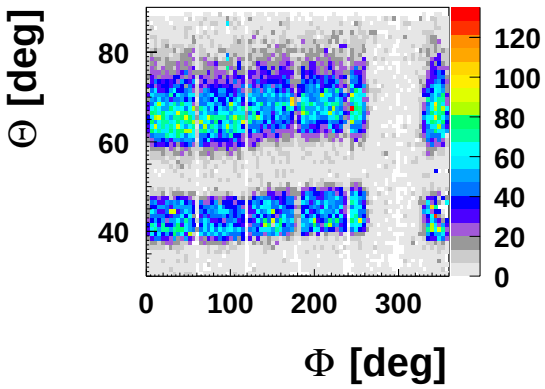

Figure 4.26: Polar angle distribution as a function of the azimuthal angle for the six sectors. The sinusoidal trend of the mean value is visible.

tion exceeds that from the experiment and the distributions are shifted. In order to interprete the experimental yield quantitatively, the polar angle distribution must be in phase with the simulated one, since the photon wavelength has been recovered on the basis of the polar coordinate only from simulations.
Figure 4.26 shows the polar angle distribution as a function of the azimuthal angle for all local maxima for the experimental data. It can be seen that the mean polar angle of the two rings is not constant for the six sectors and that moreover the variation resembles a sinus function. This effect can be explained with the fact that the beam was not parallel to the beam pipe and so the deflection of the beam is the reason for the shift. Since each sector is shifted in a different way the position of the photons in each sector has been corrected shifting the experimental distribution such that the edges of the two rings overlap with the simulated polar angle distributions of the local maxima. Figure 4.27 shows the polar angle distribution of the local maxima for experimental and simulated data after the position correction has been applied for each sector individually. In the first picture on the left, the wavelength boundaries of each ring are marked with an arrow. The left ring corresponds to the MgF_2 radiator and its wavelength range cover the whole VUV range. The right ring corresponds to the SiO_2 radiator and covers only a fraction of the interesting wavelength range but has a better resolution for higher wavelengths.
This region must be studied in detail since the efficiency could be strongly reduced with small variations of the photo-cathode quantum efficiency (see figure 2.6).
The two bumps in figure 4.27 corresponding to the two radiators do not show sharp edges. There are indeed reconstructed local maxima between the two bumps and outside them. This yield is in part due to the electronic noise contribution that is homogeneously distributed over the pad-plane and in the case of the experimental data a fraction of these hits are scattered photons displaced from the two rings. This effect is not included yet in the simulation package. Since the fraction of these scattered photons is very low (3%), no further corrections have been introduced to account for it.

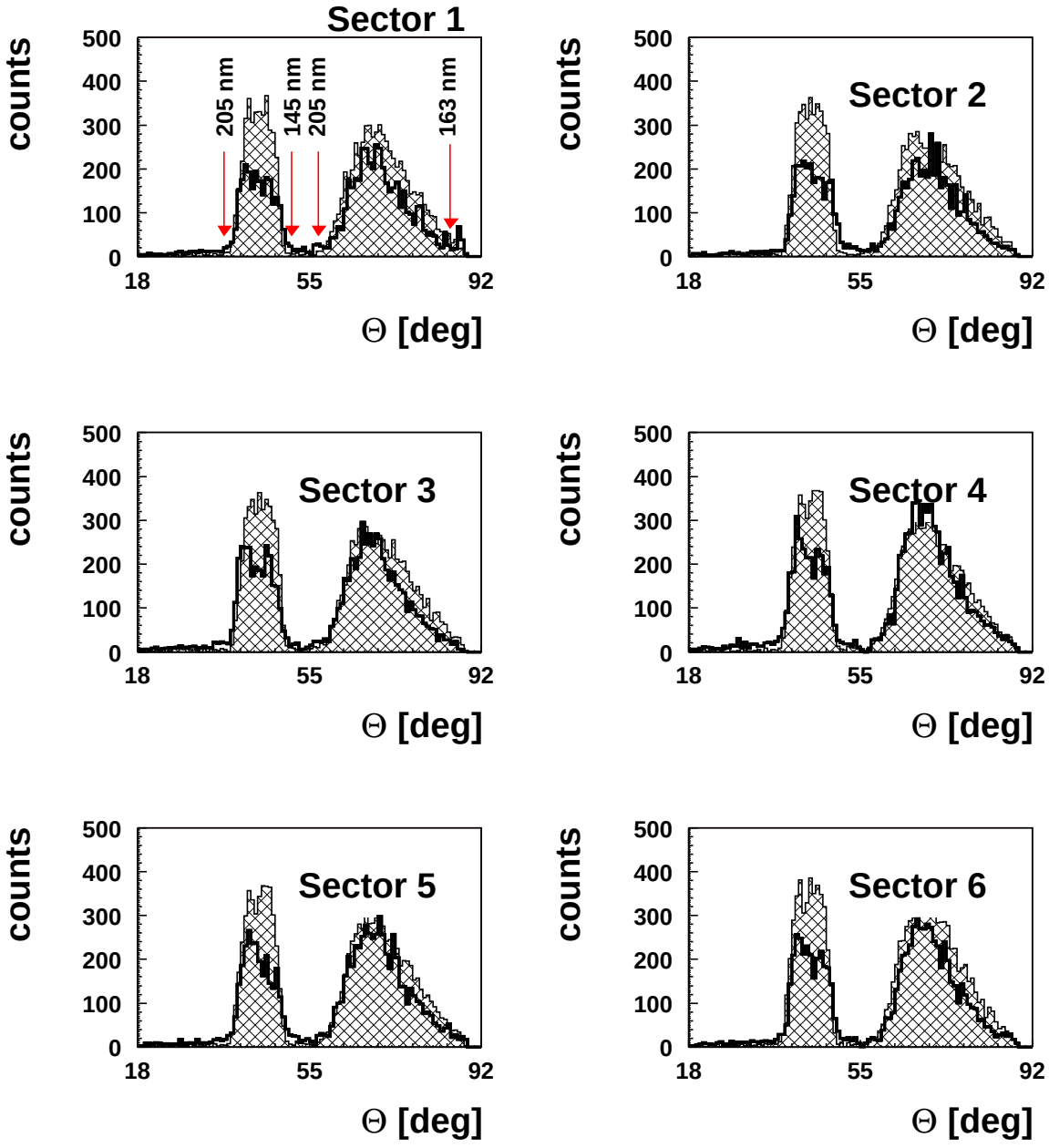

Figure 4.27: Polar angle distribution of the local maxima. For each of the six sectors simulated and experimental data are compared. The bump on the left refers to the MgF_2 radiator, that on the right to SiO_2.

4.4.2 Wavelength Resolved Efficiency

For each ring, the polar angle coordinates of a photon hit is related to the photon wavelength. If the experimental photon yield in each wavelength bin is compared with the expected values from simulations, the realistic efficiency of the detector can be estimated. Figure 4.28 shows the photon wavelength as a function of the polar angle for the two rings. The plot is obtained from simulated data. The dependency between wavelength and polar angle has been extracted fitting a polynomial function to the center of mass distribution of the two rings. The region shown in figure 4.28 below 40 deg. and between 52 and 58 deg. have not been included in the fit. As it can be seen in figure 4.27, these two regions contain only contribution from the electronic noise and from scattered photons. The fit of the simulated data give the relations:

$$\lambda(\theta) = 1.14 \cdot 10^3 - 4.42 \cdot 10 \cdot \theta + 6.12 \cdot 10^{-1} \cdot \theta^2 - 2.47 \cdot 10^{-3} \cdot \theta^3, \tag{4.19}$$

for the MgF_2 radiator and

$$\lambda(\theta) = 1.12 \cdot 10^3 - 3.2 \cdot 10 \cdot \theta + 3.7 \cdot 10^{-1} \cdot \theta^2 - 1.44 \cdot 10^{-3} \cdot \theta^3 \tag{4.20}$$

for the SiO_2 radiator.
The ratio of number of photon identified in the experimental and simulated data as a function of the photon wavelength can be written like:

$$R(\lambda) = \frac{Nr.Phot_{Exp}(\lambda)}{Nr.Phot_{Sim}(\lambda)} \tag{4.21}$$

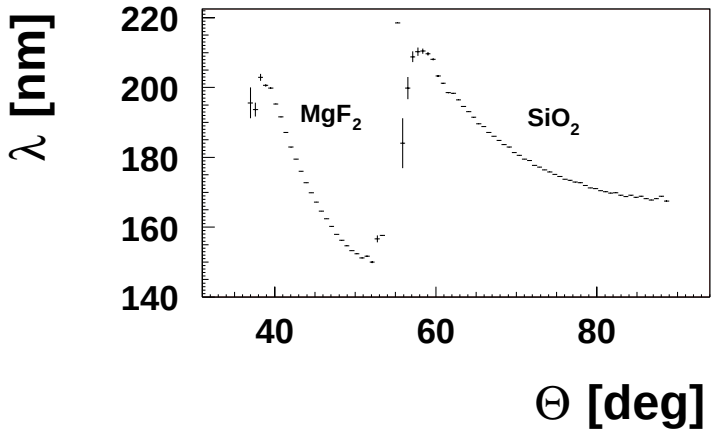

Figure 4.28: Center of mass distribution of the photon wavelength as a function of the polar angle.

Figure 4.29 shows the ratios $R(\lambda)$ as a function of the photon wavelength for the two radiators separately for four sectors. The error shown in the picture was calculated adding quadratically the statistical and systematic contribution. One contribution to the systematic error comes from the uncertainty of the polar angle measurement for the local maxima. This error is assumed to be of the size of half a pad. Since the dimension of the pads is not constant over the polar angle range, the value of the error in degrees is not constant and varies from 0.34° to 0.48°. Since the experimental efficiency has been extracted as a function of the photon wavelength, the systematic error of the polar angle has to be propagated to the wavelength using the equations (4.19) and (4.20) . An additional statistical error comes from the double hit contribution, this correction has already been estimated as an overall value of 8% and stays constant over the whole wavelength range.
The total error shown in figure 4.29 is given by:

$$\Delta R(\lambda) = \sqrt{\Delta^2_{Stat.} + (\frac{\partial R(\lambda)}{\partial \lambda} \cdot \Delta\lambda + \Delta_{DoubleHits})^2}. \tag{4.22}$$

The efficiency of the different sectors can be extracted combining the results from the two radiators in figure 4.29. The empty triangles represent the data extracted from the MgF_2 radiator, the full circles represent the data extracted from the SiO_2 radiator.

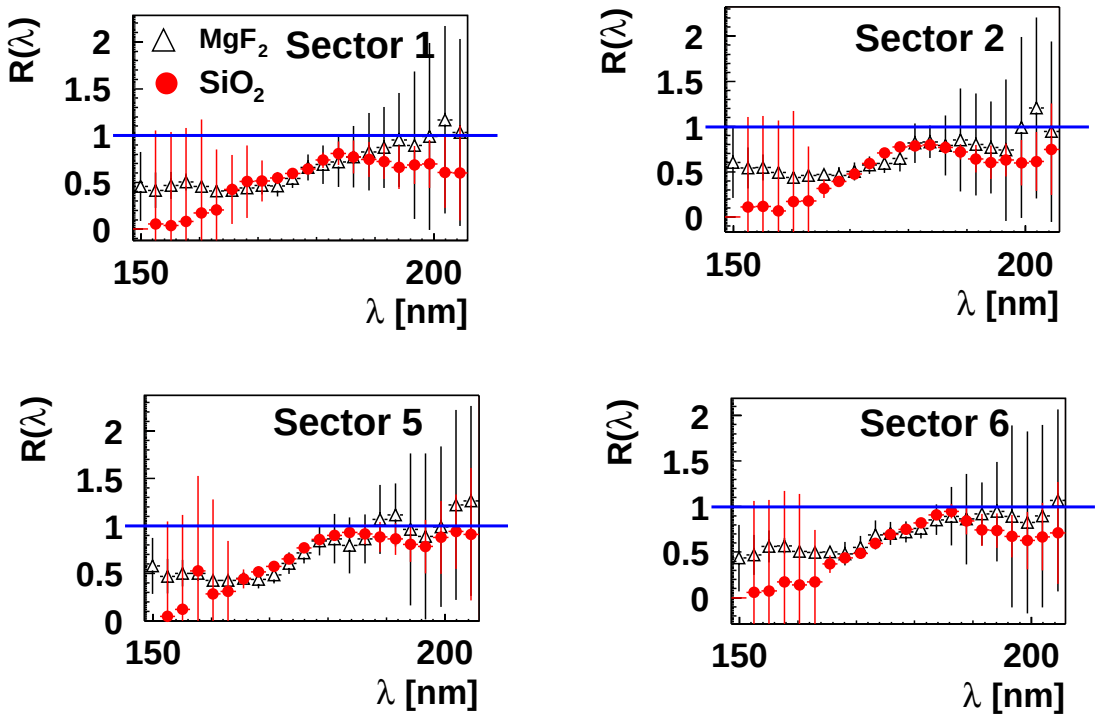

Figure 4.29: Photon yield ratios of the experimental and simulated data as a function of the photon wavelength. The empty triangles correspond to the MgF_2 radiator the full circles to the SiO_2.

The two distributions nicely overlap within the error bars.
In order to calculate an unique correction to the ideal efficiency as a function of the photon wavelength, the following method has been used: for each sector the two distributions shown figure 4.29 have been merged together weighting each point with its error. For each wavelength bin the data points deliver the correction to the unit that one should apply to the simulation in order to get the experimental photon yield.
This means in the region 185 $nm < \lambda < 205$ nm the data points from SiO_2 are more important, while for $\lambda < 165$ nm the MgF_2 results are dominating.
Efficiency losses have been observed only for wavelengths lower than 180 nm has been observed. This effect could be due to impurities in the gas detector or defects in the mirror reflectivity. There are hints that the old provisional mirrors, in the meanwhile replaced, had a lower reflectivity than the one shown in figure 2.6 and used for the simulations. It can however hardly be explained with losses in the quantum efficiency. Indeed, such losses should effect the higher wavelength much more than the lower one.
One of the aims of this investigation was to develop a realistic simulation of the RICH detector. The correction to the photon efficiency as a function of the wavelength has been included in the digitization of the detector response and the simulation of the OEM experiment were repeated to crosscheck that the corrected simulations show the same yield as the experimental data.
The so corrected simulations have delivered photon distributions that are in agreement with the experimental ones within 5%.

4.4.3 Calculation of the Figure of Merit N_0

So far the differences between the single photon efficiency in the experiment and the values predicted by the simulation have been investigated. Figure 4.29 shows this comparison as a function of the wavelength. Another aim of these studies was the determination of the integral efficiency over the whole wavelength range by introducing the figure of merit N_0, which is calculated using the equation (4.3) and is often used to compare the performances of different RICH detectors.
In the case of the OEM experiment, the Cherenkov emission does not happen in the C_4F_{10} radiator but in the two solid radiators placed around the beam pipe. Hence the product of the optical parameters $\epsilon(E_\gamma)$ in equation (4.3) contains their contributions. So the N_0 of the HADES RICH can not be directly deduced from the OEM measurement. However, if one assumes that the measured values of the transmission of the two solid radiators (see figure 4.3) are accurate enough to be considered the same in simulation and experiment, they cancel out in the calculation of $R(\lambda)$. The calculation of the figure of merit for the simulated data is therefore given by:

$$N_0^{Sim} = const. \int_{\lambda_1}^{\lambda_2} \epsilon(\lambda)^{Sim} \frac{d\lambda}{\lambda^2}, \tag{4.23}$$

where the energy E_γ has been expressed in terms of the wavelength λ and $\lambda_1 = 145$ nm, $\lambda_2 = 205$ nm.
Using the ratio of the experimental and simulated yield $R(\lambda)$, the equation (4.23) has

been used to evaluate the experimental figure of merit separately for the two radiators.

$$N_0^{Exp} = const. \int_{\lambda_1}^{\lambda_2} R(\lambda)\epsilon(\lambda)^{Sim}\frac{d\lambda}{\lambda^2} \tag{4.24}$$

where $R(\lambda)$ has been calculated have merging together the ratios obtained for the two radiators (see figure 4.29), weighting each point with its error.
The results from simulation and experimental data for the six sectors are summarized in table 4.2. The so calculated figure of merit reflects a sufficient single photon efficiency, still the reasons for the losses should be investigated. In the following chapter it is explained, how these results affect the single lepton efficiency of the HADES spectrometer.

Sector Nr.	1	2	3	4	5	6
N_0^{Sim} $[cm^{-1}eV^{-1}]$	112	112	112	112	112	112
N_0^{Exp} Tot $[cm^{-1}eV^{-1}]$	69 ± 7	70 ± 7	80± 9	85± 8	80 ± 10	75± 7

Table 4.2: Calculated values for the figure of merit N_0 for all six sector. For comparison the expected values of the simulation are shown as well. The total values of N_0 have been calculated combining the efficiency obtained in the two radiators as explained in the text.

Chapter 5

Single electron efficiency of the RICH detector

The results that have been achieved so far allow us to determine the response of the RICH photon-detector to the single photon signal. The next step consists of the determination of the single electron efficiency of the RICH detector. Since there are no calibrated e^+e^- sources, the determination of the efficiency has to be based on simulations.
In the previous chapter it has been shown how the detector response has been parameterized and how the simulated spectra of the single photons properties are in good agreement with the experimental spectra. Hence, it can be assumed that the so far developed simulations are realistic enough to base the calculation of the single electron efficiency on them.
The calculation of the efficiency has been done using different event generators for the HGeant program. First, a source of electrons produced in target with a flat distribution for the mass and the momentum has been taken. This event generator represents the easiest scenario to be investigated. Secondly, the Ultra relativistic Quantum Molecular Dynamic (UrQMD) model [Ern 98] has been used as event generator (see chapter 3). The Dalitz decays of the π^0 and η mesons are computed already in the event generator, while γ-conversion, production of knock-on and *Delta* electrons happen in the HGeant program. The UrQMD output contains also all the hadrons produced in a given heavy ion reaction. The presence of the hadrons in this analysis enables a more realistic scenario.
All the produced e^+e^- are tracked through the spectrometer and the HGeant output delivers the hit position of the different products.
The answer of the detector is folded with the HGeant output, and a set of data is created in the same format as the experimental data. Rings found in the RICH correspond only partly to electrons or positrons and partly to fake images. Since it is known how many electrons have been produced in the input and in the HGeant program and it is known how many of them have been recognized as a ring, it is possible to calculate the efficiency of the RICH detector. Such an analysis has been carried out for electrons produced in different processes, to investigate possible differences in the efficiency.

As already mentioned, it is of great importance that the simulations describe precisely the experimental data. Since the UrQMD delivers all the known products of a heavy ion collision, the response of the RICH detector to electrons has been studied, comparing results from simulations with UrQMD as generator and experimental data produced in a heavy ion collision.
Figure 5.1 and Figure 5.2 show a typical ring pattern in the UrQMD simulation data

and a ring pattern in the C+C at 2 $AGeV$ experimental data, respectively. The simulation provides the information about the origin of the pattern on the RICH detector, while in the experimental data it is not so easy to know which pattern stems from an electron/positron.

First the properties of the simulated and experimental rings have been compared and

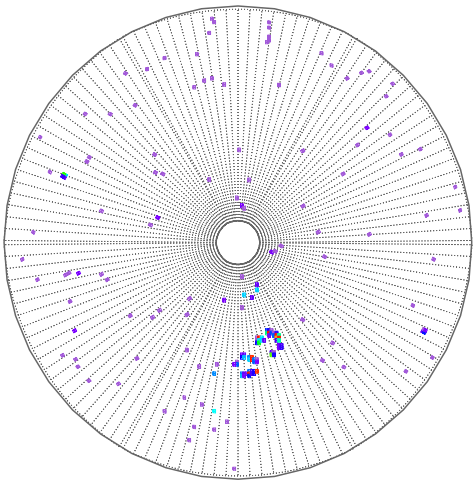

Figure 5.1: Sample ring pattern on the RICH pad-plane taken from simulated data.

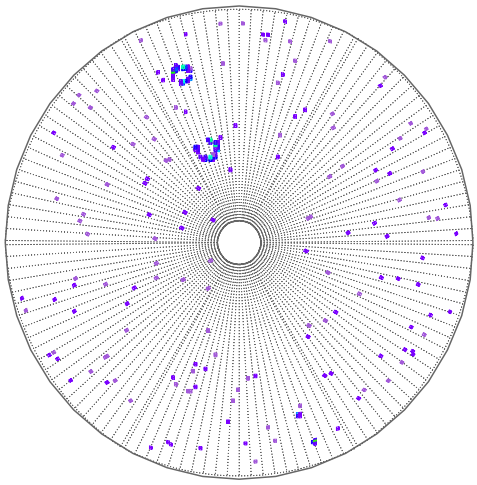

Figure 5.2: Sample ring pattern on the RICH pad-plane taken from experimental data.

secondly a set of cuts has been chosen that allows to select among all electron candidates only the real ones.

In the following sections the ring finder algorithm used on the RICH detector fired pads are shown. The single electron efficiency calculation is explained for different electron sources and finally a comparison of the simulated and experimental rings properties is done.

5.1 Description of the ring finder algorithms

In order to identify rings in the analyzed data, two ring finder algorithms have been used. The goal of these ring recognition algorithms is to identify the position of the rings formed by photoelectrons, that are extracted from the CsI photo-cathode. The ring recognition ability depends not only on the number of fired pads in a ring but also on the regular location of pads along its circumference. If the ring image is not complete it might not be recognized. The following algorithms have been first implemented in the HADES framework by [Wit 02], later on they have been revised and optimized. Before the ring finder algorithms are applied the cleaning and labeling procedures are executed.

5.1.1 Cleaning and Labeling

It has already been pointed put in 4.3, 4.1.3 that there are other effects apart from Cherenkov photon production, that can induce signals on the pad-plane: direct hits and electronic noise. The cleaning procedure to get rid of direct hits is explained in 4.1.3, [Wit 02]. Groups of pads, which contain at least one pad with a very high amplitude (higher than 300 ADC ch.), are removed. Additionally single pads with a small charge (lower than 5 ADC ch.) with a distance from the next fired pad larger than 7 pad units have been removed. The charge threshold corresponds to $3 < \sigma >$, where σ characterizes the Gauss distributed noise signal of each pad. In this way 99.7% of the pads have been removed that are most probably generated by electronic noise.
After the cleaning the labeling is done, which is a process of decomposition of an image into smaller parts.
Since the pad-occupancy is very low (only 1%), the ring finding analysis has been restricted only to those areas of the pad-plane which contain groups of fired pads. Such a procedure reduces the computation time significantly.

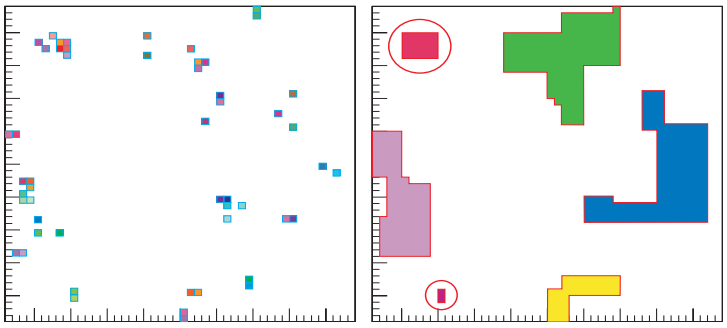

Figure 5.3: The figure on the left shows the hits on a fraction of the pad-plane and the figure on the right shows some of the labels that are calculated from the hits.

Figure 5.3 shows an example of the labeling procedure [Sha 92]. On the left side the pad-plane is shown with the fired pads and on the right side the selected areas (labels) formed with fired pads are visible. Pads have been assigned to the same label if the distance of a fired pad to its next fired neighbor is less that 7 pad units. This minimum distance is chosen in order to limit the size of the labels and at the same time produce labels which are still large enough to contain fragmented ring candidates. If the label is too small to contain a ring (the average ring radius is about 4 pad units) it is removed from the data sample (see the labels inside the circle in Figure 5.3). Hence the labels shown in the right panel of figure 5.3 do not contain only fired pads but they represent the region where the search for a ring candidate is performed.

Two ring finder algorithms have been used which are explained in the following section: one based on a pattern mask (PM) and one that exploits a Hough transform (HT) method. They are used to identify the ring candidates and determine the position of the pad that corresponds to the ring center. Each pad on the pad-plane is mapped to a fixed polar (θ) and azimuthal (ϕ) angle that corresponds to the angular coordinates of the emitted electron. The position delivered by the ring finder algorithms is later on

used to correlate geometrically the found rings with the other detector hits.

5.1.2 Pattern Matrix Algorithm

The Pattern Matrix algorithm is based on the superposition of a pattern image of a ring on the pad-plane. The left side of figure 5.4 shows a 11×11 pads pattern matrix. Each cell contains a weight reflecting the ring image. Positive values form a ring, while negative values correspond to those places where no fired pad is expected. The right side of Figure 5.4 shows a three-dimensional view of the matrix.
This matrix has been constructed using experimental data collected in November 2000. Severals rings have been collected for which positions have been correlated with a hit in the MDC detector. To obtain the matrix, all the rings have been added and the sum has been symmetrized and normalized such that the sum of all weights is zero.
In order to find the ring, the matrix is shifted through all possible labels on the pad-plane. On a given label the matrix is shifted such that each pad fired in the label corresponds once to each matrix slot. For each position a matching of the fired pads on the pad-plane and the matrix has been done as follows: for each fired pad the corresponding weight on the matrix is added to produce a quantity defined as *Pattern Matrix Quality* (PM quality). If the pad cluster on the pad-plane looks like a ring with the foreseen radius, most of the pads get a positive weight in the matrix and the PM quality of the ring will be high.
The matrix is shifted at each step by one pad unit and the PM quality is newly calculated. The maximum PM quality among all the calculated values is computed and the position of the matrix center stored as the center of the ring candidate. If two labels are very close to each other and in both a ring is identified and if the distance between the two is greater than 4 pad units, the ring with the lowest PM quality is rejected.
All the found ring candidates correspond to a PM quality that classifies the ring. This PM quality is a number that varies from 50 to 1500. It is possible to select rings that overcome a certain quality threshold. The value of the threshold must be set such not to throw away too many real rings. In the following, it is shown how this threshold is determined.
The pattern matrix algorithm is very fast, but its accuracy decreases when rings are

-46	-40	-25	1	22	27	22	1	-25	-40	-46
-40	-15	27	50	47	41	47	50	27	-15	-40
-25	27	44	12	-9	-15	-9	12	44	27	-25
1	50	12	-24	-33	-35	-33	-24	12	50	1
22	47	-9	-33	-36	-36	-36	-33	-9	47	22
27	41	-15	-35	-36	-36	-36	-35	-15	41	27
22	47	-9	-33	-36	-36	-36	-33	-9	47	22
1	50	12	-24	-33	-35	-33	-24	12	50	1
-25	27	44	12	-9	-15	-9	12	44	27	-25
-40	-15	27	50	47	41	47	50	27	-15	-40
-46	-40	-25	1	22	27	22	1	-25	-40	-46

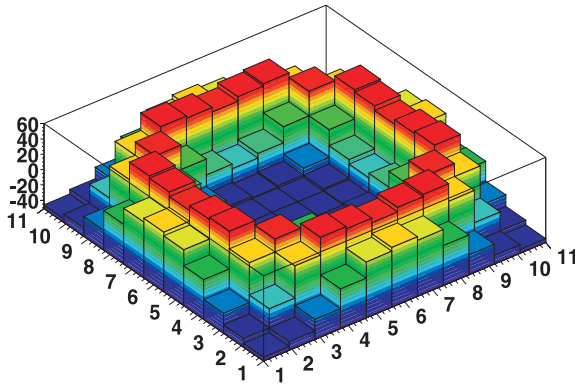

Figure 5.4: Schematic illustration of the pattern matrix method.

deformed because of the contribution of electronic noise or when two rings overlap.

5.1.3 Hough Transform Algorithm

The Hough Transform is a method used for object identification [Hou 62],[Ill 88],[Lea 93]. A specific class of objects (e.g. circles) must be chosen and a parameterization defined (e.g. the ring radius) that describes all possible instances of the object. Among the several algorithms that have been developed, the Randomized Hough transform (RHT) has been chosen for the HADES RICH analysis. Circles are parameterized as function of x, y and r where x and y refer to the position of the center and r to the ring radius. A two dimensional parameter space has been defined for circles, such that each circle maps to a single point in the parameter space. In each step, three pixels (fired pads in the label) are chosen and the unique circle passing through them is computed. The parameters x and y of the circle are saved. This operation is repeated for each triplet of pixels.

Because of the fixed radius of the rings and in order to reduce the computation time,

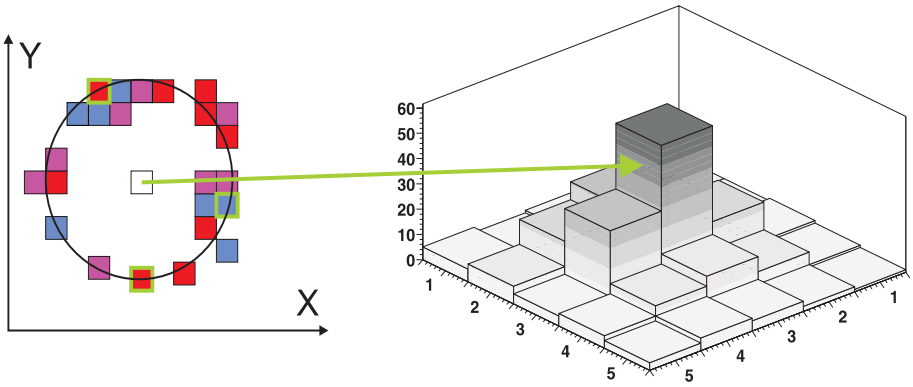

Figure 5.5: Schematic illustration of the Hough transformation method. The drawing on the left shows a label on the pad-plane and the circle that passes through the three green pixels. The right panel shows the two dimensional array where the ring centers are accumulated.

a condition is applied on the minimal distance between two sub-sequential pixels. This distance must be larger than half a ring radius. The final result is a two-dimensional array where the positions of the ring centers have been accumulated. In the next step of the analysis the maximum of this two-dimensional distribution has been determined. Figure 5.5 shows how the circles are calculated and the two dimensional array that contains one entry for each ring center position. The maximum in the center of this two-dimensional distribution indicates that this position has been the center of the circle for the majority of pad combinations. This position is taken as the center of the ring candidate.

The height of this maximum corresponds to the *Hough Transform Quality*.

The cleaner the ring shape the higher is the maximum, because all the calculated circles will have the same center.

The advantage of the Hough Transform algorithm is that it does not strictly depend on the radius of the circle and it is able to identify a ring even in case of distortions due

to the electronic noise contribution. The drawback is that the algorithm will recognize a ring even if it tests a large pad cluster. This characteristics, together with those of the PM algorithm, suggested to combine the two algorithms in the analysis, in order to reduce the contamination of the real signal as much as possible.

5.2 Results of the efficiency studies

As described in the previous paragraph, the ring finder algorithms deliver a certain quality. The higher the quality the better is the ring candidate. One can apply a threshold to both qualities to select only candidates that correspond to a higher probability for a real electron.
It has already been mentioned that the signal induced on the RICH pad-plane does not come only from Cherenkov photons. Some pads register a charge induced by electronic noise or by charged particles crossing the detector. Despite of the cleaning procedure that is applied before the ring search starts, there is still a fraction of pads with non-electron induced signal. This signal can eventually lead to patterns similar to rings. These rings do not correspond to any electron and will therefore be addressed as fakes. It can also happen that due to the low number of detected photons in a ring, the shape of the ring is not complete but the circumference is only partially occupied. In this case the ring finder algorithm can recognize the ring but it will eventually wrongly determine the position of the ring center. An identified ring in a wrong position has also been considered a fake.
The ring finder algorithms deliver a higher quality for real rings than for fakes, still there are some real electron rings for which a low quality is calculated. The dependence of the ratio between the algorithm efficiency and the fake contribution on different values of the quality threshold has been studied using the simulations. The resulting distribution will be addressed as the *Operating Curve* of the algorithm [Mue 95].
This curve is characterized by two quantities: the probability to misidentify a good candidate P(b|g), in other words 1-efficiency, and the fake probability P(g|b). The first term can be expressed with:

$$P(b|g) = \frac{N(g,b)}{N(g)}, \tag{5.1}$$

where $N(g,b)$ is the number of not-identified electrons and $N(g)$ is the number of electrons that are in the geometrical acceptance for which the identification is possible. The other parameter has the form:

$$P(g|b) = \frac{N(b,g)}{N(b)}, \tag{5.2}$$

where $N(b,g)$ is the number of fakes, i.e. the number of rings that do not correspond to a real electron or those that have a wrongly determined position. The position of the ring on the pad-plane is compared to the center of gravity of the emitted Cherenkov photons, which corresponds to the correct position of the ring. $N(b)$ is the number of fake candidates that in this case correspond to the total number of pads of the photon-detector. The operational curve has been calculated for the two algorithms separately for the following scenarios:

- single electrons coming from the target homogeneously distributed in momentum ($0 < p < 1000\ MeV/c$) and polar angle ($0 < \theta < 90°$),
- single electrons coming from the target embedded in a C+C at 2 $AGeV$ reaction,
- conversion electrons coming from the target and from other materials.

For each event it has been checked if there has been an electron/positron in the geometrical acceptance of the spectrometer and if this electron has been recognized as a ring in the correct position on the RICH pad-plane. All rings that do not correspond to any electron are counted as fakes. This analysis is repeated for different values of the ring finder algorithm thresholds. Since the quality delivered by the two algorithms is strictly correlated (see Figure 5.6), the discussion is limited to the dependency of the signal and fake efficiency on the pattern matrix quality.
The simplest case of a single electron produced in the target has been first investigated.

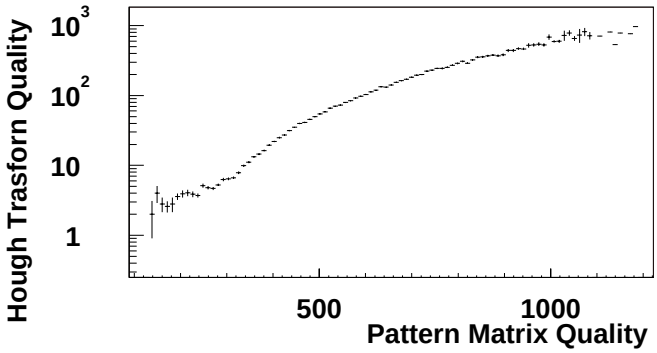

Figure 5.6: Hough Transformation quality as a function of the Pattern Matrix quality for candidates that have been found by both algorithms using the homogeneous electron generator as input.

The electronic noise of the detector is simulated in a realistic way (see section 4.3), but the contribution coming from the direct hits is not included in the simulations.
The simulation has been processed for two sets of optical parameters; one corresponding to the single photon efficiency obtained with the optical parameters shown in Figure 2.6, another that includes the reduced single photon efficiency measured in NOV02 and shown in Figure 4.29. It is important to compare the single electron efficiency obtained with the two parameter sets, to estimate the losses in the single electron efficiency after the corrections.
Figure 5.7 shows the pattern matrix algorithm inefficiency as a function of the pattern matrix quality. The stars represent the values obtained with the ideal single photon efficiency and the triangles the results obtained using in the simulation with the corrected single photon efficiency.
The range of the pattern matrix quality varies from 0 to 1500 units. The x-axis in Figure 5.7 represents a given threshold while the y-axis is the percentage of not-recognized electrons. This inefficiency stays quite constant and is equal to the minimum value

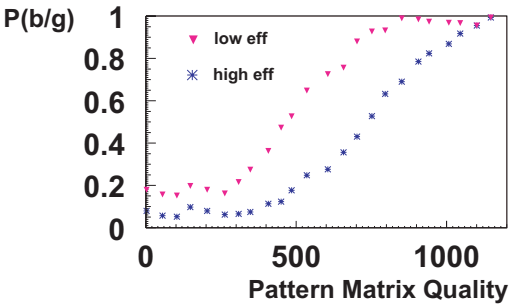

Figure 5.7: Inefficiency of the pattern matrix algorithm as a function of the increasing pattern matrix quality threshold.

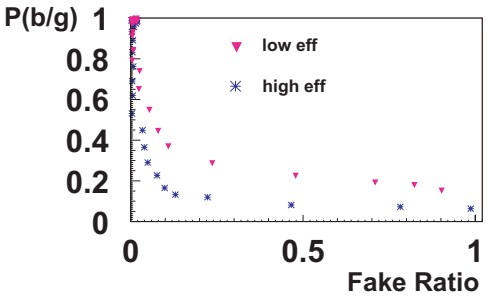

Figure 5.8: Inefficiency of the pattern matrix algorithm as a function of the fake ratio.

up to a certain threshold, then starts to increase steeply. The minimal value of the inefficiency is about 9% for the high single photon efficiency and 17% for the lower one. One can notice that the plateau is wider for the high efficiency, while the curve starts to become steeper starting from a smaller threshold value in the case of the reduced single photon efficiency.
In the first iteration of the electron analysis it has been tried to reject as few rings as possible, in a sort of minimum bias approach. Therefore the point on the plateau, that is next to the change of slope, has been chosen in Figure 5.7. This point corresponds to a Pattern Matrix Quality value of about 200.
Figure 5.8 shows the actual *Operating Curve*, that visualizes the inefficiency as a function of the fake ratio. The quantity plotted on the x-axis of figure 5.8 represents the ratio of fake rings to good rings and is direct proportional to P(g/b). It has been chosen for the graphical representation because it is easier to be interpreted.
In figure 5.8 one can see that the lower the inefficiency the higher is the fake ratio. The value of the PM quality of 200 leads to a fake ratio of about 50%.
If the PM quality is fixed, the corresponding threshold for the HT algorithm can be extracted from the correlation plot in Figure 5.6; this results to be 29 units. If the ring recognition is processed using the coincidence of the two algorithms, each with the thresholds just mentioned, the single electron efficiency can be calculated as a function of the momentum and polar angle of the electron.
Figure 5.9 and Figure 5.10 show the single electron efficiency of the RICH detector as a function of the momentum and polar angle, obtained with the chosen thresholds. The integrated efficiency amounts to 93% for the higher single photon detection efficiency (Figure 5.9) and to 84% for the lower single photon detection efficiency (Figure 5.10). The reduced single photon efficiency does not seem to introduce a similar strong reduction of the electron recognition efficiency.
The drawback is clearly the huge number of fake rings that are recognized with such low thresholds of the ring finder.

As second scenario, a distribution of electrons emitted in the target, homogeneously distributed in momentum and emission angles, has been embedded in a C+C at 2 $AGeV$ reaction. The simulation of the heavy ion reaction was done using the UrQmd model

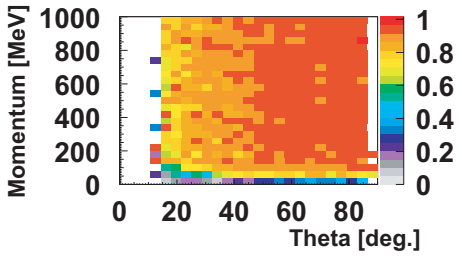

Figure 5.9: Single electron efficiency as a function of the momentum and polar angle of the incoming electron calculated for the ideal single photon efficiency.

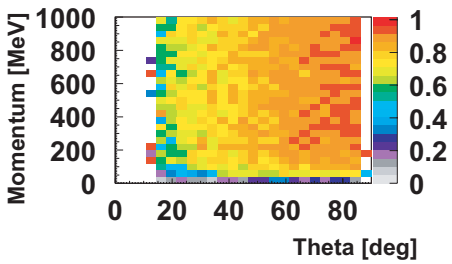

Figure 5.10: Single electron efficiency as a function of the momentum and polar angle of the incoming electron calculated using the corrected lower single photon efficiency.

(see section A.4) and the parameterization for the lower single photon detection efficiency. In this scenario the number of fakes might increase and the efficiency decrease due to the overlap of the electron signal with signals induced by the other reaction products. The efficiency has been calculated only for the electrons coming from the target.
The first step to decrease the number of fake rings without changing the ring finder thresholds is to correlate the found rings with the MDC hits reconstructed in the two planes placed before the magnetic field. The details about the determination of the spatial cut are given in A.2.
The spatial (section A.2) reduces the number of fakes but also the efficiency is reduced. The crosses in Figure 5.11 show the operating curve for a single electron coming from the target.
If this curve is compared with that in Figure 5.8, one can see that the maximum fake ratio is reduced from 100% to 20%. The maximal efficiency is reduced from 84% to 81%. In general, the strong fake reduction motivates the choice for this cut. The efficiency do not show any strong variation due to the heavy ion background, this is probably due to the fact that until now only light systems have been analyzed.

The third scenario concerns the e^+e^- that come from conversion processes. It has been seen in chapter 3 that the di-electrons coming from the conversion processes are very difficult to be treated, because of the small opening angle and contribute strongly to the combinatorial background. Hence, it is very important to study the response of the detector to the conversion pairs.
The same efficiency analysis has been applied to these electrons including the spatial correlation with the MDC segments and the results are shown in Figure 5.11.
The full circles show the inefficiency as a function of the fake ratio for e^+/e^- coming from γ conversion in the target. The empty squares show the inefficiency for the conversion products coming from other materials, mainly the radiator gas, inside the RICH.
One can see that the efficiency for the e^+/e^- coming from γ-conversion drops dramatically to a maximum value of 30% and that the fake ratio increases to a maximum value of 2. This value means that the number of found fake rings is twice the number of rings

that correspond to an electron.

The reason for which the efficiency decreases is twofold. First the momentum dis-

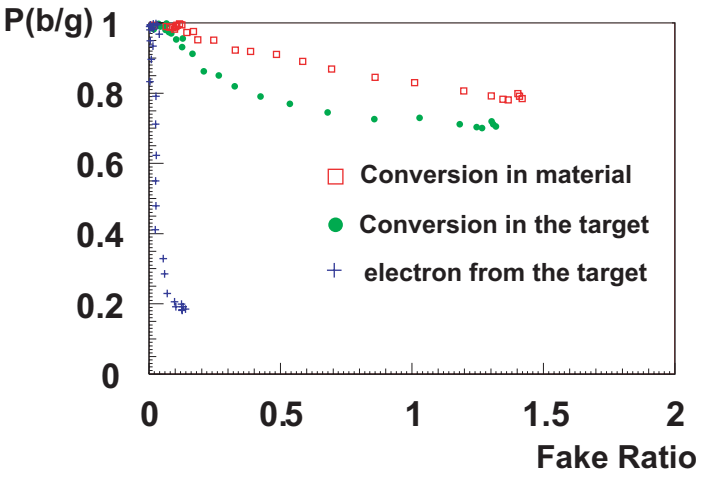

Figure 5.11: The operating curve is shown for free electrons produced in the target, where each ring is correlated spatially with the MDC segment (cross-like points) and for the electron/positron produced in conversion processes that take place in the target (full circles) and in other materials in the RICH detector (squared points).

tribution of the e^+/e^- from conversion processes is dominated by small momenta ($< p >< 80\ MeV/c$) due to the abundant occurrence of low energy photons. From the Cherenkov threshold ($p_{thr.} \approx 10 MeV/c$) up to momenta of 50 MeV/c too few photons are produced to enable the recognition of a ring. Secondly, particles with low momenta have a higher probability to undergo the multiple scattering process. In this case, a mismatch between the position of the particle on the MDC detector and the ring position occurs.

Figure 5.12 shows the identification efficiency of a single e^+/e^- produced in a γ conversion process in the target as a function of the momentum (continuous line) together with the momentum distribution (dashed line). One can see that the largest efficiency losses are localized at very low momenta ($p < 50\ MeV/c$) and that most of the e^+/e^- have momenta lower than 50 MeV/c.

So far only the response of the RICH detector has been investigated, but there are other factors that influence the detection efficiency of the e^+/e^-. For the standard setting of the magnetic field (about 0.5 T) all the particles with momentum lower than 50 MeV/c are bent outside the acceptance of the spectrometer. Many of the di-electrons produced in conversion processes are not tracked in the whole spectrometer and the reconstruction efficiency is very low. If investigations are limited to the RICH detector response, it has been estimated that for the system C + C at 2 $AGeV$ among the

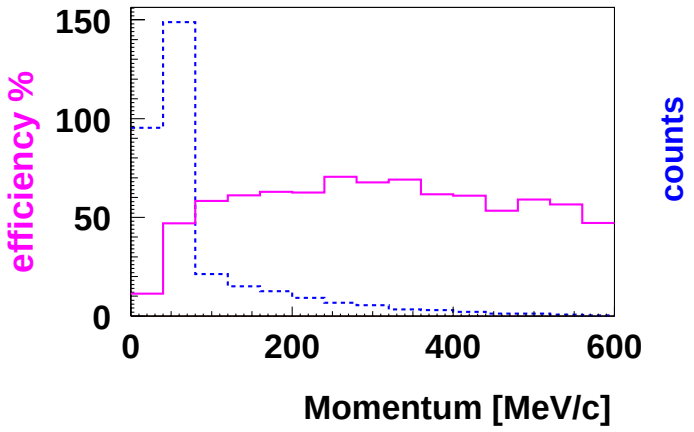

Figure 5.12: Single electron efficiency as a function of the momentum for e^+/e^- produced in conversion processes.

found rings 10% are electrons coming from the target ($\pi^0 \rightarrow \gamma e^+ e^-$), 40% electrons from conversion processes and 50% fakes. Moreover it has been seen that the correctly identified e^+e^- from the target correspond to the 60% of all the e^+e^- in the spectrometer acceptance.

5.3 Comparison to experimental data for C+C at 2 $AGeV$

So far all the results have been obtained from simulations. The UrQMD simulations have been used only as background for the efficiency studies but they can be used more extensively and compared with experimental data. The ring candidates found in simulation and in experimental data can be compared, additionally a selection strategy for $e^{/} + e^-$ can be developed, that, starting from the hit candidates, tries to reduce the fake contamination in both samples.
The experimental data used for this analysis have been taken in the winter of 2001 (NOV01) with a 1 and 2 $AGeV$ C beam on a ^{12}C target.
The spectrometer set-up was composed of: the fully equipped RICH detector, 12 MDC modules before the magnet (MDC 1/2), 2 MDC modules after the magnet (2 sectors of MDC 3), fully equipped TOF/Tofino and Pre-Shower detector.
The centrality selection was $\sigma/\sigma_{geo} \approx 10\%$ obtained with the first level trigger set using a threshold of at least 4 charged particles in the META detector. The total number of analyzed events was around 40 millions.
Parallel to the analysis of the experimental data, about $20{\cdot}10^6$ simulated events have been analyzed. The simulation done with an UrQMD input have been analyzed with the same trigger condition as the experimental data. For the parameterization of the RICH detector a modified photon detection efficiency has been used, that has been adjusted for the NOV01 experimental data (for details see A.3).

5.3.1 Selection of ring candidate

For each event, in both simulated and experimental data, the following procedure has been applied:

- First, the track segments in the first two MDC planes before the magnet are reconstructed, then the segments are matched with hits on the META detector. The *kickplane* method [San 03] (see A.5) has been used to select the combinations with the best quality and determine the momentum together with the velocity information from the time of flight and the mass of each particle. The polar coordinates θ, ϕ assigned to each track define the impact position of the particle candidate on the MDC modules before the magnet.

- Rings found in the RICH with the algorithms described in paragraph 5.1 were evaluated. The polar coordinates corresponding to each ring center define the impact of the electron/positron on the mirror.

Finally the hits in the two sub-detectors RICH and MDC have been matched according to the cuts defined in paragraph A.2. After the matching there is still a fraction of the tracks which rings could be fakes. A fake ring might still be matched with a reconstructed track, the track could be itself a fake or belong to a hadron.

5.3.2 Ring Properties and fake suppression

The rings have been classified on the basis of their quality. The quality of each ring is characterized by the following quantities:

- the number of pads that compose a ring,

- the total ring-charge, calculated as the sum of the charges of all the pads that compose a ring,

- the pattern matrix quality (see section 5.1),

- the centroid, meant as the difference between the center of gravity as deduced from the pulse height and the geometrical center of the ring

- the number of local maxima, calculated looking for charge local maxima among all the pads that compose a ring (see section4.4.1).

In Figure 5.13 - 5.17 the distributions of the ring properties for simulated and experimental data are shown. All the rings have been used only once to fill these histograms, that means that the contribution of the multiple matching to the total fake ratio is not taken into account yet.
One can see that the distribution of the ring properties is very similar between the experimental and simulated data. The simulated distributions show together with the total signal the contribution coming from fake rings and real e^+e^-.

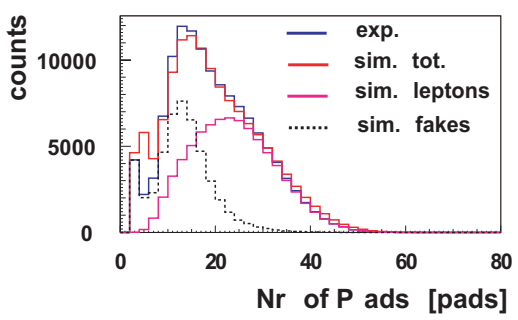

Figure 5.13: Distribution of the number of pads per ring, the experimental results are shown together with the simulations. The same number of events has been analyzed for the experimental and simulated data.

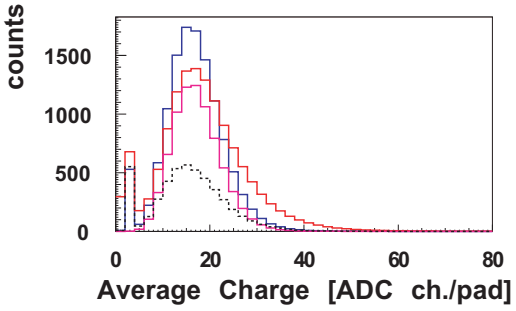

Figure 5.14: Average charge distribution for experimental and simulated rings, normalization and color-code are the same as in Figure 5.13.

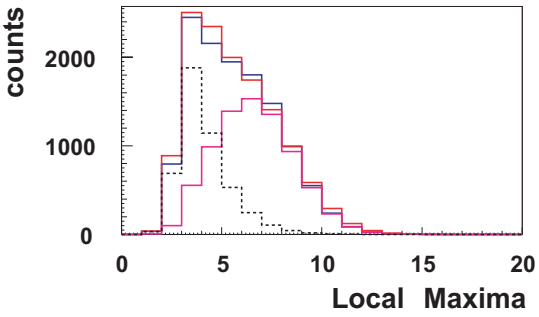

Figure 5.15: Local maxima distribution for experimental and simulated rings, normalization and color-code are the same as in Figure 5.13.

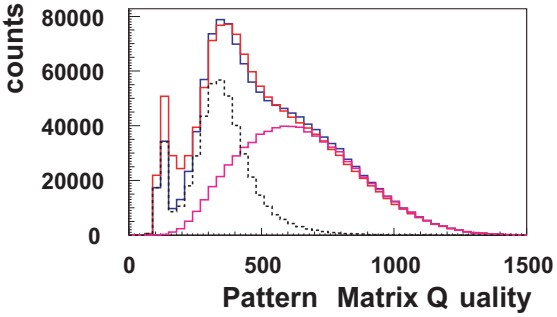

Figure 5.16: Pattern Matrix quality distribution for experimental and simulated rings, normalization and color-code are the same as in Figure 5.13.

The good agreement between the simulated and experimental ring properties entitles us to rely on the real/fake classification delivered by the simulation information. Among the rings correlated with one track there are still 10% of fakes. One can see from the figures that there are no cuts on the parameters that allow the rejection of all the fakes and keep all the good electrons. Because of the limited statistics accumulated in NOV01, conservative cuts have been used, able to preserve most of the signal. A two-dimensional analysis of the ring-parameter distributions suggest the following cuts:

- Nr. of pads in a ring > 5
- PM quality > 200
- Ring-centroid < 2.8
- Average charge > 5

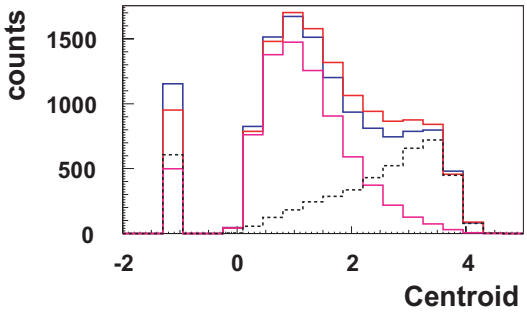

Figure 5.17: Ring centroid distribution for experimental and simulated rings, normalization and color-code are the same as in Figure 5.13.

- Nr. of local maxima > 4

These cuts on ring properties, which from now on are addressed as "good ring cut", allow to reject 40% of the fakes and keep 85% of the good signal. The e^+e^- ensemble leftover after the cuts contains 80% of good rings and 20% of fakes.

Chapter 6

Response of the HADES spectrometer to di-electron pairs

The analysis of the NOV01 experimental and simulated data has been performed also for the e^+e^- using the cuts on ring properties that have been described in chapter 5. Other cuts have been additionally developed that employ the information delivered by other sub-detectors to reduce the amount of fakes [Ebe 03]. The aim of this analysis is to get a di-electron pair signal for which the contamination by wrongly reconstructed tracks is as low as possible. From now on the wrongly reconstructed pairs will be addressed as fakes, the exact classification of fake pairs follows in this chapter. The investigation of the low di-lepton invariant mass region was carried out to evaluate the response of our spectrometer to the π^0-Dalitz channel.
Once the selection cuts are developed, the pair efficiency and fake probability for the NOV01 data and for the applied cuts are calculated, in order to correct the reconstructed pair distribution. Since the fake probability and pair-efficiency change as a function of the analysis cuts, this dependence has been investigated quantitatively. Additionally the geometrical acceptance of the whole spectrometer has been calculated.
The efficiency and fake probability corrections have been used to correct the simulated and experimental invariant mass distributions of the reconstructed e^+e^- pairs.

6.1 Input and geometrical acceptance

The calculation of the pair efficiency and of the fake probability has been done using the simulations. A so called "white"pair source generator has been used, with invariant mass (M) homogeneously distributed between 0 and 2.5 GeV/c^2, transverse momentum (P_t) between 0 and 2 GeV/c and rapidity (Y) between -2 and 3. One of these pairs has been embedded in each event produced with the UrMQD code for the reaction C + C at 2 $AGeV$, to simulate a realistic background.
300000 events have been processed, for e^+e^-, e^+e^+, and e^-e^- pairs separately. Figure 6.1 show the mass (M), the transverse momentum (P_t) and rapidity (Y) distributions of the pairs in the input. The contributions coming from the white generator and from the C + C reaction products are shown separately.
The geometrical acceptance of the spectrometer for the NOV01 setup (5.3) is defined as the fraction of produced pairs which cross both the two inner MDC planes and the META detector. The geometrical acceptance is again a function of M, P_t and Y. Figure 6.2 shows the geometrical acceptance distribution as a function of M and P_t for

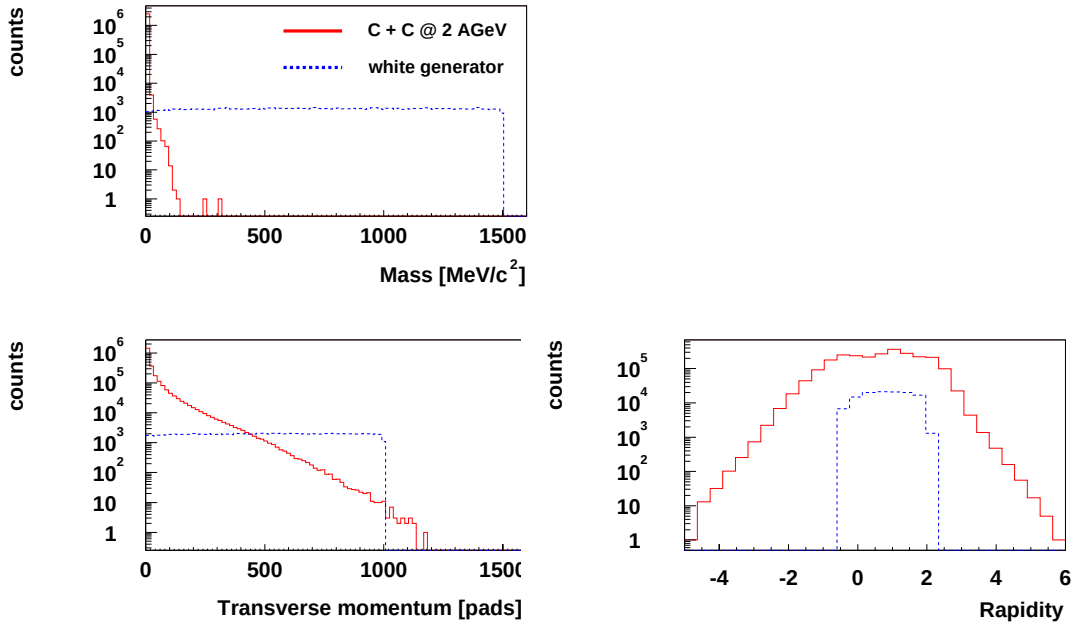

Figure 6.1: Invariant mass, transverse momentum and rapidity distributions of the simulation of e^+e^- pairs used as simulation input to calculate the di-electron efficiency. The white distribution is overlapped to the di-electron distribution predicted by UrQMD for the C + C reaction at 2 $AGeV$ incident energy.

the unlike-sign and like-sign pairs. The distribution in Y is not shown here, because it is quite homogeneous. One can see that the di-electron acceptance of the HADES spectrometer is relatively homogeneous between unlike and like-sign pairs. The acceptance is quite low for low M and P_t values $(5-10\%)$ and quite constant (35%) for $M > 150 MeV/c^2$ and $P_t > 150\ MeV/c$. The acceptance distributions (see Figure 6.2) as a function of M and P_t, show a lower acceptance for the low P_t positive like-sign pairs in comparison with the negative ones. This implies that the response of our spectrometer to negative and positive like-sign pairs is not the same, but the difference lies within 10%.

6.2 Di-electron efficiency and fake probability

The input pairs that are emitted in the spectrometer acceptance can induce a signal in the sub-detectors and be reconstructed.
The HGeant track informations are translated in detector signals (e.g. chapter 4) and the hit finder search for candidate in each sub-detector (e.g. section 5.1) is executed. The hits reconstructed in the different sub-detectors are matched together and e^+/e^- tracks are identified. Once reconstructed, the e^+/e^- tracks are event-wise combined in like-sign and unlike-sign pairs. The information about the particles contained in the simulation enables the identification of those reconstructed pairs that do not correspond

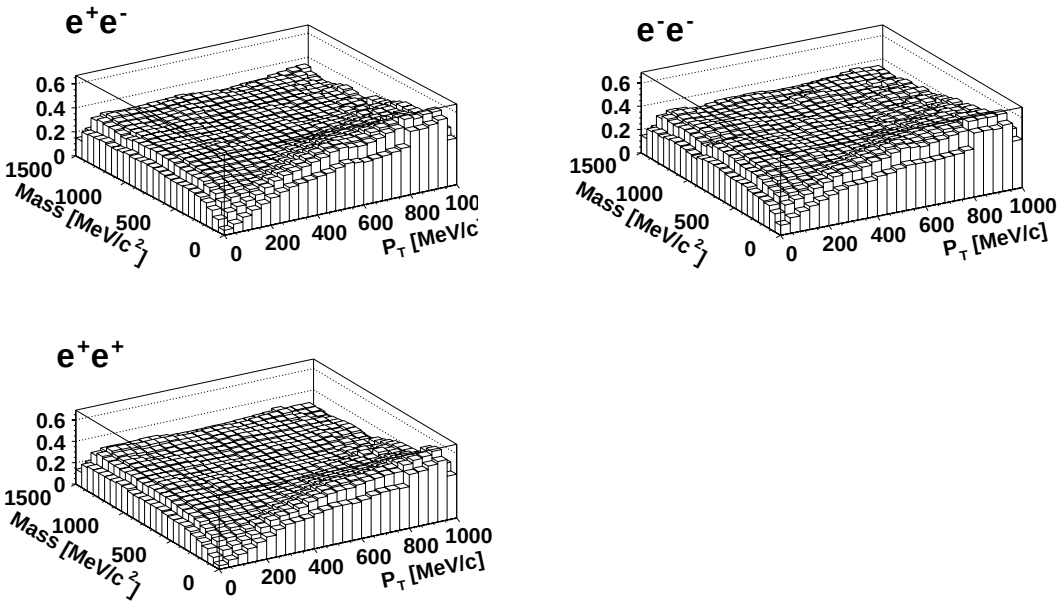

Figure 6.2: Pair acceptance as a function of M and P_t for unlike-sign, positive and negative like-sign pairs.

to any physical e^+/e^- pair and to calculate the overall efficiency of the spectrometer. In the following subsections the analysis cuts are explained, that have been used to select the e^+/e^- pairs sample. The estimation of the systematic error on the pair properties is discussed and the efficiency and fake probability are calculated.

6.2.1 Cuts for the selection of e^+/e^- pairs

For each reconstructed di-electron (unlike and like-sign) pair the following cuts are applied [Ebe 03]:

1. both track candidates must be correlated within q 3σ window defined in section A.2 with rings that fulfill the "good ring cut",

2. both tracks must be recognized as leptons in the β-momentum plane developed on the basis of the t.o.f. information [Zov 03],

3. both tracks must be characterized by a good matching between the MDC segments and the META hit via the kickplane method [San 03], (see A.5),

4. the Pre-Shower condition for a lepton must be fulfilled by both tracks,

5. all the pairs that have the same RICH ring and the same MDC segment in common are rejected,

6. all the pairs for which the two candidates have the same META hit are rejected,

7. all the pairs with opening angle smaller than 4° are rejected.

The fake probability and pair efficiency dependence on these cuts is calculated for each cut separately. In particular the effect of the sequential addition of the cuts from one to seven are shown in the next section.

6.2.2 Error propagation

Together with the efficiency, acceptance and fake correction, the systematic error on the dependent variables α (opening angle), M (invariant mass), P_t (transverse momentum) and Y (rapidity), that characterize a pair, has been estimated.
The error has been propagated to the dependent variables making use of the following formulas:

$$\begin{aligned}
\alpha = & \arccos[\sin(\theta_{e^+})\cos(\phi_{e^+})\sin(\theta_{e^-})\cos(\phi_{e^-})+ \\
& \sin(\theta_{e^+})\sin(\phi_{e^-})\sin(\theta_{e^-})\sin(\phi_{e^-})+\cos(\theta_{e^+})\cos(\theta_{e^-})]. \\
M = & \, 2\sin\frac{\alpha}{2}\cdot\sqrt{p_{e^+}p_{e^-}}, \\
P_t = & \, p_{e^+}\sin(\theta_{e^+})+p_{e^-}\sin(\theta_{e^-}), \\
Y = & \, \frac{1}{2}ln\left(\frac{E+P_l}{E-P_l}\right), \qquad (6.1)
\end{aligned}$$

where

$$\begin{aligned}
E = & \, E_{e^+}+E_{e^-}=\sqrt{p_{e^+}^2+m_{e^+}^2}+\sqrt{p_{e^+-}^2+m_{e^-}^2} \\
P_l = & \, P_l^{e^+}+P_l^{e^-}=p_{e^+}\cos(\theta_{e^+})+p_{e^-}\cos(\theta_{e^-}) \\
c = & \, 1.
\end{aligned}$$

The sources of error for the determination of M, P_t, Y and α of one e^+/e^- pair are: the polar and azimuthal coordinates θ and ϕ and the reconstructed momenta p of the e^+/e^- tracks. No error on the rest mass has been assumed, since its values have been taken from the Particle Data Book once the identity of the particle had been determined.
The polar and azimuthal coordinates θ_{e^+}, θ_{e^-}, ϕ_{e^+}, ϕ_{e^-} are estimated by the track finder algorithm in the MDC detector [San 03]. This algorithm introduces an average uncertainty (error) of 0.19 *mrad* for the polar coordinate and 1 *mrad* for the azimuthal coordinate. Figure 6.3 shows the distributions of the uncertainty for the polar and azimuthal coordinates. These results were obtained using Monte Carlo simulations. The two distributions can be approximated with a Landau function; the maximal error on θ and ϕ has been set as the most probable value + 3σ, where σ is the width of the two distributions respectively ($\sigma_\theta = 0.03$ *mrad* and $\sigma_\phi = 0.2$ *mrad*)).
Additionally to these errors the uncertainty determined by the multiple scattering has been taken into account. For the e^+/e^- the width of the polar and azimuthal distribution due to the multiple scattering depends on the particle momentum [Eur 98]:

$$\Theta_0^{rms} = \frac{13.6MeV}{p}Z\sqrt{\frac{x}{X_0}}\left(1+0.038\ln\frac{x}{X_0}\right), \qquad (6.2)$$

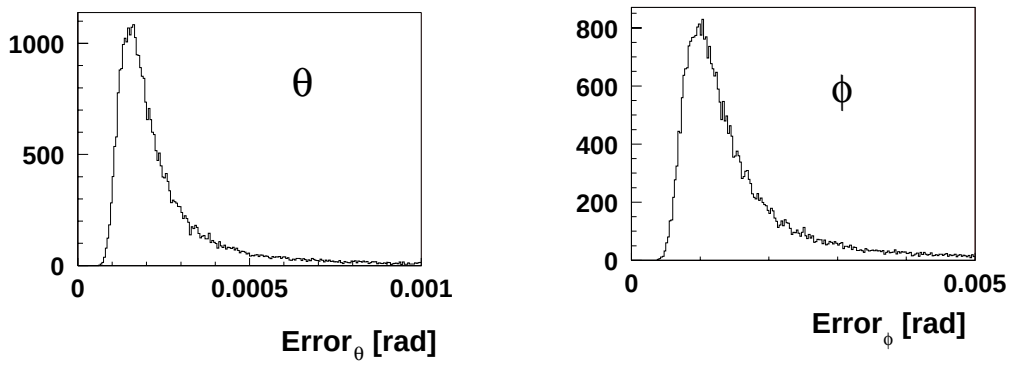

Figure 6.3: Distribution of the uncertainty introduced by the track finder on the θ (left panel) and ϕ (right panel) coordinates.

where Θ_0^{rms} is the mean scattering angle, p the particle momentum in MeV/c, Z = 1 for e^+/e^-, X_0 the radiation length of the material that the e^+/e^- cross and x the path length. The radiation length and the path length of the materials contained in the RICH detector that more strongly contribute to the multiple scattering are listed in table 2.1 and [Kas 00]. These parameters lead to an uncertainty of about 5.5 mrad in θ and ϕ for an electron of 0.5 GeV/c.
The total error on the angular coordinates is given by the quadratic sum of the track-finder resolution and multiple scattering resolution. This leads on average to an error of about 6 mrad for θ and 8 mrad for ϕ.

In Figure 6.4 the uncertainty (error) introduced by the kickplane method by reconstructing the particle momentum is shown as a function of the momentum. The error on the reconstructed momentum ($Error_{P_{REC}}$) increases with the increasing momentum and varies between 4% and 10%.
In order to check these error values delivered by the kickplane, the difference between

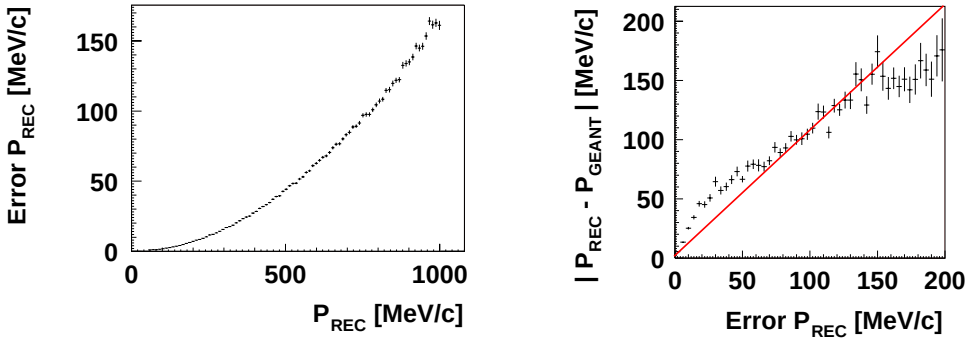

Figure 6.4: In the left panel the uncertainty on the reconstructed momentum is shown as a function of the momentum. The right panel shows the difference between the ideal and reconstructed momentum as a function of the uncertainty on the reconstructed momentum.

the reconstructed momentum and the ideal momentum of a particle has been checked in the simulations. The right panel of Figure 6.4 shows the difference between the ideal and reconstructed momentum as a function of the error on the reconstructed momentum. It can be seen that the center of mass distribution on the right panel lies above the diagonal up to 100 MeV/c error values. This means that for smaller momenta there is a higher deviation between the calculated and the real momentum.

Figure 6.5 shows the error propagated on the dependent variables following equations (6.1) . The first panel in Figure 6.5 shows the distribution of error on the reconstructed P_t for the intervals 90 $MeV/c < P_t < 110 MeV/c$ and 390 $MeV/c < P_t < 410$ MeV/c. The sigma extracted by the Gauss fit of the two distributions is for both about 10% of the average P_t value. The second panel in Figure 6.5 shows the distribution of the error on the reconstructed M. The width of the error distribution changes in this case from 5% for the mass interval 90 $MeV/c^2 < M < 110$ MeV/c^2 to 10% 390 $MeV/c^2 < M < 410$ MeV/c^2. This dependence of the pair mass resolution upon the pair mass reflects the behavior of the error on the reconstructed momentum. The third panel in Figure 6.5 shows the error distribution for the reconstructed rapidity. The width of this distribution is independent of the rapidity range and corresponds to about 2%.

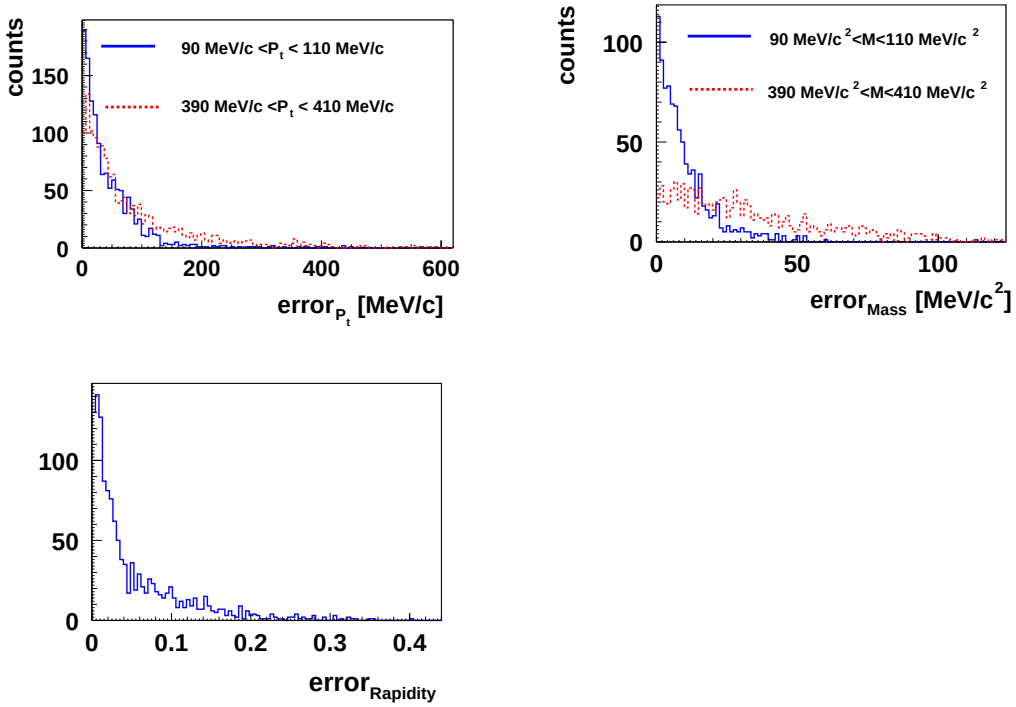

Figure 6.5: Propagated error on the dependent variables M, P_t and Y. *top left:* the error distribution for the reconstructed P_t is shown for two momentum intervals, *top right:* the same is shown for the variable M, *bottom:* the average error distribution for the rapidity is shown.

6.2.3 Pair efficiencies

Among the reconstructed pairs, there are some that correspond to a real input pair and some others that are fakes. The simulated reconstructed pairs still carry the information about the Geant track numbers of the parent particles and can be compared to those of the input pairs. A reconstructed pair has been accepted in the efficiency matrix only if the track numbers of the two pair-partners match with the corresponding HGeant track numbers. Additionally, it has been checked that the reconstructed momentum p of the two pair-partners is equal to the ideal momentum calculated in HGeant within a 3σ cut. With this cut about 12% of the pairs have been lost.

The pair efficiency is a function of M, P_t, Y and the opening angle α. The efficiency is reduced for small angles ($\alpha < 10°$), where two tracks are reconstructed as one or not reconstructed at all. First the efficiency and fake distributions obtained after all the analysis cuts mentioned in the list above are shown.

A relative and an absolute efficiency can be calculated. The relative efficiency is normalized to the number of pairs in the acceptance, it is built dividing the number of reconstructed pairs with a given M, P_t, Y and α by the number of pairs in the acceptance with the same M, P_t, Y and α.

$$Eff_{relative} = \frac{Nr.\ of\ correctly\ reconstructed\ pairs}{Nr.\ of\ pairs\ in\ acceptance} \tag{6.3}$$

Only the pairs from the white generator are used to calculate the efficiency matrix. Figure 6.6 shows the relative efficiency distribution for unlike-pairs as a function of all the bi-combinations of M, P_t, Y and α after all the cuts listed in section 6.2.1 have been applied. This efficiency reflects the hardware properties of all the sub-detectors folded into the digitization procedures and the reconstruction software efficiency. It can be seen that the pair reconstruction efficiency depends very strongly on M, P_t and α. In particular the efficiency is lower for values of mass $M < 200\ MeV/c^2$ and transverse momentum $P_t < 200\ MeV/c$. This shows that the spectrometer design is not optimized for the reconstruction of the π^0-Dalitz pairs, that are to be found in this lower mass region. One notices the efficiency losses for small opening angles due to the finite resolution of the software.

The absolute efficiency is calculated normalizing the number of reconstructed pairs to the total number of input pairs, hence multiplying the relative efficiency matrices with the geometrical acceptance shown in 6.2.

$$Eff_{absolute} = \frac{Nr.\ of\ correctly\ reconstructed\ pairs}{Nr.\ of\ pairs\ in\ input} \tag{6.4}$$

Figure 6.7 shows the absolute unlike-sing pairs efficiency as a function of all the bi-combinations of the variables M, P_t, Y and α after all the cuts listed in section 6.2.1 have been applied. One can see that the maximum efficiency is about 30% and it is reached in the region of high P_t and high α. This shows the combined effect of the geometrical acceptance and of the detector efficiency. In particular it has been observed [Ebe 03] that the efficiency of the RICH is higher for particles with higher P_t. These particles are emitted at higher polar angles and travel a longer path in the radiator gas, producing more Cherenkov photons. Another reason of the higher efficiency for

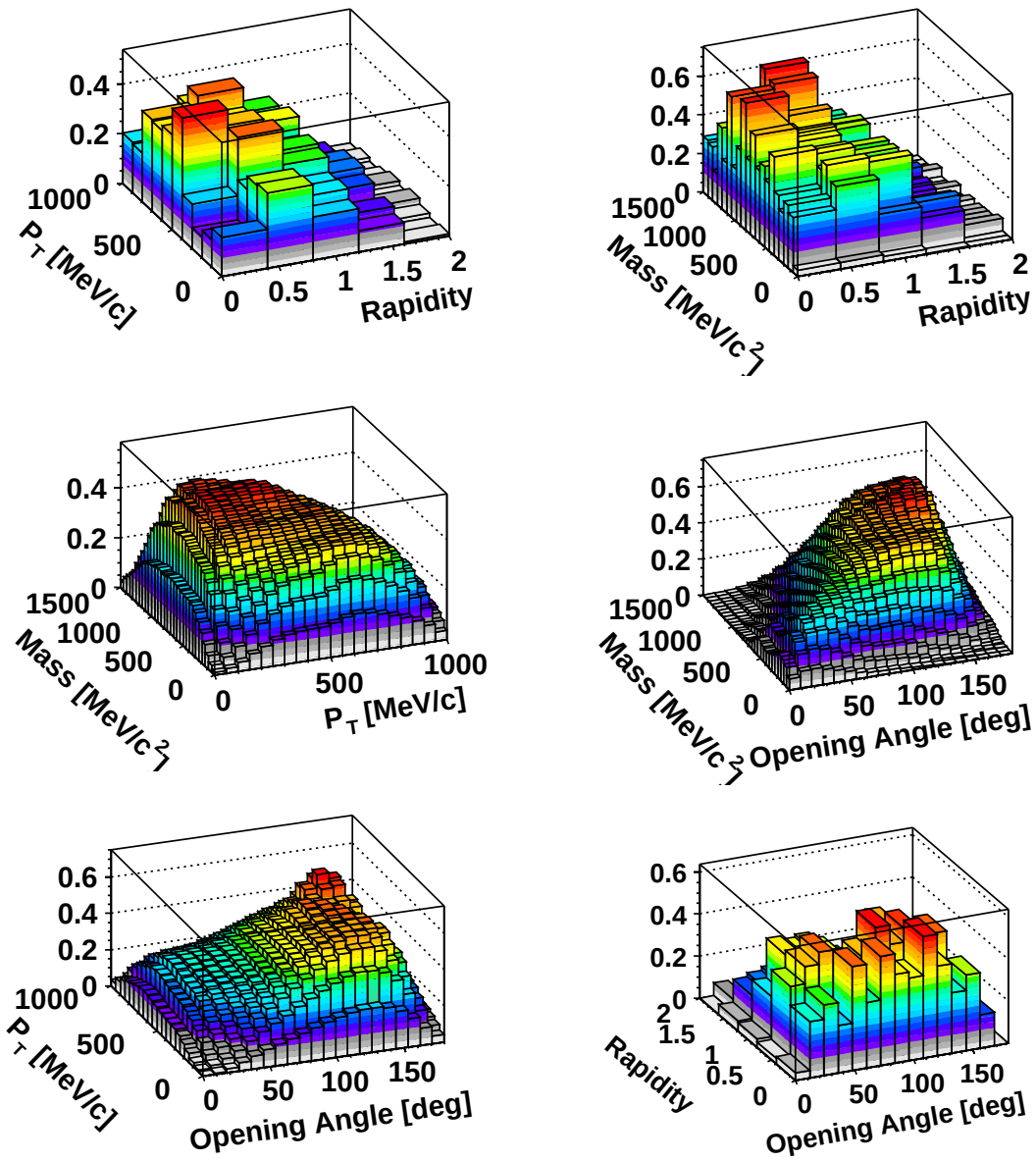

Figure 6.6: Unlike-sign relative pair efficiency. The number of correctly reconstructed pairs have been normalized to the pairs in the geometrical acceptance, as a function of M, Y, Opening Angle and P_t.

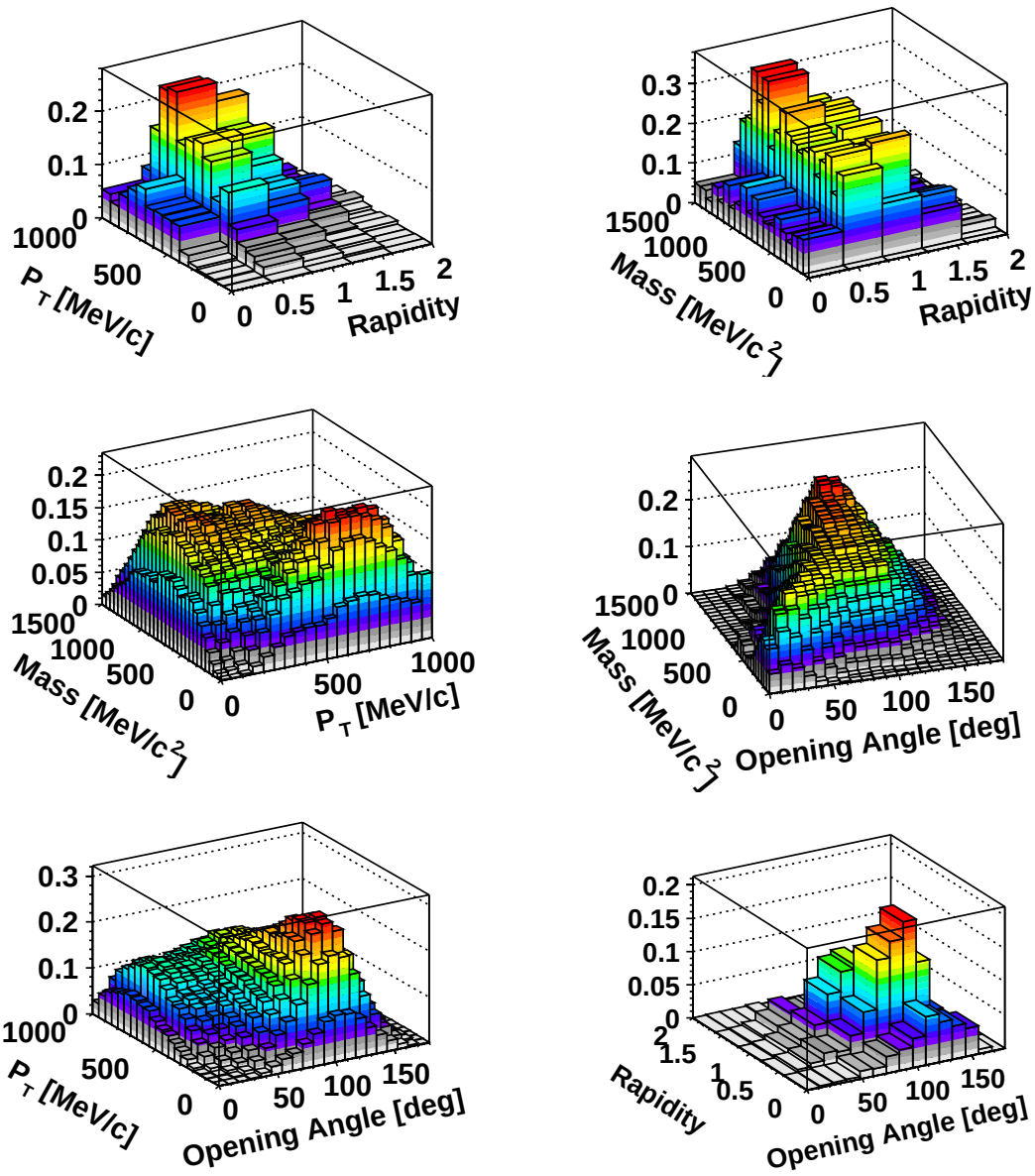

Figure 6.7: Unlike-sign absolute pair efficiency. The number of correctly reconstructed pairs has been normalized to the number of pairs in input, as a function of M, Y, Opening Angle and P_t.

higher P_t is the lower occupancy of the whole spectrometer at higher polar angle.
So far only the relative and absolute efficiency for the unlike-sign pairs have been shown. The corresponding histograms for the like-sign pairs do not show any striking difference with respect to the unlike-sign pairs. This is mainly due to the fact that the efficiency has been calculated using only the pairs produced by the white generator.
The di-electron pairs produced in the C + C at 2 $AGeV$ collisions mainly come from π^0-Dalitz and γ-conversion processes. The e^+e^- pairs produced in these processes cover a phase space corresponding to low masses ($M < 135\ MeV/c^2$), relatively low values of P_t ($70MeV/c < P_t < 350\ MeV/c$), low opening angle and relatively homogeneously distributed in Y.

As it has been shown in section 5.2, the detection efficiency for conversion products

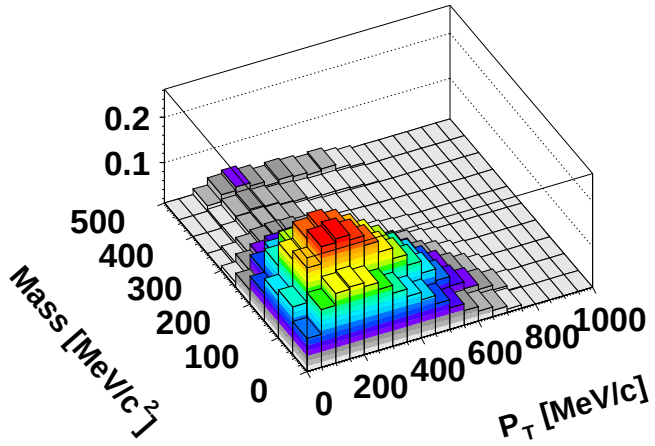

Figure 6.8: Relative detection efficiency for the e^+e^- pairs produced in γ-conversion processes in the geometrical acceptance of the HADES spectrometer. The efficiency is shown as a function of M and P_t.

is lower than the efficiency for electrons coming from the target. This means that if the relative efficiency shown in figure 6.6 can be used for the correction of all the pairs produced in the target, one can not do the same with the conversion-pairs that are mainly produced in the gas radiator (see figure 3.4).
Figure 6.8 shows the detection efficiency for the di-electron pairs produced in γ-conversion processes in the geometrical acceptance in the reaction C + C at 2 $AGeV$. The mass reconstructed from such a di-electron pair is the equivalent relativistic mass of the photon energy. This relative efficiency is significantly lower than the one obtained with the white generator input, and must be taken into account in the correction of the final spectra.

6.2.4 Fake pair probability

All the reconstructed pairs that do not fulfill the condition on the momentum and which HGeant track numbers do not match with any pair in the input are considered as fakes. For each chosen bin of M, P_t and Y the fake probability is calculated as follows:

$$Fake\ probability = \frac{Nr.\ of\ fake\ pairs}{Nr.\ of\ fake\ +\ Nr.\ of\ correctly\ reconstructed\ pairs} \tag{6.5}$$

Among the wrongly reconstructed pairs there are those formed by fully reconstructed tracks that come from different vertices. They build up the combinatorial background and hence have not been included in the evaluation of the fake probability.
Furthermore the not fully reconstructed tracks stemming from the two different inputs (di-electrons produced in the C+C reaction and white pairs generator) can not be mixed together when the fake pairs are counted.
In this way the fake probability includes only the contribution of the wrongly reconstructed pairs due to the limited precision of the analysis software.

Figure 6.9 shows the fake probability distribution for unlike-sign pairs. One can see that the maximum values of the fake probability are reached at small values of M, P_t and α. These results have been achieved after all the 'pair' cuts have been applied. One can see that despite of the applied cuts, there is still a large fraction of so called 'fake pairs' in the low mass region. Especially the fake probability distribution as a function of M and α shows that the presence of fake pairs is due to the lack of precision in the tracking procedure, since the fake probability is very high for low masses independently from the opening angle.
The fake probability and the efficiency depend on the applied cuts. The efficiency and the fake probability change with an increasing number of applied cuts, if the list shown at the beginning of 6.2 is considered. One cut for each analysis step was sequentially added, in the order given in the cut list.
Figure 6.10 shows the average fake probability and the average relative pair efficiency as a function of the different cuts. The average fake probability and average efficiency are obtained averaging the distributions shown in Figure 6.9 and figure 6.6 over the whole available range for the variables P_t, α and Y and integrating M in the three intervals: $0 < M < 135 MeV$ (up to the π^0 mass), $135\ MeV < M < 1500\ MeV$ and $0 < M < 1500\ MeV$. The effect of these cuts in the mass region below and above 135 MeV/c^2 are shown separately.
The relative efficiency is about 50% when no cuts are applied and a fake probability is 85%, for the unlike-sign pairs in the region below the π^0 mass. That means that without any cut, 85% of the signal is not correctly reconstructed and the 15% left corresponds to 20% of the total di-electron yield in this region. These values change to 28% for the fake probability and to 28% for the relative efficiency after all the cuts. The effect of the cuts is very efficient for the fake reduction only in the low mass region, if the fake probability and the efficiency are averaged along the whole range, the effects are not so strong. A similar behavior can be seen on the second and third panel that show the cut dependency for the negative and positive like-sign pairs respectively. The pair recognition efficiency is slightly higher for the unlike-sign pairs than for the like-sign pairs and the fake probability is lower. This can be due to the fact that the like-sign

pairs are bent in the same direction from the magnetic field and therefore the two-hits position resolution on the META is lower.
There is no major discrepancy between the positive and negative like-sign pairs.
The combination of the efficiency and fake probability matrices can be used to correct the analyzed e^+e^- distributions. One can see from Figure 6.7 and Figure 6.9 that both the efficiency and fake distributions do not depend very strongly on the rapidity.

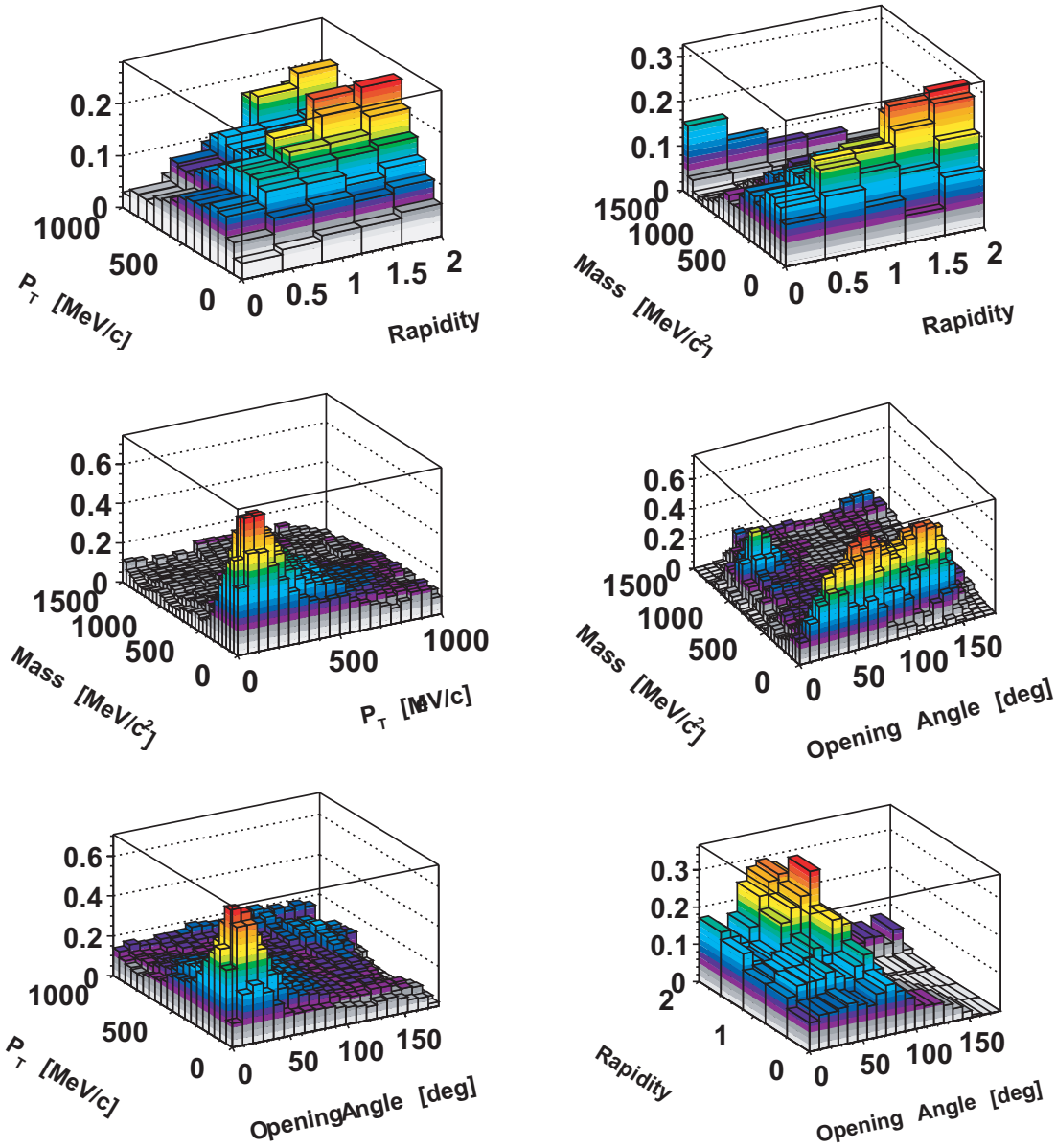

Figure 6.9: Fake probability calculated with equation (6.5) for unlike-sign pairs, as a function of M, Y, Opening Angle and P_t.

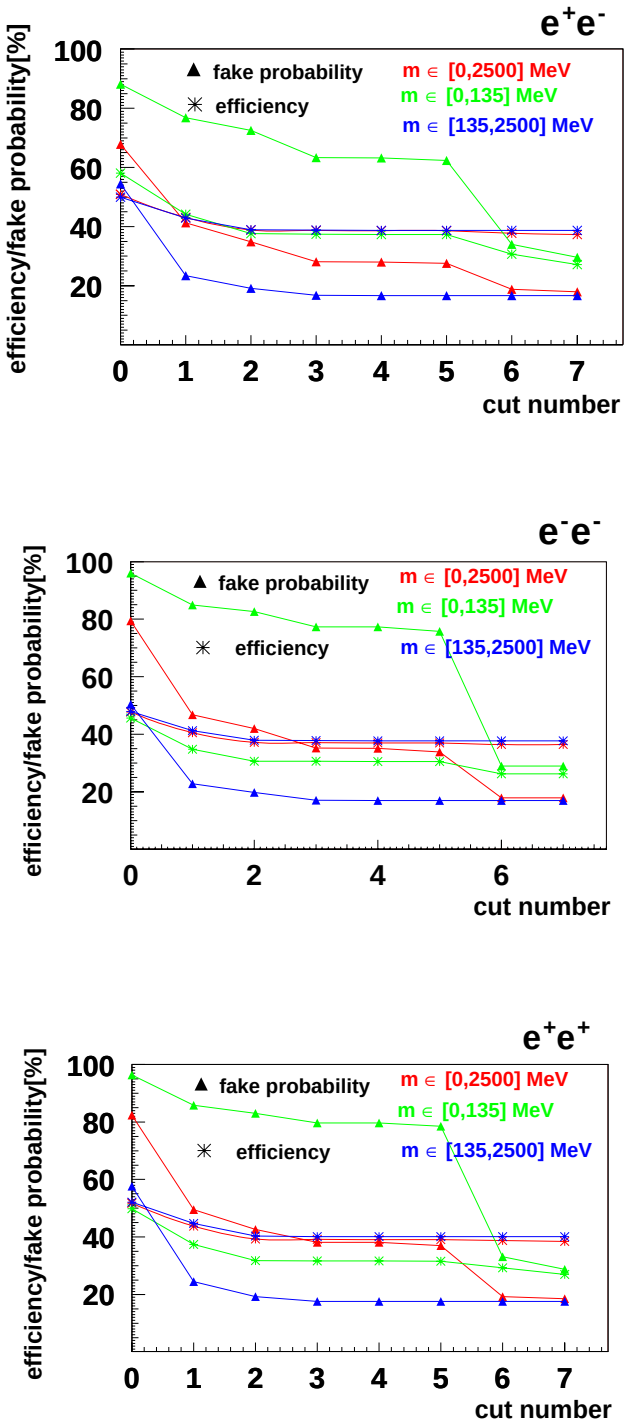

Figure 6.10: Dependency of the fake probability and relative pair efficiency on the number of the successively applied cut. *top:* the results for the unlike-sign pairs are shown, the behavior of efficiency and fake probability in the different mass ranges are visualized separately, *middle and bottom:*the results for the negative and positive like-sign pairs are shown.

Therefore it is possible to integrate over this variable for further correction calculations. Furthermore, it is known that the e^+e^- pairs produced in the C + C at 2 $AGeV$ show a yield maximum for small opening angle and relatively small M. Taking again into account Figure 6.7 and Figure 6.9, one can see that the values of efficiency and fake probability are very stable in the region of small M and small α, hence α is not considered as a free parameter in the evaluation of the corrections.

Figure 6.7 and Figure 6.9 show that the efficiency increases for larger values of P_t and

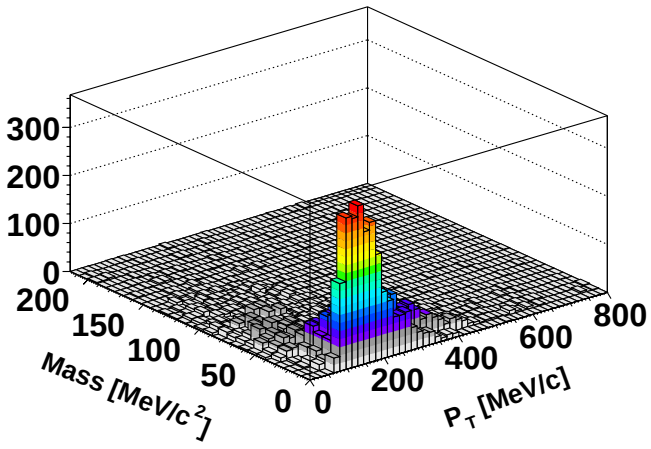

Figure 6.11: Yield of the reconstructed e^+e^- pairs for the NOV01 experimental data as a function of M and P_t.

the fake probability decreases. Figure 6.11 shows the yield distribution of the reconstructed di-electron pairs for the reaction C + C at 2 $AGeV$ as a function of M and P_t. One can see that the P_t distribution is peaked around 200 MeV.

That means that one can not integrate on the variable P_t when the efficiency and fake probability correction of the di-electron spectra extracted from the C + C at 2 $AGeV$ data are calculated. However, a folding of the efficiency and fake distributions with the yield distribution obtained for the e^+e^- pairs produced in the C + C at 2 $AGeV$ has to be applied.

A two-dimensional matrix, function of M and P_t, has been used for the efficiency correction and one for the fake contribution correction. Before the correction of the invariant mass distribution are discussed, the error propagation analysis is shown.

6.3 Correction of the simulated spectra

The detailed development of the e^+e^- cuts on the basis of the NOV01 data sample leads to certain simulated and experimental unlike-sign and like-sign distributions. The invariant mass distribution of the simulated and experimental data has to be corrected for the spectrometer acceptance, the detection efficiency (hardware and software) and

the fake probability, to obtain the real physics signal produced in the C + C reaction. First the correction has been applied to the simulated data, with the aim to check the self-consistency of the method. Two correction methods have been tested on the simulated data. The first corrects the unlike-sign distribution without the subtraction of the combinatorial background. A new fake probability has been calculated that includes the contribution of the combinatorial background. The unlike-sign distribution is corrected for the efficiency, for the fake probability due to the software and also for the combinatorial background contribution.
The second method applies the efficiency and fake probability correction with the matrices obtained in the previous section. The unlike-sign and like-sign distributions are respectively corrected, the combinatorial background is calculated with the same event technique and the corrected signal is extracted.
The first correction method has been applied in the following way: given an invariant mass spectrum ($Yield(M)$) with a defined number of bins n and the corresponding two-dimensional yield distribution function of M and P_t ($Yield(M, P_t)$), the efficiency ($Eff_{absolute}(M,P_t)$ see figure 6.7) and fake (Fake(M,P_t), see figure 6.9) two-dimensional distributions as a function of M and P_t with the same binning n in the variable M have been used. The fake probability matrix has been calculated including the pairs coming from combinatorial background since this contribution has to be subtracted from the unlike-sign yield in order to get the input distribution. The combinatorial background contribution enhances the number of fake pairs by about 30%. The resulting correction is:

$$Yield_{new}(M_i) = Yield_{old}(M_i) \cdot \frac{(1 - Fake(M_i))}{Eff(M_i)} \tag{6.6}$$

where $Yield_{old}(M_i)$ is the yield of the one-dimensional invariant mass spectrum that has to be corrected, $Fake(M_i)$ and $Eff(M_i)$ the fake contribution and the efficiency in the mass bin M_i and $Yield_{new}(M_i)$ the corrected yield.
The phase space distribution of the white generator is very different from the distribution obtained with the di-electron pairs produced in C + C at 2 $AGeV$ (see figure 6.11 and figure 6.1). Since the two-dimensional efficiency and fake probability shown in Figure 6.6 and in Figure 6.9 show a strong dependency on P_t, it is not possible to integrate over this variable. The efficiency and fake probability distributions have to be folded with the two-dimensional pairs yield (Yield(M,P_t)) (figure 6.11), as a function of M and P_t. The two quantities $Eff(M_i)$ and $Fake(M_i)$ have been calculated like:

$$Eff(M_i) = \sum_j Eff(M_i, P_{tj}) \cdot \frac{Yield(M_i, P_{tj})}{Yield_{TOT}(M_i)} \tag{6.7}$$

$$Fake(M_i) = \sum_j Fake(M_i, P_{tj}) \cdot \frac{Yield(M_i, P_{tj})}{Yield_{TOT}(M_i)} \tag{6.8}$$

$$Yield_{TOT}(M_i) = \sum_j Yield(M_i, P_{tj}) \tag{6.9}$$

Additionally to the correction the error has to be propagated.
The systematic error of M has already been discussed in 6.2.2. Since this error is not constant, in order to avoid a non constant binning, the error of the x variable

(mass) has been propagated on the y variable. Given the yield of each bin M_i and the corresponding error on the mass, the error on the yield has been calculated like:

$$error_{Yield}(M_i) = \frac{\partial Yield}{\partial M}(M_i) \cdot error_{M_i} \tag{6.10}$$

The systematic component of the error has been added quadratically to the statistical one.
Since so far only 400000 events have been analyzed to produce the correction matrices and since the pair cuts reduced consistently the statistic of reconstructed pairs, the accuracy of the efficiency and fake probability distribution is not satisfactory. In order to by-pass this problem, all the efficiency and fake probability distribution have been smoothed.
After the correction and the error propagation, one comes to the result shown in Figure 6.12.
The dashed line shows the invariant mass distribution for the unlike-sign pairs that fulfill all the pair cuts [Ebe 03]. The crosses show the histogram corrected for the fake probability and the absolute efficiency, the error includes the systematic and the statistical contributions. The full line shows the input invariant mass distribution for the reaction C + C at 2 $AGeV$, absolutely normalized to the same number of events analyzed for the corrected distribution.

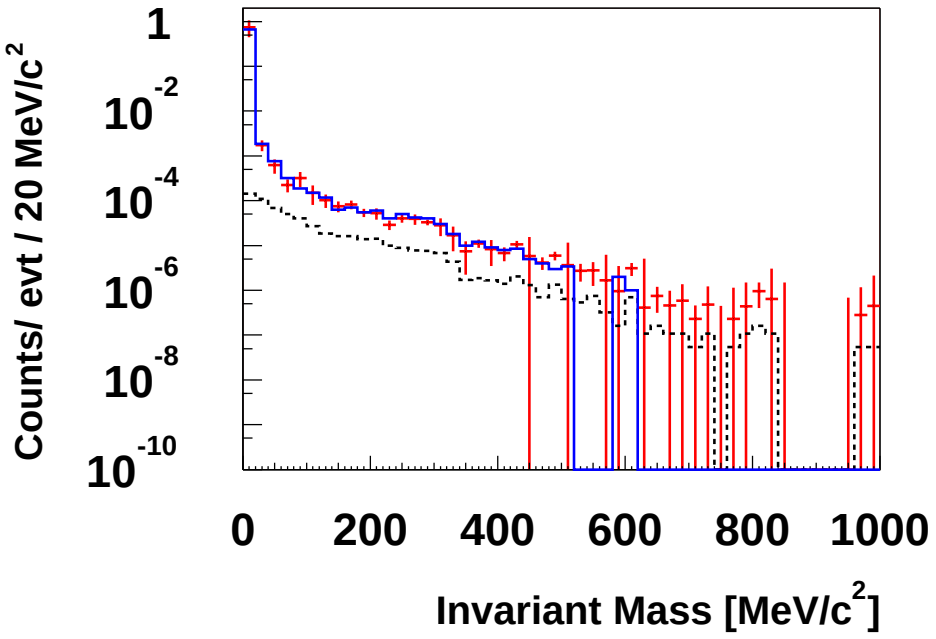

Figure 6.12: The invariant mass distribution of the di-electron signal that fulfill all the pair cuts is shown together with the corrected signal and the input. The dashed curve represent the signal before the correction, the data point with the error bars show the spectrum corrected for the efficiency and the fake contribution, the full line shows the input distribution.

One can see that the simulated data points are in good agreement with the input, inside the error bars.
The good agreement between the input and the corrected simulated distribution shows the self-consistency of the method. The correction that has been applied, includes the efficiency scaling but also gets rid of all the fakes, including those due to the combinatorial background.
This correction can be applied to the simulation data but should not be applied to the experimental data. Indeed the combinatorial background contribution to the experimental spectra is evaluated via statistical methods [Ebe 03], [Her 01]. For this reason a second correction of the simulated data has been tested.
The unlike-sign pair signal has been corrected for the efficiency and fake probability as shown in equation (6.6) , using a fake correction that does not include the combinatorial background contribution. The fake probability refers only to the wrongly reconstructed pairs left over by the limited resolution of the analysis. The same correction has been applied to the like-sign pair signal. Figure 6.13 shows the unlike-sign and the like-sign invariant mass distributions for the simulated data before and after the fake and efficiency correction has been applied. One can see that the correction modifies significantly the yield especially for the low mass range. Indeed, in this region the geometrical acceptance and the pair efficiency of the spectrometer are supposed to be very low [Sch 95]. Moreover it can be noticed that the asymmetry between the distributions of the negative and positive like-sign signal are strongly reduced after the correction, still some differences survive.
The combinatorial background was calculated via the same-event technique [Her 01] combining the corrected like-sign mass distributions shown in the lower panel of Figure 6.13 using the:

$$N_{background}(i) = 2 \cdot \sqrt{N_{++}(i) \cdot N_{--}(i)} \tag{6.11}$$

where N_{++}/N_{--} are the counts at the bin i of the negative and positive like-sign mass distributions.
The so obtained combinatorial background has been subtracted from the corrected unlike-sign signal.
Figure 6.14 shows the comparison between the two correction methods. The full circles represent the results from the first correction method, they correspond to the corrected distribution already shown in Figure 6.12. The square points show the signal after the background subtraction using the second correction method. It can be seen that the two distributions agree very well within the error bars up to 150 MeV/c^2 but between 150 MeV/c^2 and 300 MeV/c^2 the distribution obtained with the second method shows a hole not present in the first distribution. This is due to the statistical error introduced by the subtraction of the combinatorial background that was built using like-sign distribution that are not completely symmetric.
The fact that both methods enable the reproduction of the input distribution (see Figure 6.12) supports the idea of making use of the second method to attempt a correction of the experimental data too.

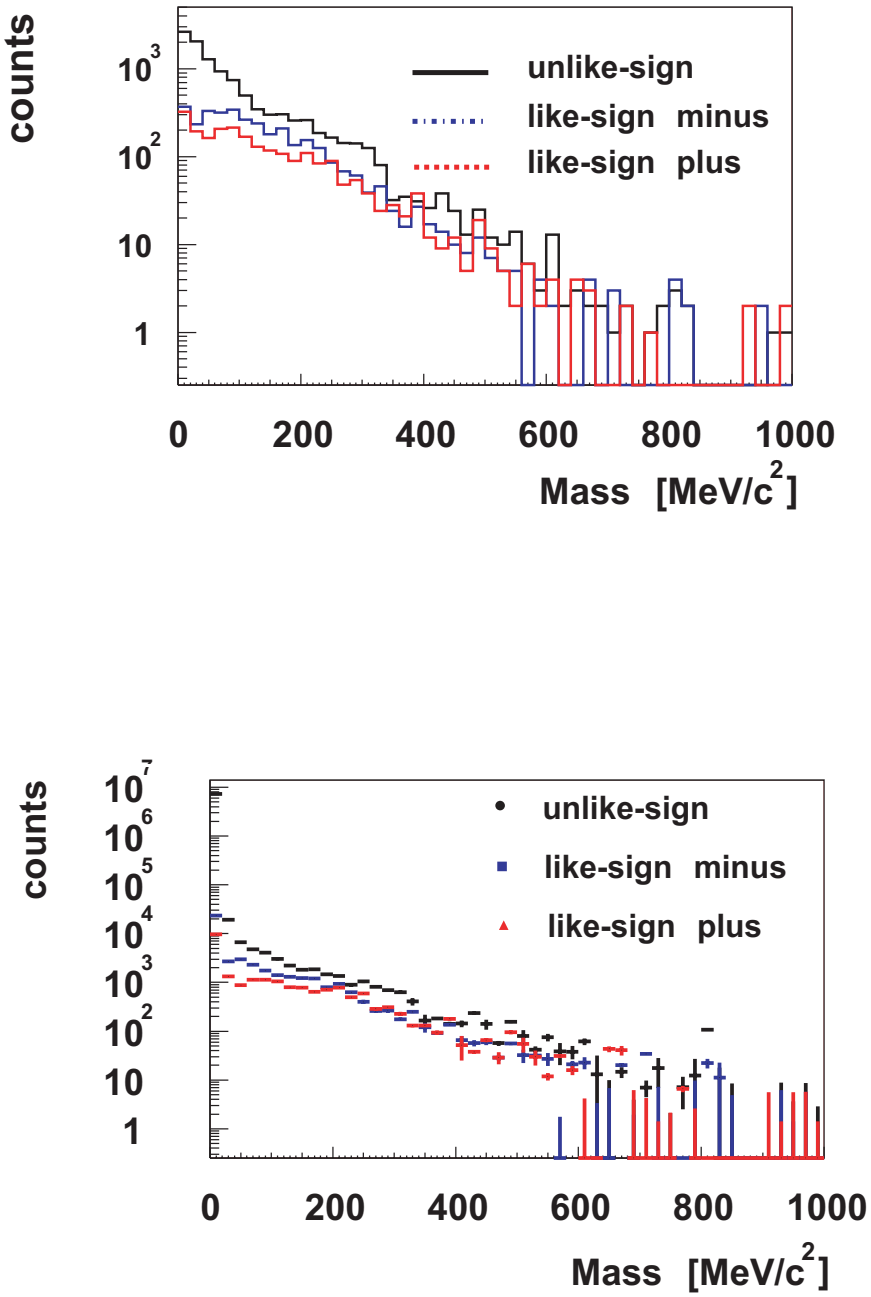

Figure 6.13: The unlike-sign and like-sign invariant mass distribution for the simulated data are shown before (upper panel) and after the correction (lower panel). The error shown in the lower panel is the total one, quadratic sum of the statistical and systematic contributions.

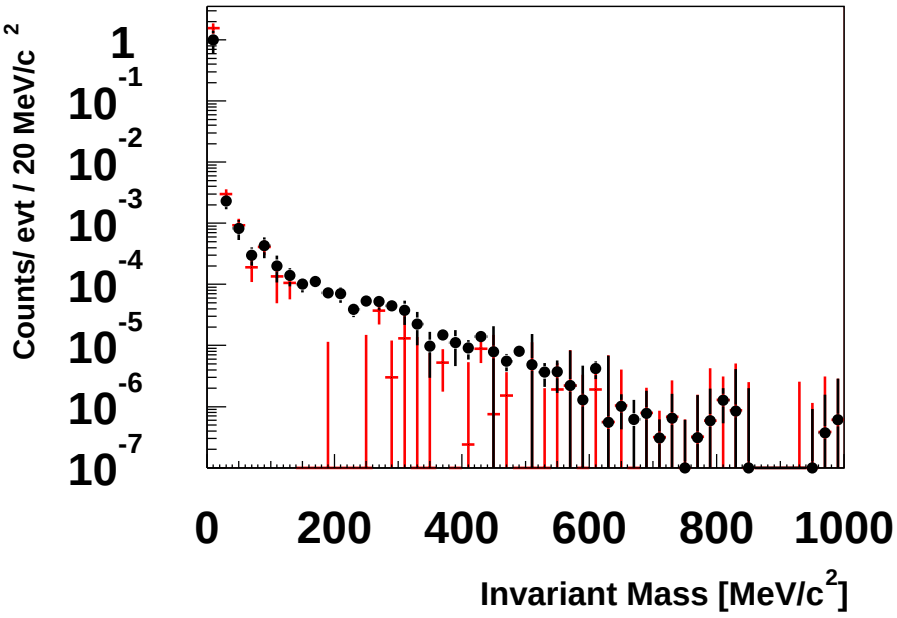

Figure 6.14: Comparison between the two correction methods applied to the simulation data. The full circles show the distribution corrected with the first method, the square points show the distribution corrected with the second method. Both distribution are normalized to the number of analyzed events.

6.4 Correction of the experimental data

The correction applied to the simulated data can be used for the experimental data under the assumption that the simulation realistically reproduce the experimental conditions. As far as the RICH detector is concerned it has been shown in chapter 4 that the understanding of the detector allows very realistic simulations. Additional studies concerning the single tracks and the pair characterization for the whole spectrometer has been carried out in [Ebe 03]. There it is shown that a good agreement has been achieved as far as the track and pair properties are concerned, but that there are still differences if one looks at absolute pair yields. In particular in [Ebe 03] it is shown that the absolute pair yield extracted in the simulation overestimates by a factor 2.7 the yield calculated with the experimental data.
This difference is partially due to the imprecision of the particle multiplicities delivered by the UrMQD input, to the different effects that the analysis cuts listed in 6.2 have on simulated and experimental data but especially to the absolute normalization of the spectra.
The second correction method has been nevertheless applied to the experimental data in order to check if the simulated and experimental spectra after the correction show evident differences from a qualitative and quantitative point of view.
Figure 6.15 shows the uncorrected unlike-sign and like-sign invariant mass distribution

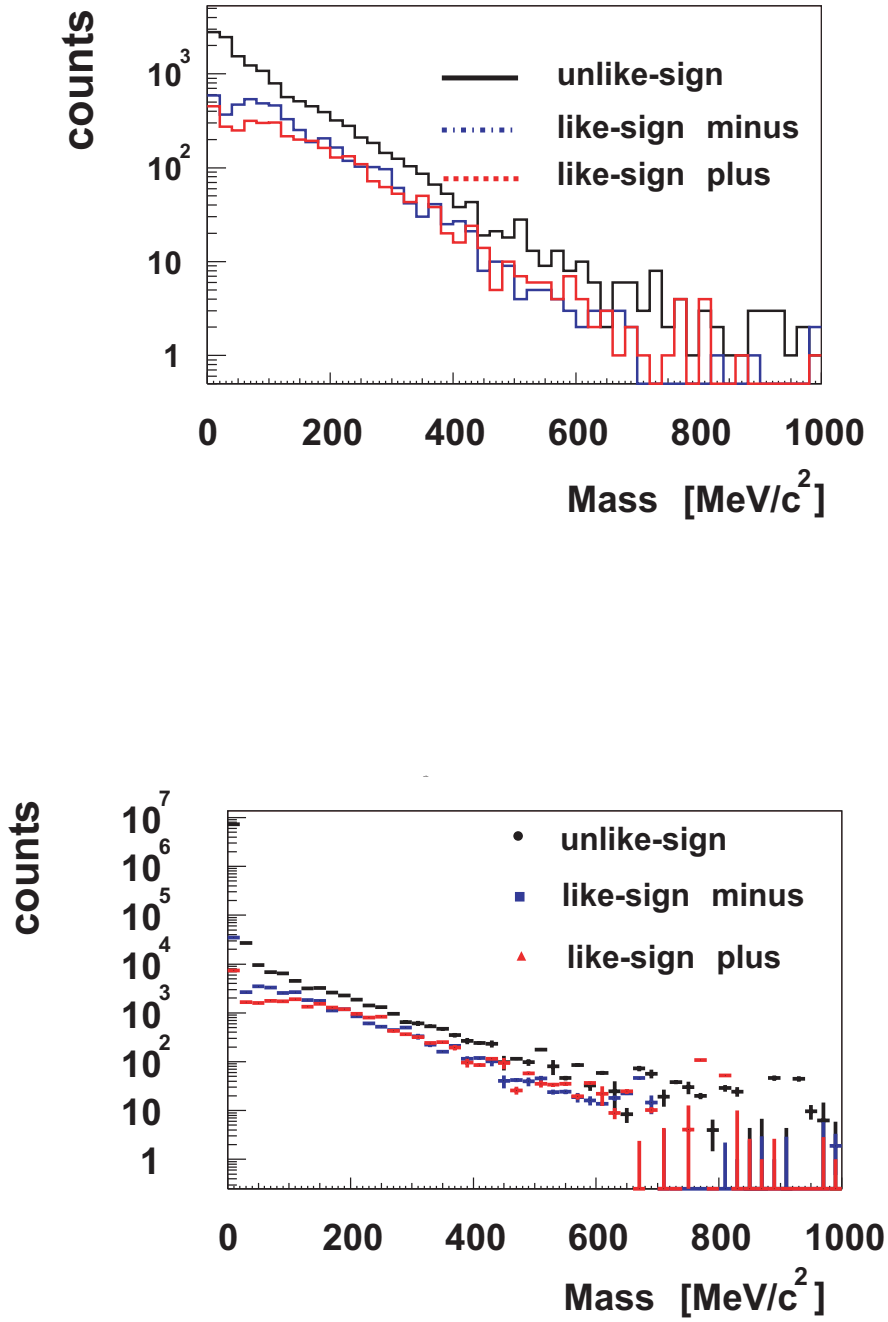

Figure 6.15: The unlike-sign and like-sign invariant mass distributions from the experimental data are shown before (upper panel) and after the correction (lower panel). The error shown in the lower panel is the total one, quadratic sum of the statistical and systematic contributions.

and the corrected ones. One can see that both the uncorrected and corrected distributions look very similar to the simulated distributions shown in figure 6.13. The combinatorial background has been again calculated with the same event technique and then subtracted from the corrected unlike-sign distribution. Figure 6.16 show the simulated and the experimental invariant mass distribution after the second correction method has been applied and the background subtracted. The experimental distribution has been scaled up by a factor 2.7 in order to compare the slope of the two distributions. One can see that the two distributions agree qualitatively very well, even if the absolute yield per event is not the same. One can notice that the disagreement between simulation and experimental data becomes larger after the correction is applied.
Due to the difference in the yield it is not possible at this stage of the analysis to extract the number of produced π^0 even if the simulation have achieved a quite good description of the experimental data.
The high peak at small invariant mass values is mainly due to the conversion contribution. The so-far applied cuts were not strict enough to get rid of all the conversion pairs. The results obtained with the full-scale simulations described in chapter 3 do not show the same pronounced peak for the small masses since the opening angle cut

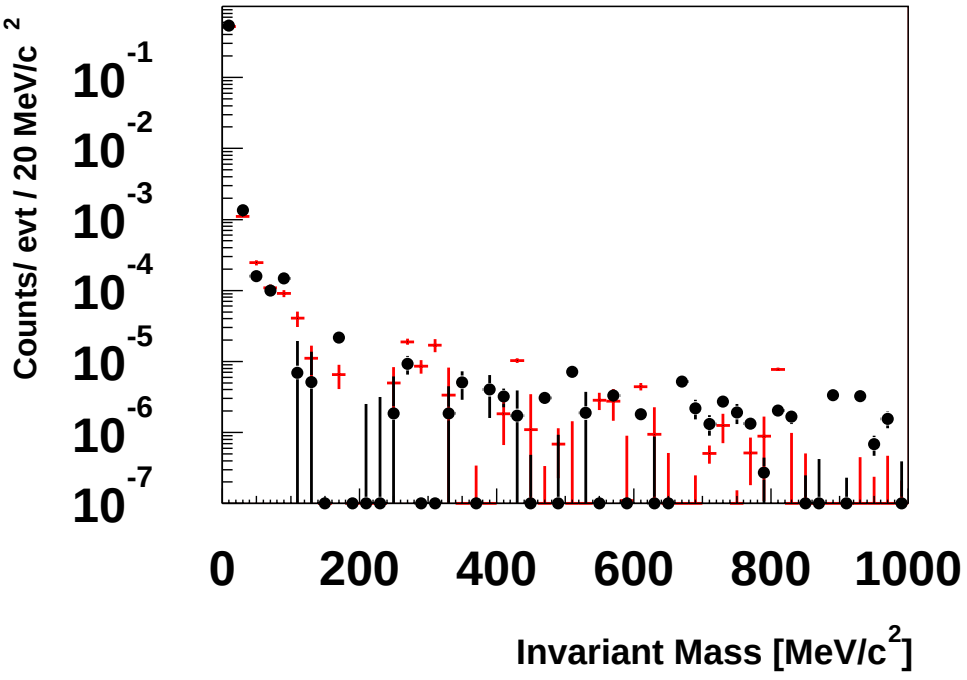

Figure 6.16: The full circles show the experimental invariant mass distribution after the fake and efficiency correction and the square point show the distribution of the simulated invariant mass after the correction. The experimental data have been scaled up of a factor 2.7 to compare the shapes of the two distributions.

of 15° was sufficient to get rid of all the conversion pairs. The low statistics collected in the NOV01 beam time did not allow the usage of such selective cuts that would have reduced the number of pairs dramatically.

Chapter 7

Conclusions and outlook

The response of the RICH detector of HADES to single photons was studied via a dedicated efficiency measurement carried out in November 2002, that allowed to understand in details the behavior of the MWPC to a single photon and evaluate the overall detector efficiency. From the analysis of these data a parameterization of the detector response has been developed that allows a CPU saving full-scale simulation of the RICH detector. The simulation results have been compared with the experimental data and a good agreement has been observed. The overall efficiency of the detector has been calculated in terms of a figure of merit (N_0). The parameter N_0 has been measured for each of the six RICH sectors separately and values between 70 and 85 cm^{-1} have been obtained.
The single e^+/e^- signals extracted from the C + C at 2 AGeV reaction have been studied, the experimental data have been analyzed in parallel with the full-scale simulation of the spectrometer. The single e^+/e^- efficiency of the RICH detector for different sources has been estimated via the simulation, at the same time the agreement of the single electron signature on the RICH detector between simulation and experiment has been verified. An average single electron efficiency of 85% has been obtained for e^+/e^- produced in target, the efficiency drops to about 20% for the γ-conversion products coming from the gas radiator.
The comparison between the lepton signature in experiment and simulation has allowed to identify a difference in the detector efficiency between November 2001 and November 2002 and to modify the parameterization of the detector in the simulations, such as to obtain a realistic description of the detector for both time spans.
The simulations have been used to develop a set of pair analysis cuts, which action have been parallel tested on experimental data. The geometrical acceptance of the unlike-sign pairs has been estimated and a value around 35% has been obtained. A difference of about 8% has been found for the geometrical acceptance of positive pairs, while the rest of the phase space shows no difference among unlike/like-sign pairs. For the pair efficiency recognition in the geometrical acceptance values around 45% and 15% have been obtained for the high ($M > 300\ MeV/c^2$) and low mass ($M < 150\ MeV/c^2$)range, respectively, leading to an absolute efficiency of 18% and 5% respectively.
The propagation of the statistical and systematic errors has been carried out for the dependent variables mass, transverse momentum, rapidity and opening angle, that characterize each di-electron pair. The analyzed invariant mass spectra from experimental and simulated data have been corrected for efficiency and fake probability in order to get an absolute pair yield.

The limits of the method have been pointed out. The present disagreement between experiment and simulation seems not to be connected with the properties of the RICH detector but further investigations are needed to individuate clearly the problem. One possible reason for this disagreement could lie in the normalization of the experimental data. It has indeed been observed that the first level trigger condition in the experiment (at least four particles identified in the META) do not always correspond to four full reconstructed particles in the whole spectrometer. The production of secondary particles in the simulation can differ from the experiment and this creates problems with the absolute normalization of the data.
Moreover the calculation of the correction matrices has to be repeated with much larger statistics in order to get rid of the huge error introduced by the correction.
Further cuts have to be tested that are able to reduce the contribution of the conversion pairs to the total signal. These cuts should be tested with the higher pair statistics available in the NOV02 data sample, that is being analyzed at the moment.

Appendix

A.1 Estimation of the Gas Amplification of the HADES-MWPC

The field configuration of the MWPC with a pad-cathode like in the HADES RICH (see figure 2.5) has not a symmetric configuration. This design was chosen in order to:

- a better charge coupling from the anodic wires to the cathodic pad-plane.
- a fast detector with a small gap.

If we consider distances of several 100 μm around the anode wire we can approximate the electric field as that of a cylindrical proportional counter. The electric field, the potential and the capacity of the proportional counter are :

$$E = \frac{\lambda}{2\pi\epsilon_0 \cdot r}, \quad 2\pi\epsilon_0 = 5.56 \cdot 10^{-11}\frac{F}{m}, \tag{A.1}$$

$$U = \frac{\lambda}{2\pi\epsilon_0} \cdot \ln(\frac{r_a}{r_i}), \tag{A.2}$$

$$\frac{C}{L} = \frac{2\pi\epsilon_0}{\ln(\frac{r_a}{r_i})}, \tag{A.3}$$

where r_a and r_i are the external and internal diameters of the counter, r is the distance from the center of the wire and λ is the charge density per unit length in the gas. The gas amplification G of the proportional counter can be expressed by:

$$\ln G = \frac{U}{\ln(\frac{r_a}{r_i})} \cdot \frac{\ln 2}{\Delta V} \cdot (\ln \frac{U}{\ln(\frac{r_a}{r_i}) \cdot p \cdot r_i} - \ln K), \tag{A.4}$$

$$\Delta V = 36.5 \pm 5V, \quad K = 6.9 \pm 0.5 \cdot 10^4 \frac{V}{atm \cdot cm} \quad for\ CH_4 \tag{A.5}$$

where p is the pressure in units of atm. This can be rewritten as:

$$\ln G = \frac{\lambda}{2\pi\epsilon_0} \cdot \frac{\ln 2}{\Delta V} \cdot \ln(\frac{\lambda}{2\pi\epsilon_0 \cdot p \cdot r_i \cdot K}) \tag{A.6}$$

In order to determine λ we need to calculate the exact electric field for our detector geometry. This is done by means of a finite element calculation program [CSP]. Figure A.1 shows a cross section of the MWPC. Given an anodic wire the field lines will be different depending on the direction they point too, since the geometry is not symmetric. In the picture three directions are shown: one pointing to the cathodic pad-plane (Down), one to the neighboring wire (Right) and the last pointing to the cathodic wires

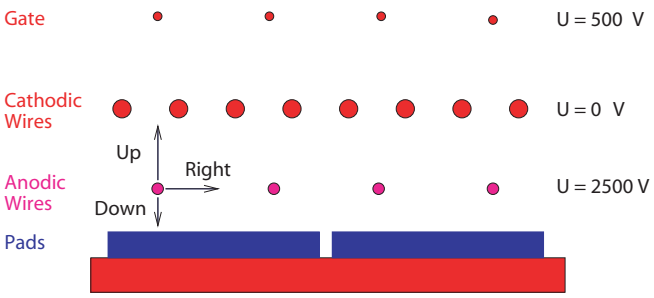

Figure A.1: Schematic view of the MWPC, the black arrows show the three directions of the field for which the gain G was calculated.

(Up). Using [CSP] we can calculate the exact field in the three directions, respectively: $E_U(r)$, $E_R(r)$ and $E_D(r)$. The charge density λ is calculated using (A.2) but one has to consider that the fields calculated with the CSP program using the real detector geometry are different from the electric field of a cylindrical counter. Therefore the $E_U(r)$, $E_R(r)$ and $E_D(r)$ are substituted in (A.2) and the value of λ calculated for 100 steps where the radius of the counter varies from 0 to 200 μm. The average among the values obtained in the 100 calculation steps is then built. This average can be substituted in (A.5) to calculate the corresponding gain. The maximum value of the radius is chosen in this way because the gas amplification occurs only within a distance of 200 μm from the anodic wire.
Table A.1 shows the results for the three field directions obtained assuming an anode voltage of 2600 V. For each λ the corresponding σ is shown as well.
The value corresponding to the 'Down' component of the field has been taken for the comparison with the experimental data shown in 4.2.2. There a disagreement of about 25% has been observed between the calculated and measured gain. This difference can be due to the fact the the effective field in the MWPC is a combination of the 'Down' and 'Right' component, therefore lower that the 'Down' component alone. The same

Direction	Up	Down	Right
$\lambda \cdot 10^{-8}\ [\frac{C}{m}]$	2.1	2.1429	2.1222
$\sigma_\lambda \cdot 10^{-10}\ [\frac{C}{m}]$	1.274	2.4522	3.1413
$G \cdot 10^5\ [e^-]$	1.96	3.07	2.42

Table A.1: Values of λ, σ and gain G for the three different field component.

calculation can be repeated for different anode voltages. Figure A.2 shows the resulting average signal $A_0 = G/1730\ e^-/ADC\ ch.$ defined in equation (4.6) , as a function of the anode voltage for the field in the three direction defined in figure A.1.
This detailed calculation provide results that can be compared with the values of the average signal extracted from the experimental data.

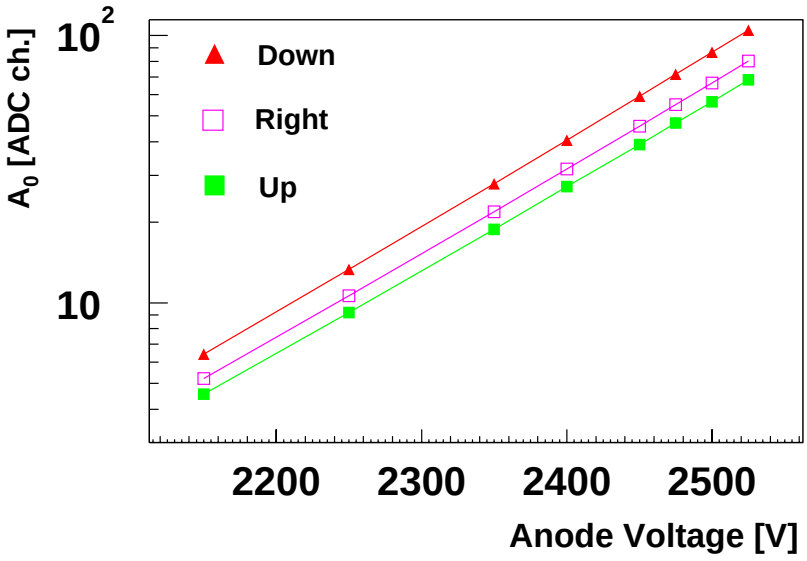

Figure A.2: MWPC gain as a function of the anode voltage, the three curves correspond to the three directions of the field defined in figure A.1.

A.2 Estimation of the spatial correlation cut between hits for the RICH and MDC detectors

The ring candidates found in the RICH detector must be spatially correlated with the reconstructed hits in the MDC chambers in order to suppress the patterns that do not correspond to any particle. The polar and azimuthal angle of each ring candidate must be matched with the polar and azimuthal angle of the reconstructed segment in the first two modules of the MDC that are before the magnet. The window used for this matching has been determined analyzing data without a magnetic field. Figure A.3 shows a schematic view of the method. Each RICH ring is correlated with a track segment reconstructed before the magnet and with the hits on the META detector. Figure A.4 shows the distribution of the difference in the polar and azimuthal angle between the RICH rings and the MDC segments. The histograms on the left were obtained correlating all possible combinations of rings and MDC hits and then subtracting the combinatorial background. The distributions on the right were obtained applying, additional to the spatial correlation between RICH-MDC and META hits, a cut on the time of flight between 5 and 9 ns. This cut on the time of flight should suppress slow protons and pions. The difference in the azimuthal angle between the hits is multiplied by $\sin(\theta)$ (being θ the polar angle) to keep the solid angle spanned by the correlation constant. It can be seen that the resolution becomes a bit better applying the time of flight condition. A second analysis was carried out using data measured with magnetic field on. The correlation scheme is similar to that shown in figure A.3. However, since the particle is bent in the magnetic field, we can not apply a sharp cut in the difference in polar angle between the RICH hits and the META. These bent tracks are reconstructed using the *Kickplane* method [San 03], such that

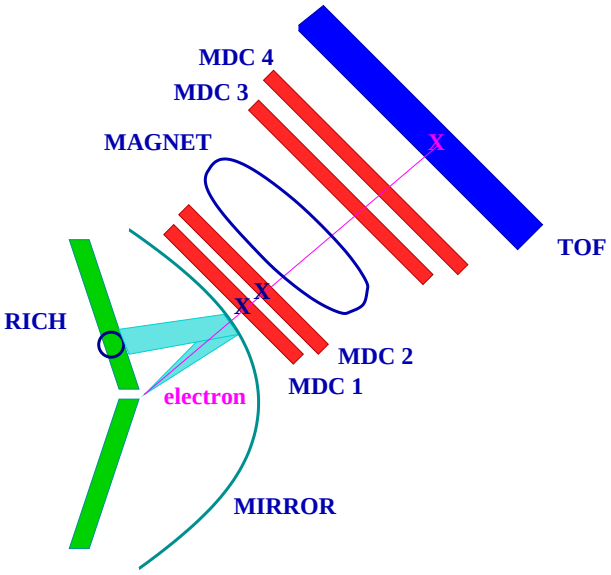

Figure A.3: Schematic representation of the detector components and of the geometrical correlation between the different detector hits without magnetic field.

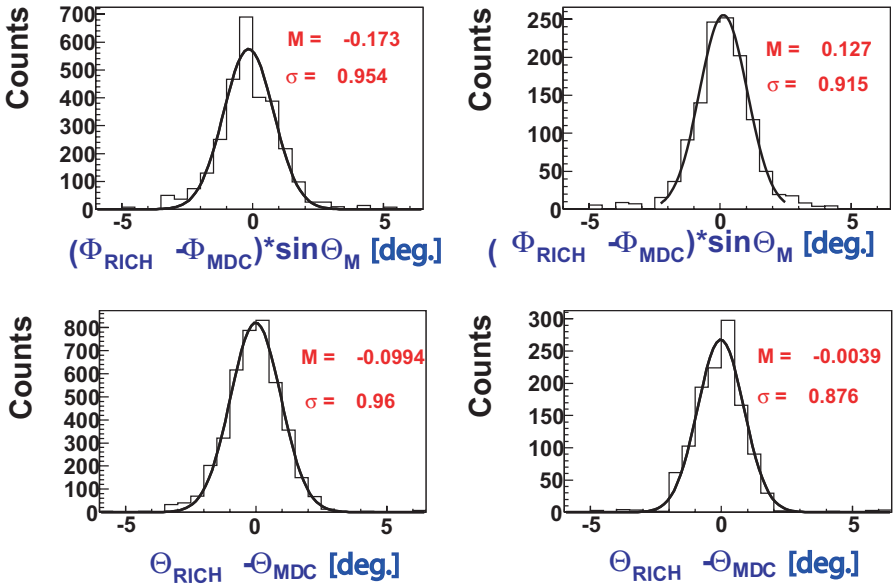

Figure A.4: The polar and azimuthal angle correlation (in deg) between recognized rings and MDC segments is shown. The distributions on the left were obtained from the combination of the RICH rings with the MDC segments, those on the right were obtained applying additionally: $5ns < tof < 9ns$. All the histograms refer to the experimental data without magnetic field.

the segment before the magnet is matched with the correct META hit. The rings are therefore correlated with the reconstructed tracks; one MDC segment corresponds to each reconstructed track. Figure A.5 shows the distribution of the difference in polar (θ) and azimuthal (ϕ) angle between the rings and the MDC segments for the rings correlated with the reconstructed tracks. One can see that the σ of the distributions become smaller compared with those in figure A.4. This happens because of the presence of the magnetic field. The low momentum leptons ($p < 50\ MeV/c$) will be thrown out of the geometrical acceptance of the spectrometer, while these leptons reach the META detector if the magnetic field is switched off.
The low momentum electrons come mostly from γ conversion processes that take place in the detector radiator (C_4F_{10}). The path length that those leptons cross in the radiator might be quite short and therefore the number of emitted Cherenkov photons quite low. This leads to "poorer"rings, with few photons and a high probability to be incomplete. It is very difficult to determine the correct position of an incomplete ring therefore there remain some candidates with a wrong position in the RICH detector. This leads to a broadening of the distributions shown in figure A.4.

The same analysis has been carried out using simulated data. The obtained distributions are shown in figure A.6. These distributions show a better spatial correlation between RICH rings and MDC segments, this is probably due to the fact that the simulation does not account for the possible optical deviation of the provisional mirror. This parameter influences the focusing of the photons and hence the position resolution

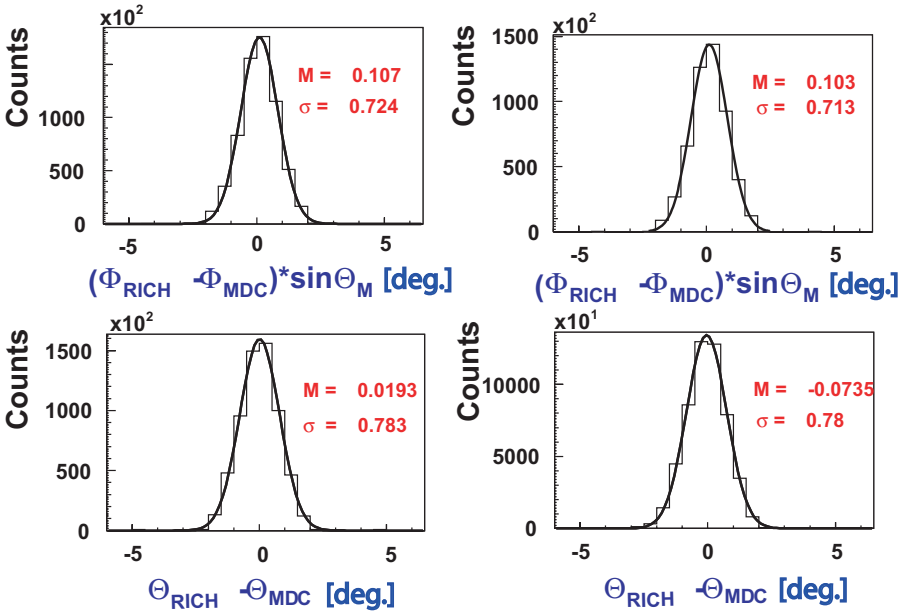

Figure A.5: The distribution correspond to the same cuts mentioned in figure A.4. Here the experimental data with high magnetic field are used as input. The analyzed reaction is: C + C at 2 AGeV

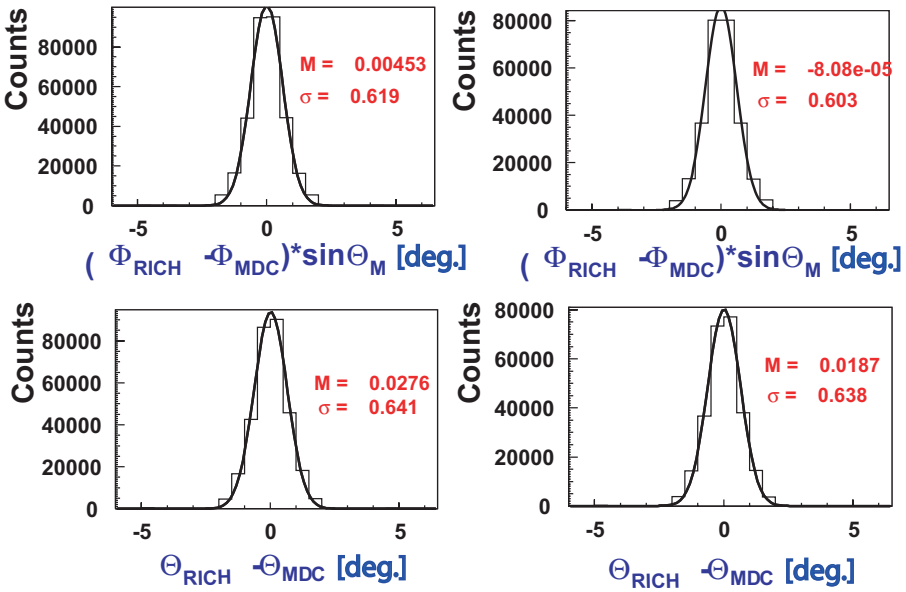

Figure A.6: The angular correlation (in deg.) extracted from the simulated data are shown. The reaction analyzed is C + C at 2 AGeV.

of the rings. The values of the correlation width for the polar and azimuthal angles shown in figure A.5 were used to analyze both experimental and simulated data. We apply a cut of $2.5 \cdot \sigma$ between the hits on the MDC detector and the rings on the RICH detector. A crucial point in setting the correlation window between different detector hits is the multiple matching. It can happen that two rings very close to each other match with the same MDC segment. This effect brings in some problems because it not possible a priori to decide which combination has to be taken.
As already mentioned in 5.1, the ring finder algorithms set a minimum distance between 2 rings candidates. This distance introduces a veto region around each identified ring. Given a minimum distance of 4 pads and known the dimension of the pads, it is possible to calculate the solid angle spanned by this veto region. We already saw in 2.2.4 that the dimension of the pads varies with the polar angle, to guarantee ring images with constant radius. Figure A.7 shows how the veto region solid angle stays almost constant along the whole polar angle range, as expected after the correction of the pads dimension. The solid angle spanned by the *3-pad* unit veto is about 3 msr

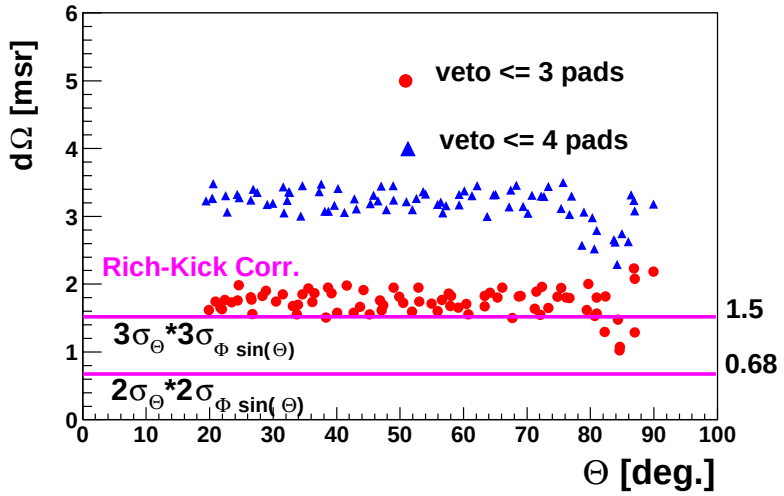

Figure A.7: Comparison between the solid angle spanned by the RICH-MDC correlation cut (continous line, 2 and 3 σ) and the veto region around each recognized ring. The solid angle is shown as a function of the polar angle, data for the veto region of 3 and 4 pads are shown.

while that obtained for the *4-pads* veto is about 2 msr. The two pink lines shows the solid angle corresponding to a 2σ and 3σ geometrical correlation. One can see that both lines are always lower than the veto region points. That means that the presence of the veto region limits to a very small number (5%) the chance correlation of two rings with the same MDC segment.

A.3 Time dependence of the RICH detector single photon efficiency

The results obtained from the analysis of the OEM data taken in NOV02 (see chapter 4) delivers a correction of the single photon efficiency that has been used for the simulation of the NOV01 data. Since the comparison of the single photon spectra (see section 4.3) between simulation and experimental data deliver a good agreement, one expects the same if the ring properties are compared when the electrons produced in a heavy ion reaction are analyzed.
Figure A.8 and figure A.9 show the comparison between experimental and simulated data for some of the ring properties (see section 5.3.2), all the ring candidates have been correlated with the MDC detector according to the geometrical cuts defined in A.2, to get a clean sample of lepton tracks. Figure A.8 shows the pattern matrix (PM) quality distribution, the continuous line represents the experimental data, the dashed line the simulation obtained with the OEM efficiency parameterization and the dash-dotted line the results obtained with the parameterization for the ideal efficiency. Figure A.9 shows the same comparison for the Hough transform (HT) quality. One can see that all

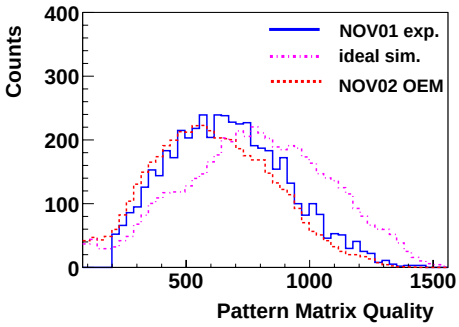

Figure A.8: Comparison between the PM quality distribution obtained for the correlated rings in the NOV01 experiment (continuous line), in the simulations with the ideal optical properties (dashed-dotted line) and for the simulation corrected via the NOV02 OEM measurement (dashed line).

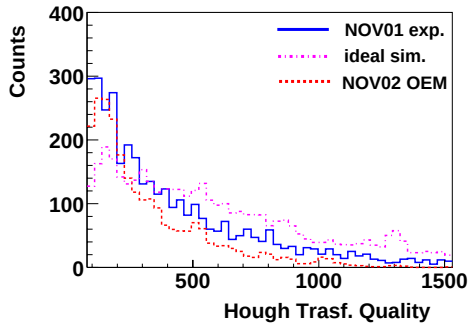

Figure A.9: The same comparison shown in figure A.8 is shown for the HT quality.

the simulated distributions obtained with the OEM efficiency parameterization underestimate the experimental distribution , while the distributions for the ideal efficiency overestimate them.
This fact suggests that the RICH efficiency has changed between November 2001 and November 2002 and in particular it has slightly decreased. Further analysis of the NOV02, C + C data should confirm this hypothesis. A good agreement should be observed between the experimental rings and the simulated one for the efficiency parameterization extracted from the NOV02 simulations.
As far as the NOV01 data are concerned, the single photon efficiency has been modi-

fied such that the properties of the simulated rings are comparable to the experimental ones. The result is a single photon efficiency that is between the ideal one and the one obtained from the NOV02 OEM analysis. Figure A.10 shows the ratio $R(\lambda)$ (see for details 4.21) extracted from the OEM analysis and the adjusted one as a function of

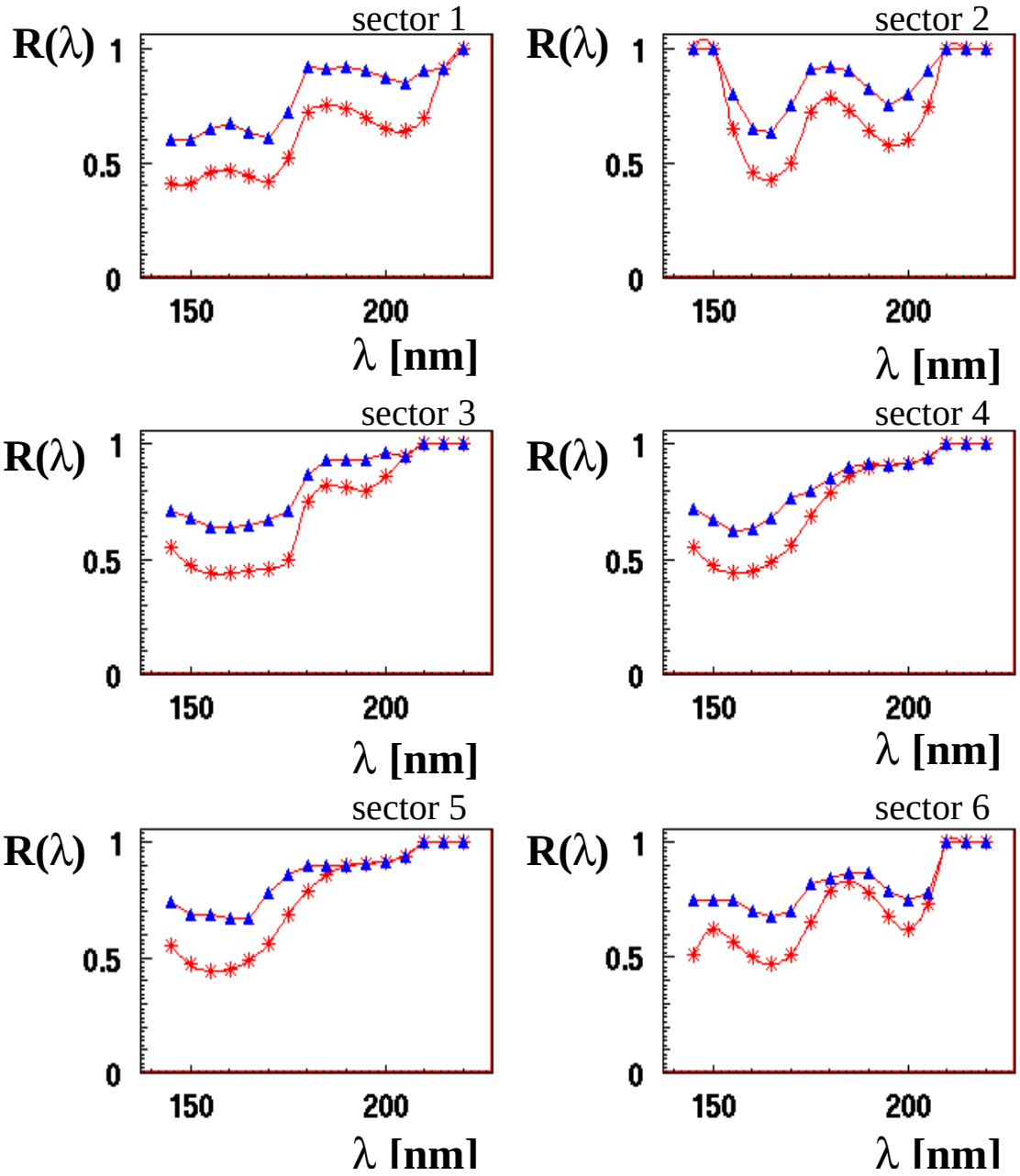

Figure A.10: The ratio $R(\lambda)$ between the number of photons identified in the OEM experiment and in the simulation is shown (stars) together with the values adjusted for the NOV01 data (full triangles) as a function of the photon wavelength.

the photon wavelength.

The stars show the OEM parameterization and the full triangles show the modified values. One can see that the difference between the two curves is stronger for the range $\lambda < 180\ nm$, but also the modified curve does not fit 100 %. In general a degradation of about 20% is observed if the extrapolated RICH efficiency of NOV01 is compared with the values of NOV02.

Figure A.11 and figure A.12 shows the comparison between experiment and simulation for the PM and HT quality when the modified parameterization of the single photon efficiency is used. The agreement is now reasonable.

The described sets of parameters have been used to process the HGeant simulations for the NOV01 and NOV02 experiments.

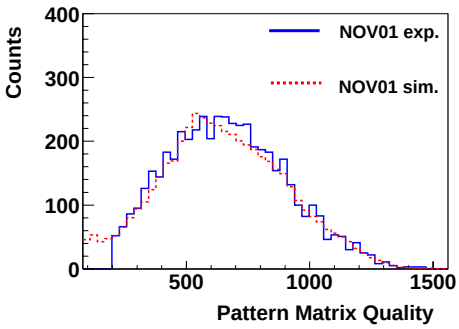

Figure A.11: Comparison between the PM quality distribution obtained for the correlated rings in the NOV01 experiment (continuous line) and in the simulations with the modified efficiency shown in figure A.10 (dashed line).

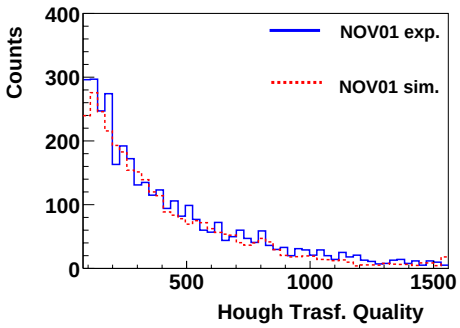

Figure A.12: The same comparison shown in figure A.11 is shown for the HT quality.

A.4 The UrQMD event generator

In order to describe a heavy ion reaction, one should make use of the Quantum Chromo Dynamic (QCD) theory, that describe the quark dynamic. Since there are no available solutions yet for this problem, the heavy ion collisions have been so far described by means of hydrodynamical and ideal gas like models.
Among the most successful models that have been used to describe the experimental data, we can find models that solve the Hamilton equations of a many-body system (Quantum Molecular Dynamic, QMD[Aic 86],[Aic91]). The QMD model is based on the classical concept of phase-space trajectories and can be analyzed event by event like the experimental data. In general all QMD models are constituted of three parts:

1. initial equation of state,

2. propagation of the primary and secondary particles,

3. hadron collisions and the decay of instable particles.

Given a heavy ion collision, each nucleon of the target and projectile is assigned a stochastic distributed Fermi momentum, where the Fermi sphere is proportional to the proton and neutron density.
The nucleons propagation can be done by means of a Cascade model, that ejects particles on straight trajectories. This model does not account for compression effects in the nuclear matter, that is considered in the Ultra Relativistic QMD (UrQMD) model via an equation of state [Kon 96] that includes the Skyrme component and the Yukawa-Coulomb interaction. Once the interaction potential is built, the Hamiltonian equations of motion are solved numerically.
The so calculated particle trajectories might eventually come closer and a binary collision can occur. The collision rate is calculated considering the particle interaction cross-sections as geometrical surfaces. That means that given their interaction cross-sections, two particles collide if they come close enough and their respective geometrical cross-sections overlap. After the collision has occurred the particle dynamic evolves further, up to the next collision.
All the particle species has to be included in the UrQMD calculation to reproduce the experimental data, expecially the different resonances and their decays have to be accuratly described. Indeed the particle production in the UrQMD model happens via excitation and subsequent decay of resonances. A complete list of all the particle implemented in the UrQMD is given in [Ern 98].

Currently, the analysis of the available HADES data is focused on the answer of the spectrometer to the π^0 channel. The UrQMD model has been used as input of the HADES full scale simulation to provide a basis of comparison with the experimental data. The results of the UrQMD calculation can be compared with the so far experimentally measured values for the π^0 multiplicities. Table A.2 shows the comparison between the π^0 multiplicities calculated with the UrQMD [Ern 98] and measured by the TAPS experiment [Ave 97] for the reaction C +C at the energies 0.8, 1.04 and 2 AGeV.

System	$^{12}C + ^{12}C$					
Source	TAPS	UrQMD	TAPS	UrQMD	TAPS	UrQMD
Energy [AGeV]	0.8	0.8	1.04	1.0	2.0	2.0
Δy	0.42-0.74	0.42-0.74	0.42-0.74	0.42-0.74	0.8-1.08	0.8-1.08
$< M >_{\pi^0}^{\Delta y}$ $[10^{-2}]$	6.0 ± 0.4	6.0	8.0 ± 0.5	8.7	13.7 ± 1.7	16.7
y	all	all	all	all	all	all
$< M >_{\pi^0}^{\Delta y}$ $[10^{-2}]$	22.2±1.8	32.3	33.5 ±2.5	52.2	82.6±8.4	122.4

Table A.2: Mean multiplicities of π^0 mesons measured by TAPS and given by the UrQMD calculation for $^{12}C + ^{12}C$ collisions.

The multiplicties are compared in the rapidity interval covered by the TAPS acceptance and for the extrapolation to the full rapidity interval. The extrapolation of the experimental data has been obtained assuming an isotropic angular distribution in the center of mass system. One can see that the experimental and calculated π^0 multiplicities $< M >$ are in good agreement for the rapidity intervals $(0.42 - 0.74,\ \ 0.8 - 1.08)$ ($\frac{<M>_{\pi^0}^{TAPS}}{<M>_{\pi^0}^{UrQMD}} = 1$ (at 0.8 $AGeV$), 0.92 (at 1.0 $AGeV$), 0.82 (at 2 $AGeV$)) but diverge for the full rapidity interval ($\frac{<M>_{\pi^0}^{TAPS}}{<M>_{\pi^0}^{UrQMD}} = 0.69$ (at 0.8 $AGeV$), 0.64 (at 1.0 $AGeV$), 0.68 (at 2 $AGeV$)). It has anyway to be pointed out that the angular pion distribution was assumed to be homogenous but could have an enhancement of about 10% in higher rapidity intervals due to collective flow [Hol 02]. Therefore the extrapolated multiplicities are eventually underestimated by 10%.
The difference between the multiplicities measured by TAPS and the one calculated via UrQMD has been taken into account in the π^0 yield found for the HADES HGeant simulation [Ebe 03].

A.5 Kickplane

The momentum determination for the low resolution set-up (no MDC planes behind the magnetic field) is calculated via the kickplane method. Given a reconstructed trajectory in the first two MDC planes and given the position of the hit on the META detector, the particle momentum can be reconstructed using a parameterization of the trajectory deflection in the magnetic field. The mapping of the magnetic field has been measured in [Bre 99] and the field distribution is schematically depicted in figure A.13. The action of the magnetic field on a particle trajectory is exerted in a single point, that is the intersection of straight trajectories calculated before the magnet and the *kickplane surface*. This surface is almost flat and sits close to the central line of the magnetic field (see figure A.13. Each point of this surface corresponds to a so-called *momentum kick* that has been tabulated as a function of the field mapping using HGeant simulations. The momentum is calculated using :

$$p = \frac{P_T}{2 \cdot \sin(\Delta\theta/2)} \tag{A.7}$$

where θ is the deflection angle in the polar coordinate and P_T the momentum kick. The deflection θ is calculated using the reconstructed trajectory before the magnet and the hit on the META detector. The resolution in the momentum determination achieved with this method is on average 7%.

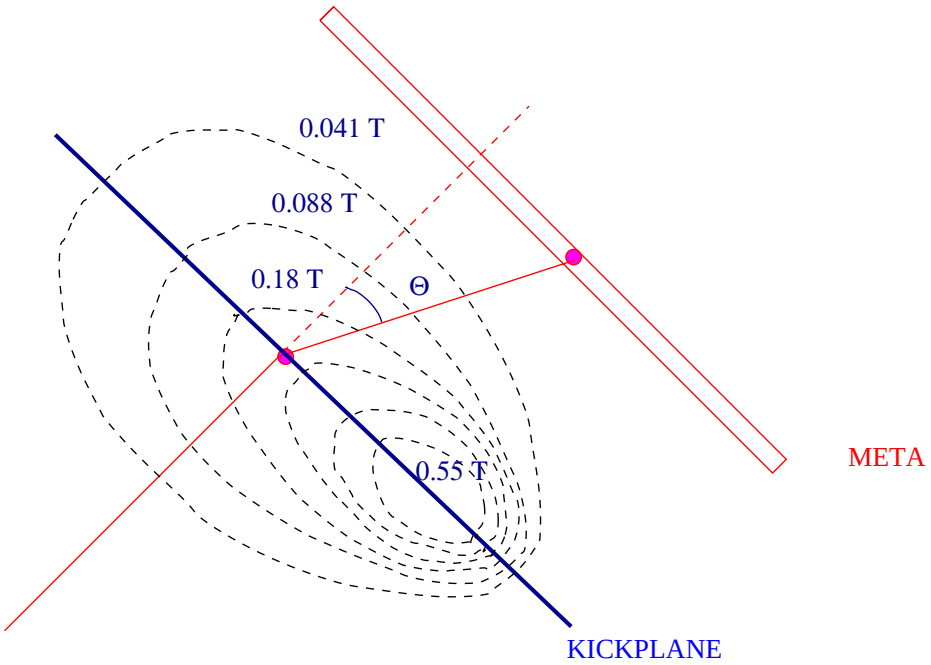

Figure A.13: Schematic view of the kickplane surface together with the field mapping and the META detector.

Acknowledgments

In primo luogo vorrei ringraziare Andi, per la sua infinita, amorevole pazienza durante questo ultimo anno, per l'aiuto nella correzione della tesi e perche' e' sempre stato, anche nei momenti bui, il mio piu' accanito sostenitore. A lui dedico queste pagine. Grazie a mia madre e mia sorella che mi hanno sempre incoraggiato a fare il meglio ed ad essere soddisfatta del mio lavoro, alle mie amiche Rita e Stefania, che piu' di una volta si sono sorbite infinite lamentele e dettagliati reportage delle mie fatiche, dandomi consigli decisivi.
Ich will mich herzlich auch bei Adel und Fips bedanken, für die Interesse, die sie gegenüber meine Arbeit gezeigt haben und für die Ermutigung in den letzen Monaten.

All this started in 98, when I met Jürgen and he gave me the chance to come to Munich. I thank him for this, for all the efforts he had to put in teaching me how to express my thoughts in an understandable way and expecially for the careful, multiple corrections of this thesis.
Prof. Körner has welcomed me in his group for this PhD, he has moreover always shown me his appreciation. I will always remember him. Prof. Krücken has allowed me to go on with the work and expecially supported me a lot in the final stage of this work. My dearest thanks go to both of them.

I'd like to thank my friend Thomas for these 5 years of common projects, ideas, fights and achieved goals, without his help I'd have probably left Munich after 2 months! Thanks also to Roman who advised me in a great way concerning several items, showing brilliant ideas, an enormous patience and always trying to get to a precise solution.

I thank all my colleagues at E12 for these years, especially Tassilo, Benjamin, Mathias and Ludwig.
This work has been done together with many people sitting around in Europe. My dearest thanks goes to Piotr, Wolfgang and Romain, for the enlightening discussions and the continuous input I received from them. Additionally I thank Ilse, for her patience explanations about the RTDB and Oracle jungle and all our smoked chats.
Witek has more or less saved me and Thomas in the first months, taking us out of the valley of tears and has carried on being an important reference for all the time.
In these years we had several beam-times and meetings among the analyzers. I have really enjoyed all of this and I think we did a good job. In this context I'd like to thank my 'experienced' PhD fellows: Jaro, Jochen, Dusan, Peter, Marcin, Tomek, Jazek, Manuel and Hector.
Concluding I'd like to thank myself, because I have never given up.

Bibliography

[Aic 86] J. Aichelin and H. Stöcker., Phys. Lett. B**176** (1986),14.

[Aic91] J. Aichelin, Phys. Rep., **202** (1991) 233.

[Aga 96] G. Agakichiev et al., Nucl. Phys. A**610** (1996) 317c.

[Ago 03] C. Agodi et al., Nucl. Instr. and Meth. A**492** (2002) 14-25.

[Alk 70] G.Alkazov et al., Nucl. Instr. Meth. A**89** (1970) 155.

[Arn 88] R. Arnold et al., Nucl. Instr. Meth. A**269** (1988) 255.

[Ave 97] R. Averbeck et al., Z. Phys. A**359** (1997) 65.

[Bal 03] A. Balanda, *Performance of the Pre-Shower Detector for HADES*, to be published in Nucl. Instr. Meth. (2003).

[Bas 95] S. Bass et al, Phys. Rev. C**1995** (1995) 3343.

[Ber 94] F.D. Berg et al., Phys. Rev. Lett. **72** 7 (1994) 977-980.

[Ber 00] E. Berdermann et al., Diamond and Related Materials **10** (2001) 1765-1769.

[Bok 02] H. Bokemeyer et al, Nucl. Instr. Meth. A**477** (2002) 397.

[Bour 76] M. Bourquin and J. M. Gaillard, Nucl. Phys B**114**(1976) 334-364.

[Bra 96] P. Braun-Munziger et al., Phys. Lett. B**365** (1996) 1.

[Bra 98] E. L. Bratkovskaja et al., Phs. Lett. A**634** (1998) 168.

[Bra 99] E. L. Bratkovskaja et al., Phs. Lett. B**445** (1999) 265.

[Bra 00] E. L. Bratkovskaja et al., Nucl. Phys. A**686** (2001) 568-588.

[Bre 99] T. Bretz, *Magnetfeldeigenschaften des Spektrometers HADES*, PhD thesis, Technische Universität München (1999).

[Bro 91] G. E. Brown et al., Phys. Rev. Lett. **66** (1991) 2720.

[Cas 95] W. Cassing et al., Phys. Lett. B**363** (1995) 35;
G.Q. Li et al., Nucl. Phys. A**606** (1996) 568;
C. M. Hung et al., Phys. Rev. C**56** (1997) 453.

[Cas 99] W. Cassing, E.L. Bratkovskaya, Phys. Rept. **308** (1999) 65.

[Che 37] P. A. Cherenkov, Phys. Rev. **52** (1937) 378.

[CSP] J. Berrios and R. Kupeinskas, *The Charge Simulation Program*, Worcester Polytechnic Institute (1993).

[Cug 81] J. Cugnon et al., Nucl. Phys. A**360** (1981) 444.

[Dam 01] S. Damianovic, *Electron-Pair Production in Pb-Au Collisions at 40 AGeV*, Ruperto-Carola University Heidelberg (2002).

[Del 98] A. Delbart et al., *Cherenkov Radiation Emission in uniaxial optical materials*, Eur. Phys. J. D**1** 109-116 (1998).

[Ebe 03] T. Eberl, *Untersuchung π^0-Mesonen induzierter e^+e^--Paare in C + C Stössen.*, PhD thesis, Technische Universität München (2003).

[Ern 98] C. Ernst et al., Phys. Rev. **C58** (1998) 447.

[Ern 98] C. Ernst, *Dileptonen als Signal für in-Medium-Effekte in relativistischen Schwerionenkollisionen*, PhD thesis, Johann Wolfgang Goethe University Frankfurt (1998).

[Eur 98] Eur. Phys. J. C**3** 1-794 (1998).

[Fri 99] J. Friese et al, Nucl. Instr. Meth. A**438** (1999) 86.

[Fri 03] J. Friese et al., Nucl. Instr. Meth. A**502** (2003) 241-245.

[Gea] GEANT CERN Program Library.

[Ger 96] R. Gernhäuser et al., Nucl. Instr. Meth. A**371** (1996) 300.

[Ger 98] R. Gernhäuser, *Ein ringabbildener Cherenkovdetektor zur Untersuchung schwerer Projectilfragmente*, PhD thesis, Technische Universität München (1998).

[Ger 99] R. Gernhäuser et al., Nucl. Inst. and Meth. A**438** (1999) 104.

[Had 94] *Proposal for a High-Acceptance Di-Electron Spectrometer*, GSI, internal report (1994).

[Her 01] G. Hering, *Dielectron production in heavy-ion collisions at 158 GeV/c per nucleon*, PhD thesis, Technische Universität Darmstadt (2001).

[Hol 97] R. Holzmann et al., Phys. Rev. C**56** (1997) 290.

[Hol 02] R. Holzmann, private communication.

[Hou 62] P. V. C. Houghs, U. S. Patent 3 069 654, Dec 1962.

[Iab 96] Industrieanlagen Betriebsgesellschaft, *Werkstoffdatenblatt Isotroper Kohlenstoff*, (IABG), Ottobrunn (1996).

[Ill 88] J. Illingworth, Computer Vision, Graphics and Image Processing **44** (1988) 87-116.

[Kas 99] A. Kastenmüller et ak, Nucl. Instr. Meth. A**433** (1999) 438.

[Kas 00] A. Kastenmüller, *Nachweis von e^+/e^--Paaren aus Schwerionenstössen mit einem RICH Detektor*, PhD thesis, Technische Universität München (2000).

[Kon 96] J. Konopa, *Fragmentproduktion und Teilchenfluss in Schwerionenstössen und ihre Bedeutung für die thermodynamischen Eigenschaften von Kernmaterie*, PhD thesis, Johann Wolfgang Goethe University Frankfurt, (1996).

[Lea 93] V. F. Leavers, CVGIP: Image Understanding, 58 no. 2 (Sept. 1993) 250-264.

[Leh 00] J. Lehnert, *Echtzeit-Mustererkennung zum Elektronennachweis mit einem RICH-Detektor in relativistichen Schwerionenkollisionen*, PhD thesis, Justus-Liebig-Universität Giessen (2000).

[Lin 01] E. Lins, *Entwicklung eines Ausles- und Triggersystems zur Leptonenidentifizierung mit dem HADES-Flugzeitdetektor.*, PhD thesis, Justus-Liebig-Universität Giessen (2001).

[Lut 92] M. Lutz et al, Nucl. Phys. A**542** (1992) 621.

[Mar 03] J. Markert, Phd Thesis to be published.

[Mas 95] M. Masera, Nucl. Phys. A**590** (1995) 93c.

[Mat 95] H. S. Matis et al., Nucl. Phys. A**583** (1995) 617c-622c.

[Mor 74] H.D. Morgan et al.,J. Chem. Phys. **60** (1974) 4734.

[Mue 95] M. Münch, *Ein Datenaufnahmsystem mit Echzeit-Bildverarbeitung für Ringabbildende Cherenkovdeteketoren*, Diploma thesis, Technische Universität München (1995).

[Opt 93] Optovac, Optical Crystal Handbook, N. Brookfield (1993).

[Pal85] Handbook of Optical Constants of Solids IIAcademic Press, p. 899-914 (1985).

[Pet 00] M. Petri, *Entwicklung eines kombinierten Auslese- und Echtzeit-Triggersystems zum Nachweis von Elektronen/Positronen-Signaturen in einem elektromagnetischen Schauerdetektor.*, PhD thesis, Justus-Liebig-Universität Giessen (2000).

[Piu 03] F. Piuz, Nucl. Instr. Meth. A**502** (2003) 76-90.

[Plu 00] http://www-hades.gsi.de/computing/pluto/html/PlutoIndex.html.

[Por 95] R. J. Porter et al., Nucl. Phys. A**583** (1995) 617c.

[San 03] M. G. Sanchez, *Momentum Reconstruction and Pion Production Analysis in the HADES Spectrometer at GSI*, PhD thesis, Santiago de Compostela University (2003).

[Sha 92] L.G.Shapiroand R.M.Haralick *Computer and robot vision* Addison-Wesley 1992

[Sch 95] H. Schön, *HADES-Ein Dielektronspektrometer hoher Akzeptanz für relativistiche Schwerioenkollisionen*, Phd thesis, Johann Wolfgang Goethe University Frankfurt (1995).

[Sch 96] R. Schicker et al.,Nucl. Instr. and Meth. A**380** (1996) 586.

[Sch 00] S. Schröder, *Entwicklung und Aufbau eines Systems zur Effizeinzkalibration des HADES-RICH*, diploma thesis, Technische Universität München, 2000.

[Shu 78] E.V. Shuryak, Phys. Lett. B**78** (1978) 150.

[Sie 79] (thermal model/fireball) Siemens and Rasmussen, Phys. Rev. Lett., 42 (1979) 880.

[Sta 98] J. Stachel, *Proc. of the International Nuclear Physics Conference*, Paris, (1998).

[TDR 99] F. Piuz et al., CERN/LHCC 98-19 ALICE TDR1 (1998).

[Toi 03] A. Toia et al., Nucl. Instr. and Meth. A**502** (2003) 270.

[Tra 00] M. Traxler et al., IEE Trans. Nucl. Sci. 47 (2000) 376.

[Urb 98] M. Urban et al. Nucl. Phys. A**641** (1998) 433;
R. Rapp et al. Adv. Nucl. Phys. **25** (2000) 1.

[Wil 98] W. K. Wilson et al., Phys. Rev. C**57(4)** (1998) 1865.

[Wei 96] W. Weise, Nucl. Phys. A**610** (1996) 35c-48c.

[Wit 02] W. Przygoda *Identyfikacia czastek e^+/e^- za pomoca detektora RICH w spektrometrze HADES*, PhD thesis, Jagellonian University Crakow (2002).

[Zei 03] K. Zeitelhack, private communication.

[Zov 03] D. Zovinec, Phd Thesis, Slovac Academy of Science, Bratislava, to be published.